Biodynamic Analysis of Human Torso Stability using Finite Time Lyapunov Exponents

Martin L. Tanaka

Dissertation submitted to the faculty of Virginia Polytechnic Institute and State University and Wake Forest University in partial fulfillment of the requirements for the degree of

DOCTOR OF PHILOSOPHY
IN
BIOMEDICAL ENGINEERING

Kevin P. Granata, Ph.D., Past Chair

Shane D. Ross, Ph.D., Co-Chair
Maury A. Nussbaum, Ph.D., Co-Chair
J. Wallace Grant, Ph.D.
Deborah G. Heiss, Ph.D., DPT
James S. Thomas, Ph.D., P.T.

March 25, 2008
Blacksburg, Virginia

Key Words: Low Back Pain, Spinal Stability, Basin of Stability, Threshold of Stability, Lagrangian Coherent Structures

Biodynamic Analysis of Human Torso Stability using Finite Time Lyapunov Exponents

Martin L. Tanaka
Virginia Tech-Wake Forest University School of Biomedical Engineering and Sciences

ABSTRACT

Low back pain is a common medical problem around the world afflicting 80% of the population some time in their life. Low back injury can result from a loss of torso stability causing excessive strain in soft tissue. This investigation seeks to apply existing methods to new applications and to develop new methods to assess torso stability. First, the time series averaged finite time Lyapunov exponent is calculated from data obtained during seated stability experiments. The Lyapunov exponent is found to increase with increasing task difficulty. Second, a new metric for evaluating torso stability is introduced, the threshold of stability. This parameter is defined as the maximum task difficulty in which dynamic stability can be maintained for the test duration. The threshold of stability effectively differentiates torso stability at two levels of visual feedback. Third, the state space distribution of the finite time Lyapunov exponent (FTLE) field is evaluated for deterministic and stochastic systems. Two new methods are developed to generate the FTLE field from time series data. Using these methods, Lagrangian coherent structures (LCS) are found for an inverted pendulum, the Acrobot, and planar wobble chair models. The LCS are ridges in the FTLE field that separate two inherently different types of motion when applied to rigid-body dynamic systems. As a result, LCS can be used to identify the boundaries of the basin of stability. Finally, these new methods are used to find the basin of stability from time series data collected from torso stability

experiments. The LCS and basins of stability provide a richer understanding into the system dynamics when compared to existing methods.

By gaining a better understanding of torso stability, it is hoped this knowledge can be used to prevent low back injury and pain in the future. These new methods may also be useful in evaluating other biodynamic systems such as standing postural sway, knee stability, or hip stability as well as time series applications outside the area of biomechanics.

TABLE OF CONTENTS

LIST OF TABLES AND FIGURES 8

ACKNOWLEDGEMENTS 15

Chapter 1 Introduction 17

1.1 Low back pain 17

1.2 Spinal Stability 18

1.3 Current methods to measure torso stability 19

1.4 Basin of Stability 25

1.4 Document Organization 27

Chapter 2 Determining Torso Stability Using Time Series Averaged Lyapunov Exponents 29

2.1 Abstract 29

2.2 Introduction 29

2.2 Methods 30

2.2.1 Experimental Apparatus 30

2.2.2 Experimental Protocol 33

2.2.3 Lyapunov Stability Analyses 34

2.3 Results 38

2.4 Discussion 40

2.5 Summary and Conclusions 40

2.6 Acknowledgements 41

Chapter 3 Evaluation of the Threshold of Stability; A Pilot Study 42

3.1 Abstract 42

3.2 Introduction 43

3.2 Methods 45
3.2.1 Subjects 45
3.2.2 Set-up 46
3.2.3 Experimental Protocol 47
3.2.4 Analytical and Statistical Methods 49
3.3 Results 50
3.4 Discussion 52
3.5 Summary and Conclusions 53
Chapter 4 Locating Separatrices and Basins of Stability in a Reduced Order Model 55
4.1 Abstract 55
4.2 Introduction 56
4.2.1 Applications of LCS to Biomechanics 58
4.2.2 Sensitivity analysis and finite-time Lyapunov exponents 60
4.2.3 Determination of LCS 63
4.3 Mathematical Model 65
4.3.1 Planar Inverted Pendulum Model 67
4.3.2 Effective potential function 73
4.3.4 Model Calibration 75
4.4 Nonlinear Analysis 76
4.4.1 Deterministic and Conservative Simulation 76
4.4.2 Deterministic Simulation with Noise 82
4.4.3 Generation and Analysis of Simulated Experimental Data 85
4.5 Conclusions 93

4.6 Acknowledgments 94

Chapter 5 Mathematical Modeling and Simulation of the Planar Wobble Chair 95

5.1 Abstract 95

5.2 Introduction 96

5.2.1 History and properties of the Acrobot 97

5.2.2 Morphing the Acrobot into the Wobble Chair 103

5.3 Mathematical Model of the Planar Wobble Chair 104

5.3.1 Anthropometric Parameters 105

5.3.2 Planar Wobble Chair Model 108

5.4 Nonlinear Analysis 113

5.4.1 Analysis of the Deterministic Acrobot 115

5.4.2 Analysis of the Deterministic Planar Wobble Chair 121

5.4.3 Stochastic Analysis of the Planar Wobble Chair 129

5.4.3.1 Generation of trajectories 130

5.4.3.2 Euclidean distance method 132

5.4.3.3 State transition matrix method 132

5.4.3.5 Results - Euclidean distance method 135

5.4.3.6 Results – State Transition Matrix method 137

5.5 Discussion 141

5.6 Summary and Conclusions 142

Chapter 6 Determining the Basin of Stability through Wobble Chair Experiments 143

6.1 Abstract 143

6.2 Introduction 143

6.2.1 Basin of Stability and Effective Potential Function Relationship 144
6.2.2 Energy approach to the basin of stability 146
6.2.2 Generating both stable and unstable system behavior 148
6.3 Methods 148
6.4 Results 150
6.5 Discussion 159
6.6 Summary and Conclusions 160
Chapter 7 Summary and Conclusions 161
7.1 Research Summary and Conclusions 161
7.2 Future Work 163
LITERATURE CITED 165

LIST OF TABLES

Table 2.1: Main Effects Table……..……..…….. 38

Table 2.2: ANOVA Table. ……..…….. 38

Table 2.3: Tukey HSD test results. ……..…….. 38

Table 3.1: Results of threshold of stability experiment……..…….. 52

Table 4.1: Model Parameters for the Reduced Model……..…….…….. 76

Table 5.1: Segment and center of mass vectors……..……..…..…….…….. 103

Table 5.2: Lower body vector table……..…... 106

Table 6.1: Basin of stability volume. ……..……... 158

LIST OF FIGURES

Figure 1.1: Locations where low back pain is experienced ……. ……. 18

Figure 1.2: The number of "spinal stability" publications listed in PubMed is increasing…….. 19

Figure 1.3: Stabilogram displaying the movement of the center of pressure in an apparently random manner. …….. 21

Figure 1.4: In stability diffusion analysis the mean distance between two points separated in time is determined (a). Stabilogram-diffusion plots shows the short term and long term regions (b) (Collins and De Luca 1993). …….. 22

Figure 1.5: Unstable seated test apparatus (Radebold et al. 2001) …….. 23

Figure 1.6: Phase plot of a single planar pendulum. Nearly circular trajectories around the stable equilibrium points represent oscillating motion. Larger almost elliptical trajectories indicate higher amplitude oscillations. The undulating lines on the top and bottom represent circular orbits in a single direction. …….. 26

Figure 2.1: The wobble chair is a new seated stability test apparatus where movement of the lumbar spine is used to maintain balance. …….. 31

Figure 2.2: Two segment inverted pendulum model. …….. 33

Figure 2.3: Nearest neighbor to the reference point was found in n-dimensional state space. The distance between these two points is tracked as it evolves over time. The heteroclinic orbit indicates the separatrix between stable and unstable regions. …….. 36

Figure 2.4: The maximum Lyapunov exponent was determined by calculating the slope of the mean expansion as a function of the evolution time. …….. 37

Figure 2.5: The main effect of a) spring setting and b) week of testing is shown. In addition, the interaction c) between spring and week is presented. …….. 39

Figure 3.1: Participant balances on the wobble chair moving the lumbar region of her torso to maintain stability. …….. 44

Figure 3.2: The wobble chair has four stabilizing springs that can be set to different distances to control the amount of restorative torque applied to the participant. …… 47

Figure 3.3: The threshold of stability was found by locating the lowest passing spring setting. In this case 45% ∇G for eyes open and 65% ∇G for eyes shut. …….. 50

Figure 3.4: The lower body angle (blue) shows large variability and the upper body (green) variability is smaller. …….. 51

Figure 3.5: After an initial adjustment at the beginning of the trial, the upper body angle, θ_1, generally stabilized and motion was dominated by the lower body, θ_1. An RMS value of 3.0 degrees (red circle) was found for the θ_1 direction. In the θ_2 direction, the RSM value was 2.0 degrees. 51

Figure 4.1: The state transition matrix is a deformation gradient about the reference trajectory describing how an initially spherical blob of surrounding particles deforms into an ellipsoid. 61

Figure 4.2: Flow chart depicting how the LCS are traditionally determined..... 63

Figure 4.3: The divergence of two points on opposite sides of a separatrix is larger than the divergence of points on the same side. This generates a ridge in the FTLE field at the separatrix. 64

Figure 4.4: The wobble chair is an apparatus designed to isolate the movement of the low back to determine torso stability (Adapted from (Cholewicki et al. 2000; Tanaka and Granata 2007)) 66

Figure 4.5: The reduced order model of the wobble chair consists of a planar inverted pendulum with stabilizing springs and a limited gain control. 68

Figure 4.6: The effective potential energy function is the sum of the individual components. Under some conditions, a potential well develops near the equilibrium point. 72

Figure 4.7: The effective potential energy function is the sum of the individual components. Under some conditions, a potential well develops near the equilibrium point. 74

Figure 4.8: Orbits and flow map for the deterministic conservative configuration. Lines ending with a point show the resulting trajectories based on the initial conditions. The heteroclinic orbit is a separatrix between the stable and unstable regions. 77

Figure 4.9: The 3D view shows the LCS to be easily observable as ridges in the FTLE field. This plot was generated from a 200 by 200 point grid over a range of ±15 degrees by ± 15 deg/sec. 78

Figure 4.10: LCS form separatrices in the forward time flow (T = 3 seconds). Locations of the LCS matches well with the heteroclinic orbit and its isoenergy lines. 80

Figure 4.11: LCS form separatrices in the backward time flow. Locations of the LCS match well with the heteroclinic orbit and its isoenergy lines. 81

Figure 4.12: The flow map evolved over 0.3 seconds for the damped system with noise is plotted simultaneously with the orbits for the conservative deterministic configuration… 82

Figure 4.13: The location of the LCS aligns well with the lines of the heteroclinic orbit in the forward time flow damped system with noise. Although the flow is more diffused than the conservative noise free system, the results are essentially the same. 83

Figure 4.14: The backward time flow analysis shows LCS that also align well with the lines of the heteroclinic orbit for the damped system with noise. ……..…….. 84

Figure 4.15: The LCS can be easily observed in a 3 dimensional plot of (Figure 4.13)…. 84

Figure 4.16: The time-series data analyzed came from several simulated experimental trials. ……..…….. 85

Figure 4.17: The maximum FTLE is found by calculating the growth of perturbation vectors in multiple state space directions. The assumption is made that the maximum FTLE dominates the evolution of the perturbation vectors. ……..…….. 87

Figure 4.18: Values for the finite time Lyapunov exponents were stored in a location midway (green) between each reference (blue) and each nearest neighbor (yellow). These values were used to generate the FTLE field in state space. ……..…….. 88

Figure 4.19: At an evolution time of T = 0.6 seconds the LCS is observable near the ejection points in state space. ……..…….. 90

Figure 4.20: By T = 1.2 seconds the LCS is clearly observable spanning more of the boundary. ……..…….. 91

Figure 4.21: By T = 1.2 seconds the LCS is clearly observable spanning more of the boundary. ……..…….. 92

Figure 4.22: FTLE field at an evolution time, T = 2.4 seconds. …….…….. 93

Figure 5.1: The Acrobot (acrobatic robot) is patterned after a gymnast on a high bar (a). Actuation occurs only at the middle joint (hip) with the first joint (hands) being free to spin about its axis (Murray and Hauser 1991) ……... 98

Figure 5.2: Equilibrium manifold for the Acrobot. Balanced parameter values were 0.5, 1, 8, 8, and 10 for the length of segment 1, length of segment 2, mass of segment 1, mass of segment 2, and acceleration of gravity, respectively. Actual parameters were 0.5, 0.75, 7, 8, and 9.8 respectively (Murray and Hauser 1991) …..…….. 99

Figure 5.3: Equilibrium manifold for the physical Acrobot (Bortoff 1992). Note that the axes are switched when compared with Figure 5.2. ……..…….. 100

Figure 5.4: Basin of stability for (a) the balanced Acrobot (Murray and Hauser 1991) and (b) the physical Acrobot (Bortoff 1992). ……... 102

Figure 5.5: Center of mass and segment vectors for the Acrobot were slowly changed to those of the wobble chair. This effectively morphed one model into the other. …..…... 104

Figure 5.6: Model of the person sitting on the wobble chair. Blue components contribute to segment one. Green components make up segment 2. The joints are shown in red and the springs in aqua. ……..……... 105

Figure 5.7: Vectors were used to find the locations of the center of mass of each body segment. ……... 106

Figure 5.8: Simplified model of the person sitting on the wobble chair. Position vectors, $\bar{L}_1$ and $\bar{L}_2$, show the connectivity of the model. Vectors $\bar{c}_1$ and $\bar{c}_2$ are from the joint to the center of mass of each segment. In the initial balanced configuration shown, the segment angles $\theta_1$and θ_2 are set to zero. 108

Figure 5.9: Poincaré section is a (θ_1, θ_2) slice of state space while the angular velocities $(\dot{\theta}_1, \dot{\theta}_2)$ are near zero. 115

Figure 5.10: Simulation results showing that PD controller drove the center of mass to near the equilibrium manifold. 116

Figure 5.11: Time plot for the upper and lower segments of the Acrobot. 117

Figure 5.12: Phase plot for the upper and lower segments of the Acrobot. 117

Figure 5.13: The blue line show the location of the equilibrium manifold. Circles show initial locations where trajectories remained in the neighborhood of the origin. Crosses represent initial locations that resulted in unstable trajectories. 119

Figure 5.14 – LCS are visible in both the (a) top view and (b) 3D view of the FTLE field for the Acrobot. 120

Figure 5.15: Equilibrium manifold for the wobble chair. The box indicated the region that is attainable in wobble chair experiments. Results are plotted on the zero velocity plane $(\dot{\theta}_1 = \dot{\theta}_2 = 0)$. 122

Figure 5.16: Simulation results showing that PD control drove the center of mass to the equilibrium manifold. 123

Figure 5.17: Time plot for the upper and lower segments of the wobble chair. 123

Figure 5.18: Phase plot for the upper and lower segments of the wobble chair. 124

Figure 5.19: Global view of the basin of stability based on the outcomes of trajectories. Circles show initial locations where trajectories remained in the neighborhood of the origin. Crosses represent initial locations that resulted in unstable trajectories. 125

Figure 5.20: In the θ_1, θ_2 plane, LCS are visible in both the (a) top view and (b) 3D view of the FTLE field for the wobble chair. The equilibrium manifold (black line), LCS (ridges), and stable trajectory evolutions (circles) were all observed to correlate well. 126

Figure 5.21: In the θ_1 phase plane, a depression in the FTLE field is observed to the upper right of the origin in the (a) top view. A (b) 3D view of the FTLE field for the wobble chair is also shown. 127

Figure 5.22: In the θ_2 phase plane, a depression in the FTLE field is observed a little closer to the origin in the (a) top view. A (b) 3D view of the FTLE field for the wobble chair is also shown. ……..……..…….... 128

Figure 5.23: Simulation results showing the location of the center of mass over 50 trials. The PD controller drove the system towards the equilibrium manifold. …..……... 131

Figure 5.24: Time plot for the upper and lower segments of the wobble chair. Both stable and unstable dynamics are visible. ……..…….... 131

Figure 5.25: Phase plot for the upper and lower segments of the wobble chair. Both stable and unstable dynamics are visible. Stable behavior occurs within ~4 degrees of the origin (see 5.24). ……..……..……..…….... 132

Figure 5.26: The state transition matrix was calculated by first forming a basis about the reference point using nearly orthogonal vectors, then tracking the trajectories forward in time (Δt) and determining the changes in the basis vectors. ……..…….....……... 133

Figure 5.27: Graphical representation of the terms that make up the gradient of the state transition matrix. ……..……..…..…….... 134

Figure 5.28: FTLE field for the wobble chair generated using the Euclidean distance method. This two dimensional plot shows the zero velocity section of the four dimensional system. Poincaré section width was 50% of the range of the data. ……. 135

Figure 5.29: FTLE field for the wobble chair generated using the Euclidean distance method. This two dimensional plot shows the $(\theta_1, \dot{\theta}_1)$ slice of state space. The position and velocity of θ_2 is reduced to a 10% band around $(\theta_2 = 0, \dot{\theta}_2 = 0)$. ……....……... 136

Figure 5.30: FTLE field for the wobble chair generated using the Euclidean distance method. This two dimensional plot shows the $(\theta_2, \dot{\theta}_2)$ slice of state space. The position and velocity of θ_1 is reduced to a 10% band around $(\theta_1 = 0, \dot{\theta}_1 = 0)$. ……..……... 136

Figure 5.31: FTLE field for the wobble chair generated using the state transition matrix method. This two dimensional plot shows the zero velocity section of the four dimensional system. 100% of the available data is shown. ……..…..…….…... 137

Figure 5.32: FTLE field for the wobble chair generated using the state transition matrix method. This two dimensional plot shows the $(\theta_1, \dot{\theta}_1)$ slice of state space. The position and velocity of θ_2 is reduced to a 10% band around $(\theta_2 = 0, \dot{\theta}_2 = 0)$. ……..…....…... 138

Figure 5.33: FTLE field for the wobble chair generated using the state transition matrix method. This two dimensional plot shows the $(\theta_2, \dot{\theta}_2)$ slice of state space. The position and velocity of θ_1 is reduced to a 10% band around $(\theta_1 = 0, \dot{\theta}_1 = 0)$. ……....……... 139

Figure 5.34: The 2-dimensional figures are arranged into a two dimensional grid. By comparing the figures at different grid locations, the full four dimensional basin of stability can be visualized (see associated document, "4D Basin of Stability") ……..…….. 140

Figure 6.1: Schematic diagram showing the effect of spring setting on the basin of stability and the kinematic variability. ……...…..…….……... 145

Figure 6.2: When spring distance is reduced to a point where kinetic energy due to random perturbations exceeds effective potential energy, the system can exhibit unstable behavior. ……...…..…….……... 146

Figure 6.3: When kinetic energy (red) exceeds effective potential energy (black) unstable behavior occurs (http://en.wikipedia.org/wiki/Image:DisNormal06.svg) ……..... 147

Figure 6.4: Human body planes. During the experimental trials, motion was focused in the sagittal plane (http://en.wikipedia.org/wiki/Core_%28anatomy%29). ……... 149

Figure 6.5: FTLE field for participant #3 with eyes open generated using state transition matrix method. This two dimensional plot shows the zero velocity section of the four dimensional system. A bounding box was drawn (black dashed lines) to approximate the dimensions of the basin of stability. ……...…..……..……... 151

Figure 6.6: FTLE field for participant #3 with eyes open generated using the state transition matrix method. This two dimensional plot shows phase space of θ_1. A bounding box was drawn (black dashed lines) to approximate the dimensions of the basin of stability. ……...…..……..……... 152

Figure 6.7: FTLE field for participant #3 with eyes open generated using the state transition matrix method. This two dimensional plot shows the phase space of θ_2. A bounding box was drawn (black dashed lines) to approximate the dimensions of the basin of stability. ……...…..……..…….……... 153

Figure 6.8: FTLE field for participant #3 with eyes shut generated using the state transition matrix method. This two dimensional plot shows the zero velocity section of the four dimensional system. The bounding box drawn (black dashed lines) to approximates ¼ of the basin of stability. The full basin is assumed to by symmetric with respect of the origin in $\theta_1$and θ_2. ……...…..…….……... 155

Figure 6.9: FTLE field for participant #3 with eyes shut generated using the state transition matrix method. This two dimensional plot shows the phase space of θ_1. …… 156

Figure 6.10: FTLE field for participant #3 with eyes shut generated using the state transition matrix method. This two dimensional plot shows the phase space of θ_2. ……... 157

ACKNOWLEDGEMENTS

The author would like to thank his past advisor, Dr. Kevin Granata, for his support and guidance on this research. Sadly, Dr. Granata was killed while working at Virginia Tech on April 16th, 2007. His invaluable encouragement and support allowed this research to be developed. The author hopes that somewhere Dr. Granata is smiling as he sees this work come to fruition.

The author would like to express his gratitude to Dr. Shane Ross and Dr. Maury Nussbaum who have provided numerous hours of advice and encouragement. Thank you for your support, guidance, and genuine interest. Dr. Ross, your knowledge has given the author a new "mathematical" perspective on the world, and what an interesting view it is. Dr. Nussbaum, thank you for the clarity you brought to the author's endeavors. Your ability to simplify seemingly complex problems is a gift. The author would also like to acknowledge the contributions of Dr. Wallace Grant, who has been a wonderful support to the author and a true friend. Thank you.

Special thanks are extended to the Ohio based researchers. Dr. Jim Thomas has given much needed advice and direction to the author. In addition, the author is grateful for Dr. Deborah Heiss's financial support, encouragement, flexibility, and advice. Your positive attitude and smile were much appreciated. Last, the author would like his committee to know that each member has been vital in the completion of this work. For all your support and guidance, the author will be eternally grateful.

Dedicated to my wife, Dana,
and my boys,
Nicholas, Andrew, William, and Michael

Chapter 1

Introduction

1.1 Low back pain

Low back pain is a common medical problem around the world, afflicting 80% of the population at some time in their life (Kelsey and White 1980; Reeves et al. 2005). It is the second most common reason that people seek medical attention, second only to colds or flu (MedlinePlus 2007). Low back pain (LBP) is an enormous problem in the United States. It is estimated that Americans spend over $50 billion on LBP annually (NINDS 2007). LBP is classified as a neurological disorder by the National Institute of Health (NIH) which supports low back pain research through the National Institute of Neurological Disorders and Strokes (NINDS). Back pain is the second most common neurological ailment in the United States led only by headaches (NINDS 2007). The debilitating nature of low back pain reduces the quality of life for those that suffer from its effects. According to NINDS, low back pain is "the most common cause of job-related disability". LBP is common in the US and Europe with point prevalences estimated to be 5.6% in North America, 13.7% in Denmark, 28.7% in Canada, and 19% in the UK (Loney and Stratford 1999; Kent and Keating 2005). In addition, LBP imposes a substantial burden in the developing world where loss of wages and productivity interferes with daily activities (Galukande et al. 2006).

The causes of low back pain are elusive, and it is likely that many different factors elicit similar symptoms. Cailliet (2003) identified seven sites for pain generation: external fibers of the intervertebral disc, posterior longitudinal ligament, nerve root dural sheath, synovial capsule of the facets, interspinous and supraspinous ligaments, erector spinae muscle, and fascia of the muscles (Figure 1.1). Although no definite cause of LPB has been identified, research interests continue to focus on spinal instability as an underlying factor.

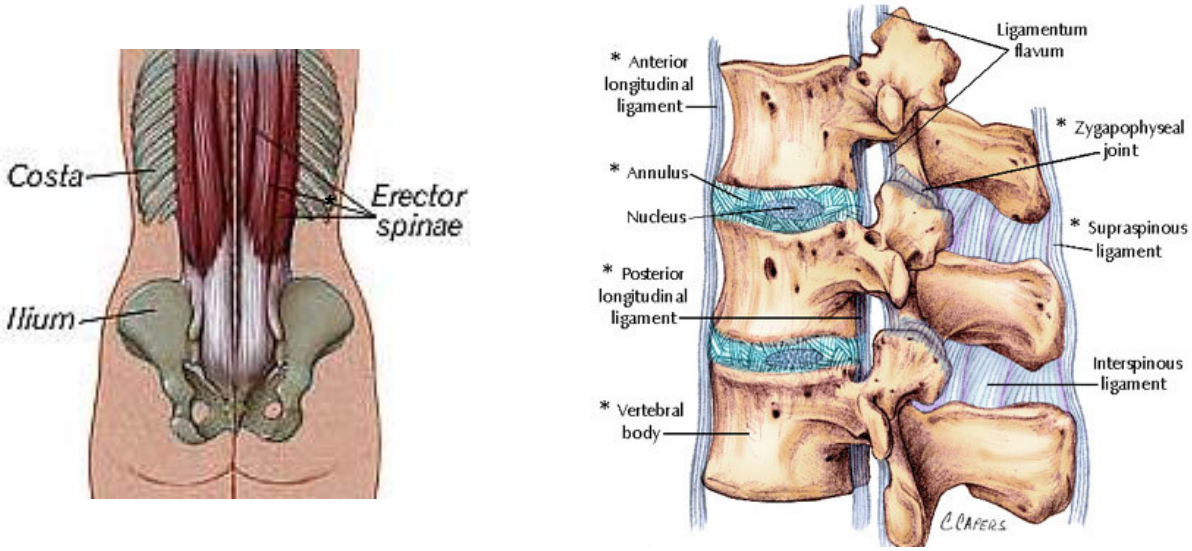

Figure 1.1: Locations where low back pain is experienced.

1.2 Spinal Stability

Instability of the human spine has long been thought to be an indicator of the risk of low back injury. In 1961, Lucas conducted one of the earliest documented experiments on spinal stability (Lucas and Bresler 1961). The amount of spinal stability research has steadily increased over the years. A current search (6-23-07) of PubMed resulted in 2611 articles on spinal stability ranging from 1963 to the present (Figure 1.2), including 94 articles already published this year. Despite all of the research into spinal stability, a clear link between spinal stability and low back injury does not yet exist. One possibility is that global instability of the spine may lead to

excessive strain at both the global and local level. Excessive local deformation may result in muscle strains and ligament sprains in the lumbar region (McGill 2001). This may initiate an inflammatory response stimulating nociceptors in the region causing low back pain (Preuss and Fung 2005). The term spinal stability is often used interchangeably with torso stability when referring to the core stability in the lumbar region. However, to some people spinal stability may imply the stability obtained from passive stiffness associated with the ligamentous spine only. In order to avoid this confusion, this document will predominately use the term torso stability since it implies the addition of active neuromuscular control.

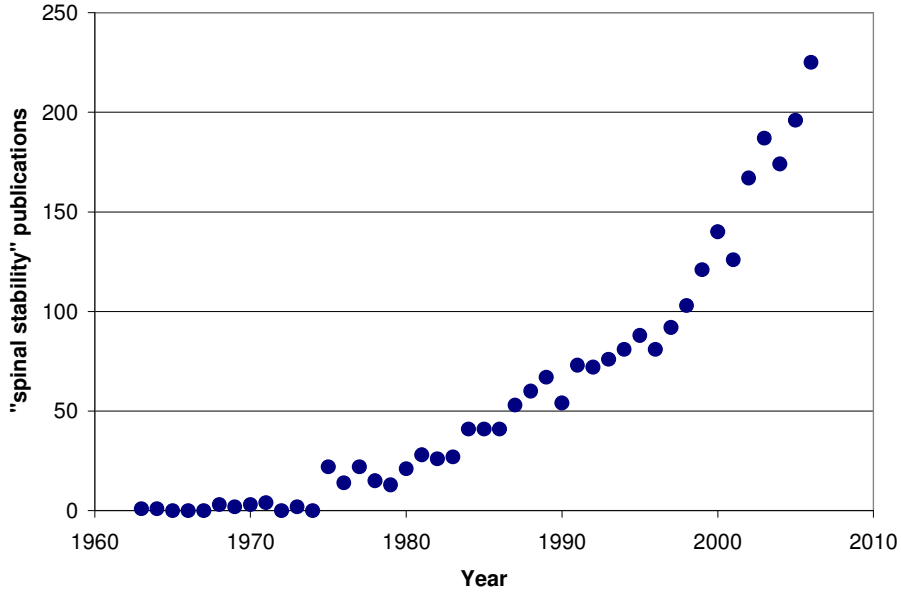

Figure 1.2: The number of "spinal stability" publications listed in PubMed is increasing, indicating that LBP research is becoming increasing more supported.

1.3 Current methods to measure torso stability

Like low back pain, stability is not easily defined (Adams 2007; Reeves et al. 2007a; Reeves et al. 2007b). The first division is between static stability and dynamic stability. For the torso to be statically stable, the destabilizing forces that drive the torso away from an equilibrium

position must be less than the restorative forces in the system. When the destabilizing forces exceed the stabilizing forces, buckling of the spine may occur. Several researchers have applied this methodology to study the spine (Lucas and Bresler 1961; Granata and Orishimo 2001; McGill 2001; Stokes and Gardner-Morse 2001; Van Dieen et al. 2003; Brown and McGill 2005).

Dynamic stability, in contrast, evaluates moving systems rather than static systems with the potential to move. Standing postural sway (Winter 1990; Winter et al. 2001) and gait (Mcgeer 1990; Goswami 1996; Garcia et al. 1998) are two common applications of dynamic stability. Parameters used as indicators of dynamic stability in biomechanics fall into two general categories. The first category is kinematic variability, which includes parameters such as mean center of pressure, 95% ellipse area, root mean squared displacement, etc. These kinematic parameters give an indication of range of motion, but they are not true indicators of stability. The second category includes true stability parameters. Some of these parametric methods include stability diffusion analysis (Collins and De Luca 1993; Peterka 2000), rescaled range analysis (Delignieres et al. 2003), detrended fluctuation analysis (Delignieres et al. 2003; Gates and Dingwell 2007), and Lyapunov Stability Analysis (Dingwell et al. 2000; England and Granata 2006; Granata and England 2006; Kang and Dingwell 2006).

Stability diffusion analysis was introduced by Collins and De Luca (1993) as a new way to evaluate stability of standing postural sway data. This method employs mathematical techniques from statistical mechanics to evaluate stabilograms. A stabilogram is a plot of the path of the center of pressure as it moves over time. In order to more easily understand the concept, first consider the similarities between a stabilogram and a random walk. The stabilogram appears to move randomly in any direction but also seems to cluster about an equilibrium point near the vertical position (Figure 1.3).

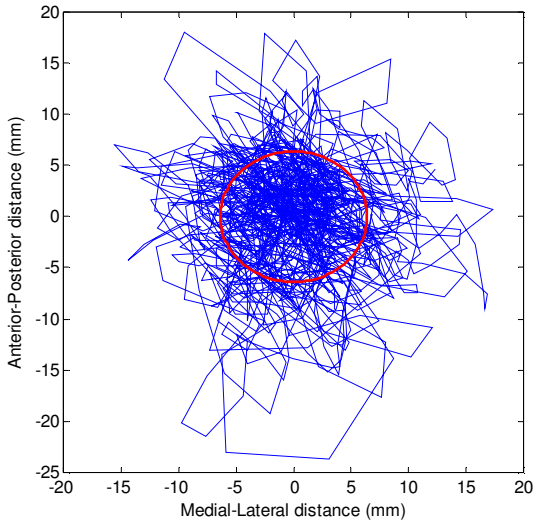

Figure 1.3: Stabilogram displaying the movement of the center of pressure in an apparently random manner.

In a true random walk, motion at each time step is in a random direction, and overall, displacement will occur. A random walk where the time step approaches zero approximates Brownian motion. Einstein (1905) showed that the mean square of the displacement, Δx, of a particle under one-dimensional Brownian motion is related to the length of time elapsed, Δt, by:

$$\left\langle \Delta x^2 \right\rangle = 2D\Delta t \tag{1.1}$$

where D is the diffusion coefficient. In 1968, Mandelbrot extended the concept of classical Brownian motion by introducing fractional Brownian motion (Mandelbrot and Van Ness 1968). Placed in the framework of fractional Brownian motion, Einstein's original equation may be written as:

$$\left\langle \Delta x^2 \right\rangle \sim \Delta t^{2H} \tag{1.2}$$

where H is a scaling exponent equal to ½ . However, the value of H may range from 0 to 1 in fractional Brownian motion. Values of H greater than ½ represent a positive correlation with previous motion and are indicative of persistent behavior. An example of persistent behavior is

the effect of inertia on a system. Conversely, values of H less than ½ represent a negative correlation with previous motion and are indicative of anti-persistent behavior. Anti-persistent behavior is common in a controlled system that drives motion to a set point.

Stability diffusion analysis was used by Collins and De Luca to analyze time series data (Figure 1.4). The distance between two points in the time series separated by a time interval, Δt, was calculated and the mean value determined. This process was repeated for different time intervals. A log-log plot (similar to 1.4b) was used to determine the short and long term scaling exponents, H_{st} and H_{lt}, respectively. Collins and De Luca found the average value of H_{st} to be approximately 0.75 indicating short term persistent behavior and the average value of H_{lt} to be approximately 0.25 indicating long term anti-persistent behavior.

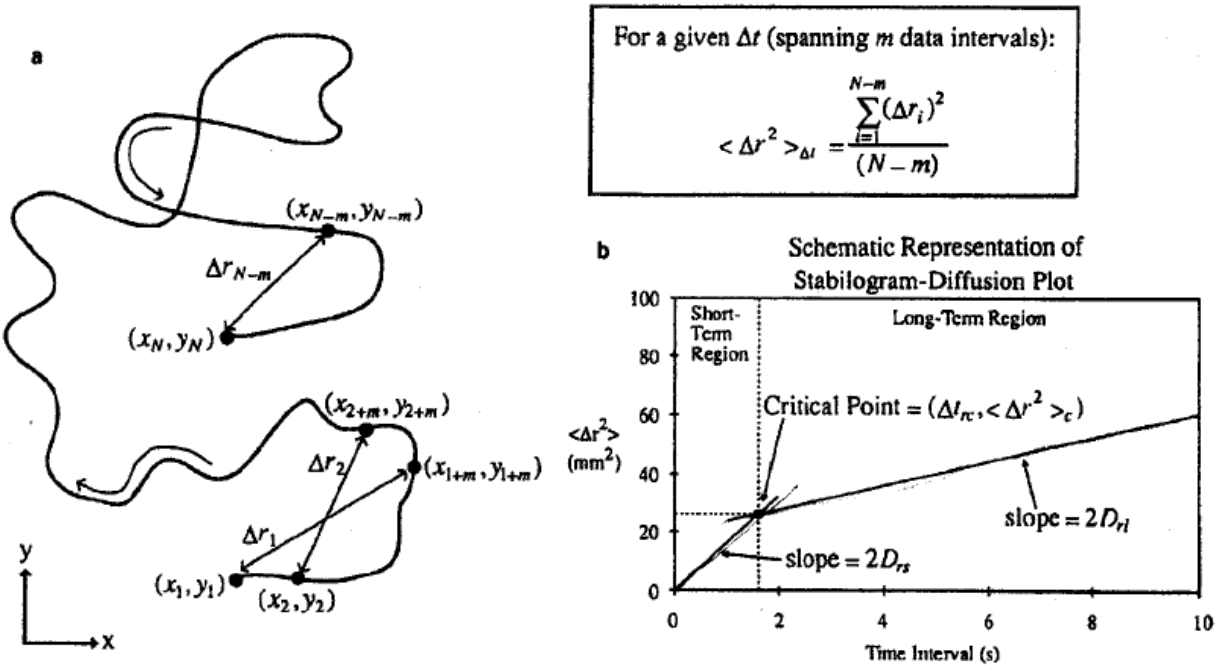

Figure 1.4: In stability diffusion analysis the mean distance between two points separated in time is determined (a). Stabilogram-diffusion plots shows the short term and long term regions (b) (Collins and De Luca 1993).

Although stability diffusion is still commonly measured, questions have been raised about the use of stability diffusion analysis stating that it is a statistical artifact (Delignieres et al. 2003). Collins and De Luca (1993) explained the short term and long term regions by open and closed loop control, respectively. The main argument against this explanation was that two distinct regions may not be present and that the flattening of the diffusion plot may instead be caused by reaching the boundaries of the system. In other words, when diffusion expands to fully fill the available space, no further diffusion is possible. Delignieres (2003) suggested using more traditional approaches such as rescaled range analysis or detrended fluctuation analysis.

Radebold and Cholewicki (2000; Radebold et al. 2001) conducted seated stability tests on the lumbar spine using hemispherical balls attached to the bottom of a seat (Figure 1.5). This apparatus isolated motion to the lumbar spine. The location of the center of pressure (COP) of the subject was measured during the test using a force plate. Stability was analyzed using the stability diffusion function (Collins and De Luca 1993).

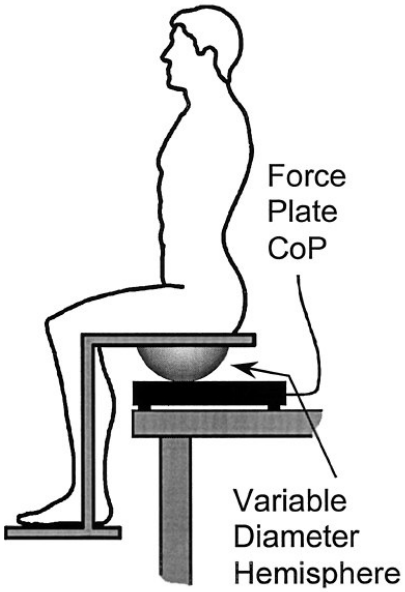

Figure 1.5: Unstable seated test apparatus (Radebold et al. 2001)

The research described herein utilized a new seated stability apparatus based upon the design of Radebold and Cholewicki. The apparatus allowed for more control over the level of static stability by providing a continuously adjustable range of restorative torque. However, rather than using stability diffusion, dynamic stability was calculated through evaluation of the finite time Lyapunov exponents (FTLE). Lyapunov exponents have been used to evaluate gait dynamics (Dingwell et al. 2000; England and Granata 2006) and body movements (Granata and England 2006) but have not been applied to lumbar stability experiments.

Lyapunov stability analysis is based on the Ph.D. dissertation of Aleksandr Lyapunov in 1892 (Smirnov 1992; Jury 1996). His theory on dynamic stability states that if one starts near an equilibrium point (within δ), and the system can be described by a Lyapunov function, then the state of the system will always remain close to the equilibrium point (within ε). Lyapunov stability is a weaker form of stability than asymptotic stability, as the latter requires the system to approach the equilibrium point. Exponential stability is an even stronger form of stability specifying that the rate of stability must be exponential. Because of its generality, Lyapunov stability has become one of the leading methods used to assess dynamic stability in a variety of applications.

In real application, however, it is not practical to evaluate stability for an infinite amount of time. When Lyapunov exponents are calculated over a finite time period, they are denoted as finite time Lyapunov exponents (FTLE). FTLE have been used to predict capsizing of ships (Mccue and Troesch 2006), analyze fluid dynamics (Evans et al. 1990; Vastano and Moser 1991; Lapeyre 2002; Shadden et al. 2005), predict weather (Yoden and Nomura 1993), assess stability of biped robots (Yang and Wu 2006), and detect ventricular tachycardia or fibrillation (Wessel et al. 1998).

In practical application, it is common to calculate FTLE using linearized perturbation equations. Some researchers have investigated higher order models (Sano and Sawada 1985; Brown et al. 1991; Okushima 2003), but these have been applied primarily to classical chaotic systems (Lorentz attractor, Roessler equation, Henon map, etc) with less emphasis on real applications.

A common method to calculate the linearized FTLE is to determine the rate of separation (Euclidean distance) of two nearest neighbors in n-dimensional state space (Rosenstein et al. 1993a). Another less common method is to calculate the FTLE by evaluating the rate of expansion of a n-dimension hyper-ellipse (Shadden et al. 2005). A variation of each of these methods will be developed in this proposal to determine the stability of the spine.

1.4 Basin of Stability

A parameter related to the threshold of stability is the basin of stability. Unlike the threshold of stability, the basin of stability is not a new term (Ashby 1962). The basin of stability defines a region in state space where stable behavior exists. The previously reported research evaluated stability only within the stable region of state space. In order to find the basin of stability, the methods described in later chapters will extend the experiments into the unstable region. In doing so, the boundary between stable and unstable behavior may be found which defines the edge of the basin of stability.

The basin of stability can be more easily visualized in state space by considering the motion of a pendulum (Figure 1.6). The pendulum is at the stable equilibrium point when it is pointing directly downward. It is at the unstable equilibrium point when it is pointing directly upward. Small oscillations of the pendulum are shown on the phase plot as small almost circular paths around the stable equilibrium points. This motion of a swinging pendulum generates

trajectories that move in a clockwise direction. Larger amplitude oscillations are observed on the phase plot as larger less-circular trajectories. The maximum amplitude of oscillation occurs when the pendulum begins its motion starting from a very small angle from the upright position. This motion begins very slowly. By the time the pendulum reaches a few degrees, it begins to move more quickly. It passes through the directly downward position at maximum velocity and then slows down again as it approaches the upright position from the other side. In theory, as the initial angle from the vertical position approaches zero, the orbit time approaches infinity. This special orbit is the homoclinic orbit.

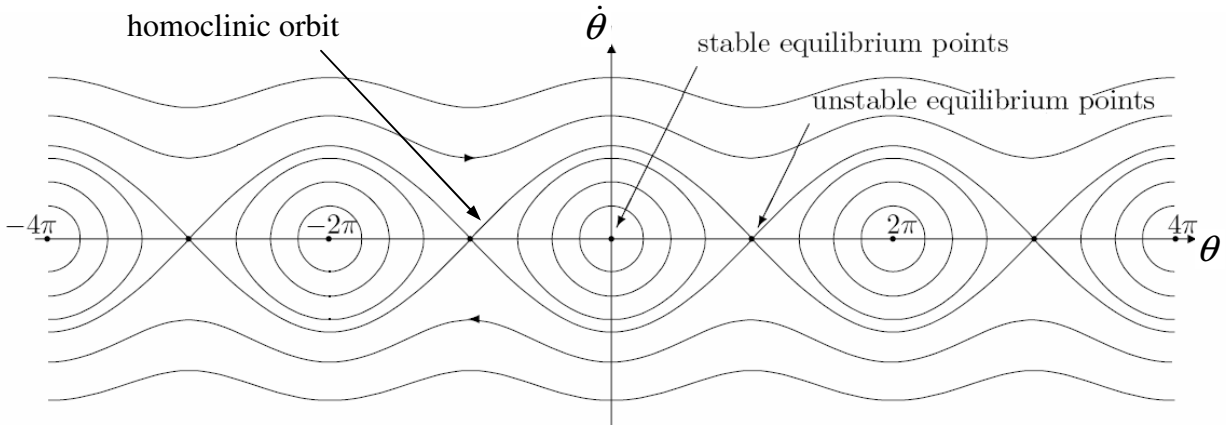

Figure 1.6: Phase plot of a single planar pendulum. Nearly circular trajectories around the stable equilibrium points represent oscillating motion. Larger almost elliptical trajectories indicate higher amplitude oscillations. The undulating lines on the top and bottom represent circular orbits in a single direction.

The undulating lines beyond the homoclinic orbit (on the top and bottom of Figure 1.6) represent circular orbits in a single direction. In this case, the pendulum no longer oscillates since it has enough energy when it reaches the upright vertical position to continue its motion in the same direction. Clearly, the oscillatory motion is very different than the orbiting motion.

The two types of motion are separated by the homoclinic orbit which acts as a separatrix. The separatrix can also be used to separate other types of dynamics such as stable and unstable behavior. In later chapters, separatrices will be found that locates the basin of stability in state space.

The magnitude of the basin of stability has been discussed in papers on gait dynamics, (Garcia et al. 1998; Schmitt 2006) but no explicit plots were shown. One method to determine the basin of stability is through Lagrangian coherent structures (LCS). LCS are defined as the ridges of the spatially distributed Finite-Time Lyapunov Exponent (FTLE) field. The LCS form a separatrix that can be used to determine the boundary of the basin of stability.

1.4 Document Organization

This dissertation has been divided into chapters, some of which can exist as stand alone documents. Chapter one introduces the topic of low back pain, describes how LBP is associated with spinal stability, and describes the current methods used to evaluate biomechanical stability. Chapter two describes an experiment to measure torso stability using existing methods. Specifically, the (time series averaged) Lyapunov exponent which has been used for evaluation of dynamic systems is evaluated. In chapter three, a new metric for evaluating torso stability is introduced, i.e. the threshold of stability. In this study, subjects are tests under two conditions, normal and limited feedback to the postural control system. Differences in the threshold of stability are evaluated. In addition, the time series averaged Lyapunov exponent is calculated for comparison. In chapter four, mathematical models are developed for the inverted pendulum, a reduced order system. This simple system shares some of the characteristics of the wobble chair. Methods are developed to generate Lagrangian coherent structures (LCS), some of which define

the location of the basin of stability. In particular, a new method is developed to find LCS from time series data without the need for a vector field which is often unavailable in biodynamic experiments. In chapter five, the methods developed in chapter four are extended to analyze a planar wobble chair. An aside is taken to evaluate the Acrobot , a similar dynamic system, using the newly developed methods. This provides insight into the system dynamics and a connection with previous research. A mathematical model for the wobble chair is developed and anthropometric parameters are used for model calibration. Deterministic and stochastic simulations are executed and analyzed to find the LCS and basin of stability. In addition, a new technique to calculate the maximum finite time Lyapunov exponent from time series data using the state transition matrix is developed. Using this new method to evaluate simulated experimental data, LCS and basins of stability are found for the wobble chair. In chapter six, these new methods are applied to real experimental data collected from human participants. LCS and basins of stability are found from these data providing a richer understanding of the system dynamics than the traditional methods of calculating the time series averaged FTLE employed in chapter two.

Chapter 2

Determining Torso Stability Using Time Series Averaged Lyapunov Exponents

2.1 Abstract

Mechanical assessment of torso stability is a valuable tool for identifying individuals at risk for low-back pain. The apparatus is designed to challenge the stabilizing control of subjects in order to quantify torso stability. In addition, a method is outlined for calculating the maximum Lyapunov exponent from the measured data. The results showed a significant negative correlation between chair stability and the maximum Lyapunov exponent, and good trial repeatability. The method was found to be sensitive to changes in stability and indicates that it may be a useful method to analyze the effects of fatigue, static flexion, or interventions such as physical therapy on torso stability.

2.2 Introduction

Low back pain is a common condition afflicting more than 80% of the population during their lifetime (Kelsey and White 1980; Reeves et al. 2005). The human spine consists of a column of vertebrae separated by discs and surrounded by ligamentous and muscular tissue.

Damage can occur when the tissues of the spine are exposed to excessive strain (Adams and Dolan 1995) that may result from unstable buckling of the vertebral column (Preuss and Fung 2005). Direct measurements of buckling loads often results in destruction of the test specimen. Since direct spinal buckling tests cannot be performed on human subjects, a method to non-destructively evaluate spinal column buckling was sought. Buckling is unlikely when the spinal column is able to maintain a stable upright configuration. Thus, torso stability may be used as an indicator of risk. Previous research has shown that stability of the torso is a valuable tool for identifying individuals at risk of low-back pain (Radebold et al. 2001). Cholewicki (2000) directed subjects to sit on a unstable seat with a hemisphere attached to the bottom. Task difficulty was modulated by adjusting the radius of curvature upon which the seat pan balanced, effectively altering the restorative moment. Nonlinear time-series analyses of the seat movements were used to estimate stability.

The experimental design in the current study modified the earlier methods to modulate the mechanical static stability of the unstable seat then observes the time-domain stabilizing performance of a human subject while sitting on this device. In addition, the analysis method was expanded to compute stability through Lyapunov analyses of the measured data.

2.2 Methods

2.2.1 Experimental Apparatus

The wobble chair is a new seated stability testing apparatus consisting of a seat mounted on a thin, flat seat pan supported by a ball joint (Figure 2.1). This allows the seat pan to pivot

freely in 2-dimensions about its geometric center. The seat can be adjusted forward and backward on the seat pan to assure the subject's center of mass is directly over the pivot point. Steel springs are located to the front, rear, left, and right of the center. The springs were selected such that the free length is equal to the distance from the base to the seat pan of the wobble chair at the neutral position (Figure 2.1).

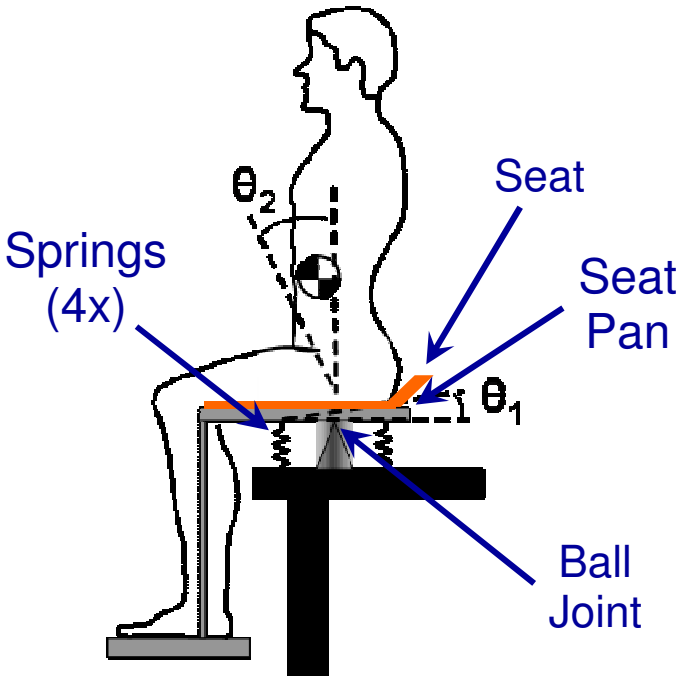

Figure 2.1: The wobble chair is a new seated stability test apparatus where movement of the lumbar spine is used to maintain balance.

The rotational stiffness can be adjusted by changing the distance from the springs to the central ball joint. Restorative 2-D moment $\vec{M}$ is,

$$\vec{M} = \vec{\vec{P}}\,\vec{\theta}_S, \quad p = k \cdot d^2$$
$$\begin{Bmatrix} M_{AP} \\ M_{ML} \end{Bmatrix} = \begin{bmatrix} p & 0 \\ 0 & p \end{bmatrix} \begin{Bmatrix} \theta_{AP\_S} \\ \theta_{ML\_S} \end{Bmatrix} \tag{2.1}$$

where $\vec{\theta}_S$ is the 2-D angle vector of the seat, composed of the anterior-posterior angle θ_{AP_S} and the medial-lateral angle θ_{ML_S}. The proportional gain constant, *p*, is a function of the spring stiffness, *k*, and the distance, *d*. The proportional gain matrix, $\vec{\vec{P}}$, has diagonal elements equal to p. Since the moment is proportional to the square of the spring distance, a larger range of proportional gain can be achieved. Static stability is decreased by reducing the stabilizing restorative moment (i.e. proportional gain provided by the springs). This is achieved by moving the springs closer to the center. The wobble chair's continuous range of gain, $\vec{\vec{P}}$, allows the level of static stability to be normalized to body mass and weight distribution. The gravitational moment, $\vec{M}_g$, about the ball joint can be measured for an individual subject. The gravitational gradient, ∇G, is a measure of the mass and weight distribution of an individual given by,

$$\nabla G = \partial \big/ \partial \vec{\theta}_S \; \vec{M}_g(\vec{\theta}_S, \vec{\theta}_T) \tag{2.2}$$

where, $\vec{\theta}_T$ is the 2-D angle to the torso. Neutral stability is achieved when the proportional gain produced by the spring's restorative force is equal to and offsets the gravitational gradient. This condition is defined as a spring setting of 100%. At spring settings greater than 100%, the stabilizing moment generated by the springs is greater than the destabilizing gravitational moment. The system is attracted toward the neutral position and is statically stable. For spring settings less than 100% the destabilizing gravitational moment is greater than the stabilizing spring moment. Upon small perturbations from the neutral position the system is repelled from the neutral position and is unstable. However, it can be demonstrated that a 2-segment under-

actuated inverted pendulum is controllable and can be stabilized (Figure 2.2). Humans achieve this through voluntary and reflexive neuromuscular control. Stability tests are typically conducted at or below the 100% level, thus requiring neuromuscular control to maintain stability. Testing at prescribed levels of instability (e.g. 100%∇G, 75%∇G, 50%∇G) can be achieved by adjusting the spring location to compensating for anatomical differences in test subjects.

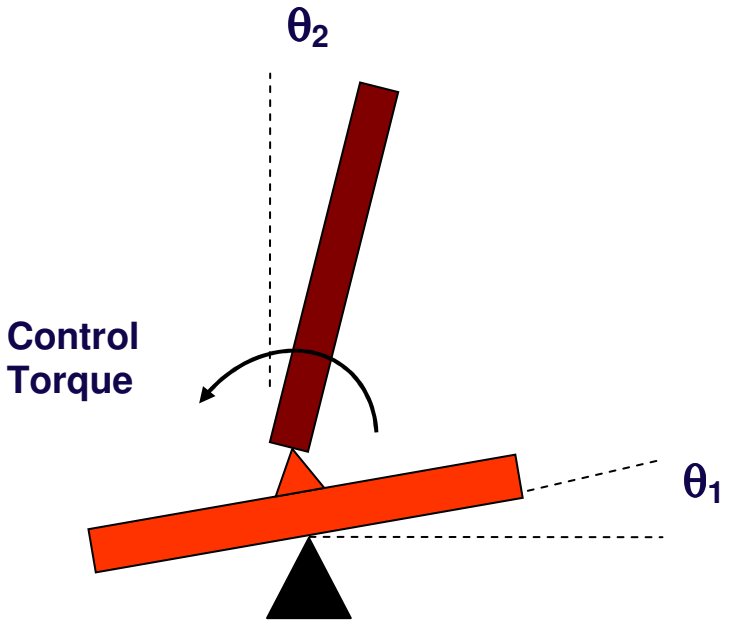

Figure 2.2: Two segment inverted pendulum model.

2.2.2 Experimental Protocol

Twelve human subjects with no history of low back pain participated in the study. Prior to participation all subjects were informed of the nature of the study and signed an informed consent form approved by the institutional review board at Virginia Tech. Before stability testing was performed, the gravitational gradient for each subject was obtained. The spring distances needed to achieve 100%, 75%, and 50% of the subject's gravitational gradient was calculated. During experimental stability measurements, the subjects were instructed to sit on

the wobble chair with their arms crossed over the chest and attempt to maintain an upright posture for 60 seconds. Seat angles and torso angles were recorded at 100 Hz in two dimensions with 6 degrees of freedom electromagnetic sensors (Motion Star Systems, Ascension Technology Corp, Burlington, VT). The subject was able to use small dynamic movements of the torso to keep the seat at a level position. Each subject was tested at all three spring settings. The order of the spring setting was randomized to avoid confounding between difficulty and trial order. Subjects performed five practice trials prior to executing five replications at each setting.

2.2.3 Lyapunov Stability Analyses

The maximum Lyapunov exponent is a measure of local stability. Large exponents indicate rapid divergence of two points that are initially close in state space (Figure 2.3). By calculating the maximum Lyapunov exponent from data that is averaged over the entire time series, the global stability of the system is estimated. The maximum Lyapunov exponent, λ_{max}, quantifies the exponential rate that two points diverge in state space.

$$d(\Delta t) = d(0)e^{\lambda_{\max}\Delta t} \qquad (2.3)$$

where d(0) is the initial Euclidean distance in state space between two points in the time series. The evolution time, Δt, is the amount of time that has elapsed as the trajectories of the two points are tracked forward in time. The Euclidean distance between the two points at an evolution time, Δt, is given by $d(\Delta t)$. This analysis method is outlined below.

Measured data consisted of a continuous series of data points representing the trajectory over the 60 second trial. From the measured data a time dependent state vector was generated using post-processing software (Matlab, Natick, MA).

$$q(t) = \left[\theta_{AP\_S}(t) \quad \theta_{ML\_S}(t) \quad \dot{\theta}_{AP\_S}(t) \quad \dot{\theta}_{ML\_S}(t)\right] \tag{2.4}$$

The state vector was filtered at 8 Hz with a seventh order low pass Butterworth filter and down-sampled to 25 Hz prior to analysis. Initially, the first data point in the time series, q(0), was identified as the reference point. A data point was identified that was close to the reference point in state space, but not in time. The nearest neighbor was identified as the point with the smallest Euclidean distance from the reference point in state space. Measures were taken to ensure that each nearest neighbor was not highly correlated with the reference point or with any previously found nearest neighbors. Specifically, the location of the first peak in the autocorrelation function was determined, and this temporal range was avoided in the selection of the nearest neighbor. Several investigators have tracked the divergence of a nearest neighbor to find the maximum Lyapunov exponent (Wolf et al. 1985; Rosenstein et al. 1993a; England and Granata 2006; Granata and England 2006). In this study the three nearest neighbors were analyzed in order to reduce variability of the results. The above process was repeated with each point in the time series being considered the reference point. The distance between the reference point and each nearest neighbor was calculated as both points evolved over time (Figure 2.3). The expansion was defined as the relative increase in distance between the two points for some Δt. The mean expansion for a given evolution time was determined by averaging the expansion over all reference points and all nearest neighbors.

$$Mean\ \ Expansion\ \ (\Delta t) = \frac{1}{3n}\sum_{i}^{n}\sum_{j}^{3}\frac{d(\Delta t)_{ij}}{d(0)_{ij}} \tag{2.5}$$

Where, n is the number of points in the time series indexed by i, and j is the index of the nearest neighbor.

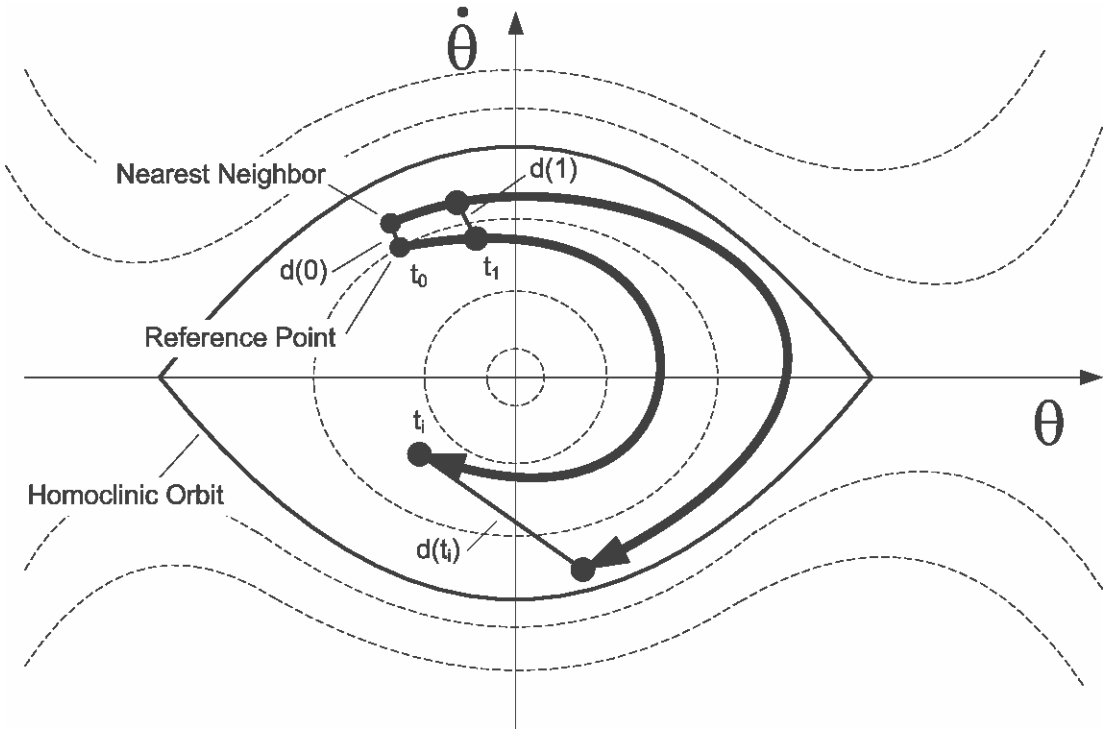

Figure 2.3: Nearest neighbor to the reference point was found in n-dimensional state space. The distance between these two points is tracked as it evolves over time. The heteroclinic orbit indicates the separatrix between stable and unstable regions.

The maximum Lyapunov exponent can be calculated by solving equation [2.3].

$$\lambda_{\max} = \frac{1}{\Delta t}\ln\left(Mean\ Expansion\ (\Delta t)\right) \tag{2.6}$$

From the experimental data, the maximum Lyapunov exponent was found by calculating the slope of the natural log of the mean expansion with respect to the evolution time over the range of 0.2 seconds to 0.7 seconds (Figure 2.4). Evolution times less than 0.2 seconds were excluded from the evaluation because the 8 Hz filter (T =.125 s) removed much of the data in this range. After 0.7 seconds, the curve began to flatten as the points approached full diffusion within state space. λ_{max} was calculated for each subject, trial, and week using custom Labview code (National Instruments, Austin, Texas).

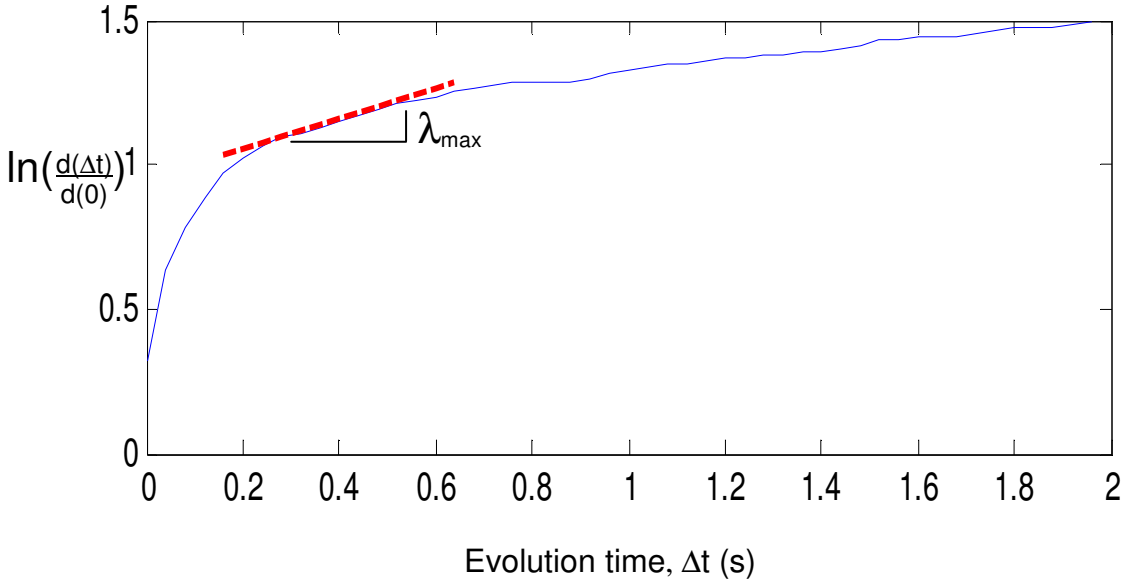

Figure 2.4: The maximum Lyapunov exponent was determined by calculating the slope of the mean expansion as a function of the evolution time.

2.2.4 Statistical Analysis

Twelve subjects were each tested five times at each spring setting. The maximum Lyapunov exponents calculated for each of the five replicate trials was averaged to obtain a value for that subject under that condition effectively reducing the data to the experimental unit (Sall and Lehman 1996). Repeated measures ANOVA was used to determine the effects of spring setting, week of test, and their interaction. This was done using JPM ® 7.0 (SAS Institute Inc., Cary, NC), with a criterion of p=0.05 used to conclude significance.

2.3 Results

The statistical results are shown below (Table 2.1 & 2.2 and Figure 2.5). Spring setting was found to be negatively correlated with λ_{max} (Figure 2.5a). Furthermore, post-hoc analysis using Tukey HSD test showed significant differences between all spring levels (Table 2.3). No significant difference was found in λ_{max} between weeks (Figure 2.5b) or the interaction between spring and week (Figure 2.5c).

Table 2.1: Main Effects Table

Level	Least Sq Mean	Std Error	Mean
week 0	0.68	0.024	0.53
week 1	0.66	0.024	0.49
Spring 50% ∇G	0.68	0.024	0.67
Spring 75% ∇G	0.54	0.024	0.50
Spring 100% ∇G	0.39	0.024	0.36

Table 2.2: ANOVA Table

Source	DF	Sum of Squares	Mean Square	F Ratio	Pr ob > F
Model	16	1.53	0.096	14.0	<.0001*
Subject (Random)	11	0.32	0.029	4.3	0.0001*
Spring	2	0.49	0.249	85.0	<.0001*
week	1	0.0009	0.0009	6.1	0.7166
Spring*week	2	0.012	0.006	0.91	0.41
Error	55	0.38	0.007		
C. Total	71	1.91			

Table 2.3: Tukey HSD test results

Level			Least Sq Mean
50	A		0.68
75		B	0.54
100		C	0.39

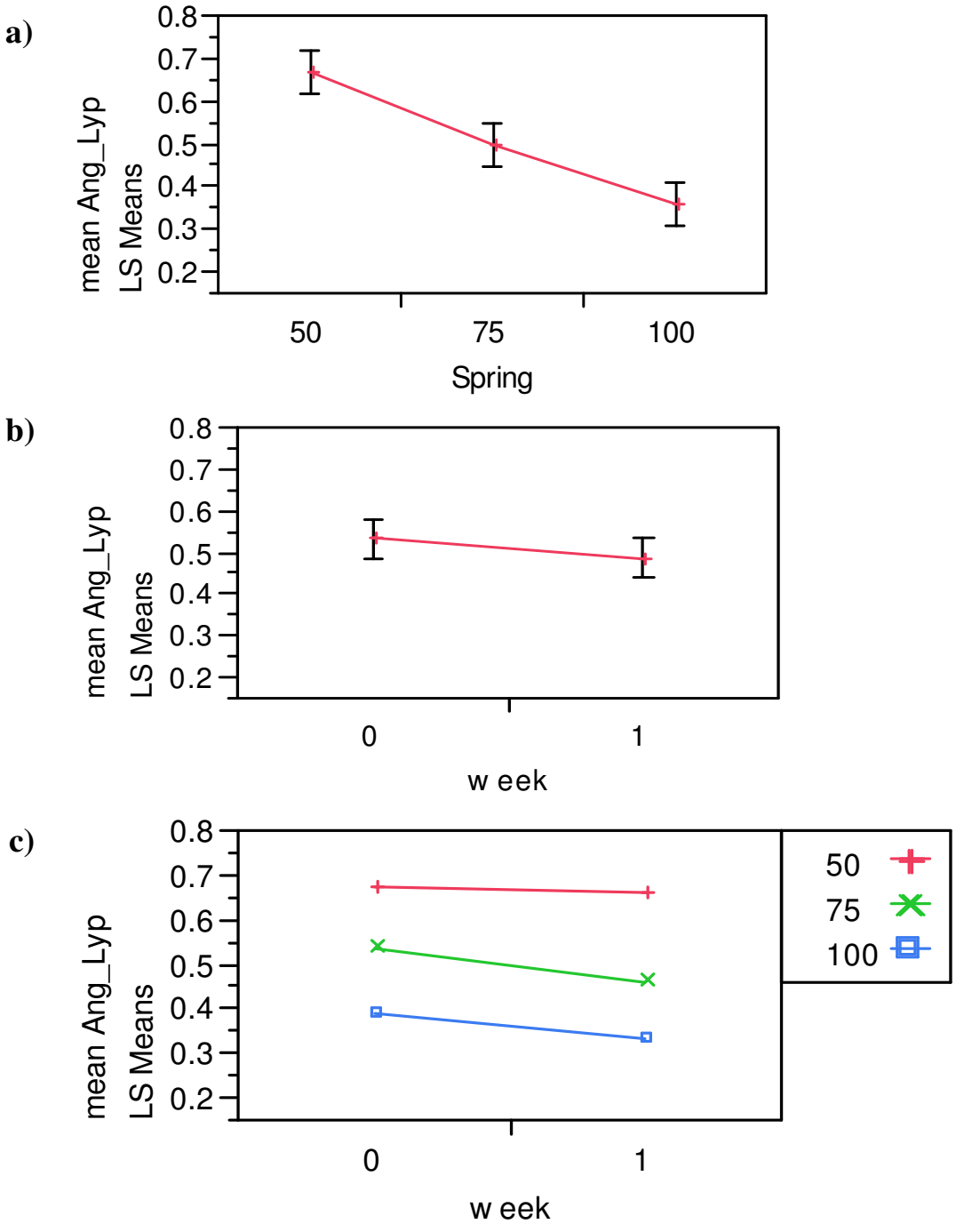

Figure 2.5: The main effect of a) spring setting and b) week of testing is shown. In addition, the interaction c) between spring and week is presented.

2.4 Discussion

The negative correlation between the maximum Lyapunov exponent and chair stability was expected. Higher mean divergence rates associated with large values of λ_{max} should occur at the more difficult spring settings. This is because the potential function is shallower with smaller gradients. Thus, random perturbations inherent in the system lead to larger motions and higher divergence rates. The mean value for the maximum Lyapunov exponent was positive which indicates divergent behavior in at least one dimension of state space. However, since stability of the overall system was maintained during the test, the sum of all Lyapunov exponents (i.e. the Lyapunov spectrum) must be less than or equal to zero.

One limitation of this study was that all stability tests were conducted with fully active neuromuscular control. Since no tests were conducted with disabled or altered control, one cannot separate the contribution of the compensatory neuromuscular control from the uncontrolled dynamics. Thus, it cannot be determined if the compensatory neuromuscular control changes as a function of the task difficulty.

Insignificant differences between the two duplicate test sessions indicate that the method has good repeatability with relatively small data sets. Test repeatability enables experiments to be conducted that measure changes in stability resulting from varying conditions such as fatigue, flexion relaxation, or physical therapy.

2.5 Summary and Conclusions

The wobble chair apparatus allows for empirical measurement of torso dynamic stability over a continuously adjustable range of static stability and instability. Adjustments can be made to compensate for anatomical differences in subjects allowing tests to be conducted at a specified

static stability level. A method for conducting Lyapunov stability analysis on the experimental data was developed that tracked the divergence of nearest neighbors for all points in the time series. The results showed a significant negative correlation between chair stability and generally consistent results from week to week. This method was found to be sensitive to changes in stability and indicates that it may be a useful method to analyze the differences in stability resulting from changing parameters.

2.6 Acknowledgements

The research was supported by grant R01 OH 008504 from NIOSH of the Center for Diseases Control. The author would also like to acknowledge the efforts of Greg Slota and Hyun Wook Lee in building the apparatus and collecting data presented in this chapter.

Chapter 3

Evaluation of the Threshold of Stability; A Pilot Study

3.1 Abstract

Current methods to study torso stability assess kinematic variability or local dynamic stability. In this chapter, a new stability metric is introduced, the threshold of stability. The threshold of stability differs from existing methods because it evaluates the boundary between stability and instability rather than evaluating dynamics within the stable region of state space. In this section, a pilot study was performed using this new method and compared to results found for the maximum Lyapunov exponent. Participants were tested using an existing apparatus that challenges spinal stability (the wobble chair), with eyes both open and shut. Results showed significant differences in stability between these two conditions using this method. The sensitivity of this method indicates that it may be a useful metric in larger studies for the evaluation of torso stability in low back pain patients. In addition, this new method has an additional advantage over previous methods in that no electronics are needed to perform an evaluation. Its simplicity, sensitivity, and low cost may make it suitable for evaluating low back pain patients in a clinical setting.

3.2 Introduction

Researchers and clinicians continue to search for a reliable indicator of low back pain (LBP). Mainly researchers have studied torso stability in association with LBP (Bergmark 1989; Granata and Orishimo 2001; McGill 2001; Van Dieen et al. 2003; Brown and McGill 2005; Reeves et al. 2007b). Some methods which have been used to quantify torso stability include kinematic variability parameters borrowed from techniques used to measure standing postural sway (Granata and Lee 2008). In addition, dynamic stability methods such as stability diffusion analysis (Cholewicki et al. 2000) and the calculation of Lyapunov exponents (Tanaka and Granata 2007; Granata and Lee 2008) have also been applied. All of these methods have at least one characteristic in common. They each assess stability by evaluating the motion within the stable region of state space. This may not be a good assessment tool since high variability within the stable region does not always correlate with instability. Furthermore, low variability within the stable region does not indicate high robustness to perturbations. Since low back injury has been associated with a loss of stability, it may be more important to determine at what point stability is lost, i.e. when the trajectories leave the stable region of state space. A new metric, the threshold of stability, was created to quantify this value. Threshold of stability is defined as the maximum task difficulty in which stability can be maintained for a given period of time.

A new metric, the threshold of stability, was developed for torso stability using an unstable sitting apparatus called the wobble chair. The wobble chair (Figure 2.1 & 3.1) has movable springs that can be adjusted in order to change the amount of restorative torque applied to the seat (Tanaka and Granata 2007). Increasing task difficulty is attained by moving the stabilizing springs closer to the central ball joint, thus reducing the stabilizing moment provided by the springs. In this study, a participant's balance control system is challenged to determine

the maximum task difficulty in which stability can still be maintained. The presence or absence of visual feedback (i.e. eyes open or shut) was the condition used in this pilot study to determine the sensitivity of the method.

Figure 3.1: Participant balances on the wobble chair moving the lumbar region of her torso to maintain stability.

This study was not focused on understanding the effects of visual feedback on balance control. Instead, visual feedback was used to test the sensitivity of the method. There were two main reasons for selecting visual feedback as the controlled parameter. First, a within-subjects test could be performed eliminating the variability from subject to subject and allowing a smaller number of participants to be tested. Second, a real difference should exist in the balance capability of a participant when compared with and without visual feedback. Moreover, it was expected that difference would be large making it more likely to be detected using the new method. Since this was the first study to evaluate this new metric, it was important to apply the method to a condition that was likely to have a real and significant difference. Therefore, if no difference was found, it could be concluded that the method was insensitive to this difference. If a test condition were evaluated with an unknown outcome, it would not be clear if a negative result was due to no difference in the controlled parameter or insensitivity of the method.

The threshed of stability is a new type of parameter. To the author's knowledge, this is the first study to determine the boundary of torso stability. All previous evaluations of torso stability have examined the level of local instability for overall globally stable systems.

3.2 Methods

3.2.1 Subjects

Eight adults participated in the study, and were asymptomatic for LBP at the time of testing. Of the participants, five were male and three were female. Mean (SD) body mass was 157(29) kg, stature was 174(15) cm and age was 27(5) years. In addition, participants had no

previous history of spinal surgery, sciatica, herniated or ruptured discs, or fractured vertebrae. Prior to beginning the tests, all participants were informed of the nature of the study and signed an informed consent form approved by the institutional review board at Virginia Tech.

3.2.2 Set-up

Before stability testing was performed, the gravitational gradient (∇G) for each subject was found using the methods described in chapter 2. With this information, the spring distances associated with levels of ∇G on 5% increments were calculated. Sensors capable of tracking angles in three-dimensional coordinates (MTx, Xsens Technologies; Enschede, The Netherlands) were attached to the base of the seat and to the back of the participant at approximately the level of the fifth thoracic vertebrae (T-5). These sensors were used to track movements of the wobble chair and trunk during the experiment.

Although full medial-lateral and anterior-posterior motion is possible using the wobble chair, the focus of this study was on sagittal plane (antero-posterior) movement. This restriction was implemented so that the experimental results calculated in chapter 6 could be better compared to the planer wobble chair simulations developed in chapter 5. Medial lateral (ML) motion was not restricted in the study. Instead, restorative spring force was set to 100% ∇G in the ML direction so stability in these directions was easy to achieve (Figure 3.2). Starting with a spring setting of 80% ∇G in the anterior and posterior directions, spring distance was decreased during the study focusing movement in the sagittal plane.

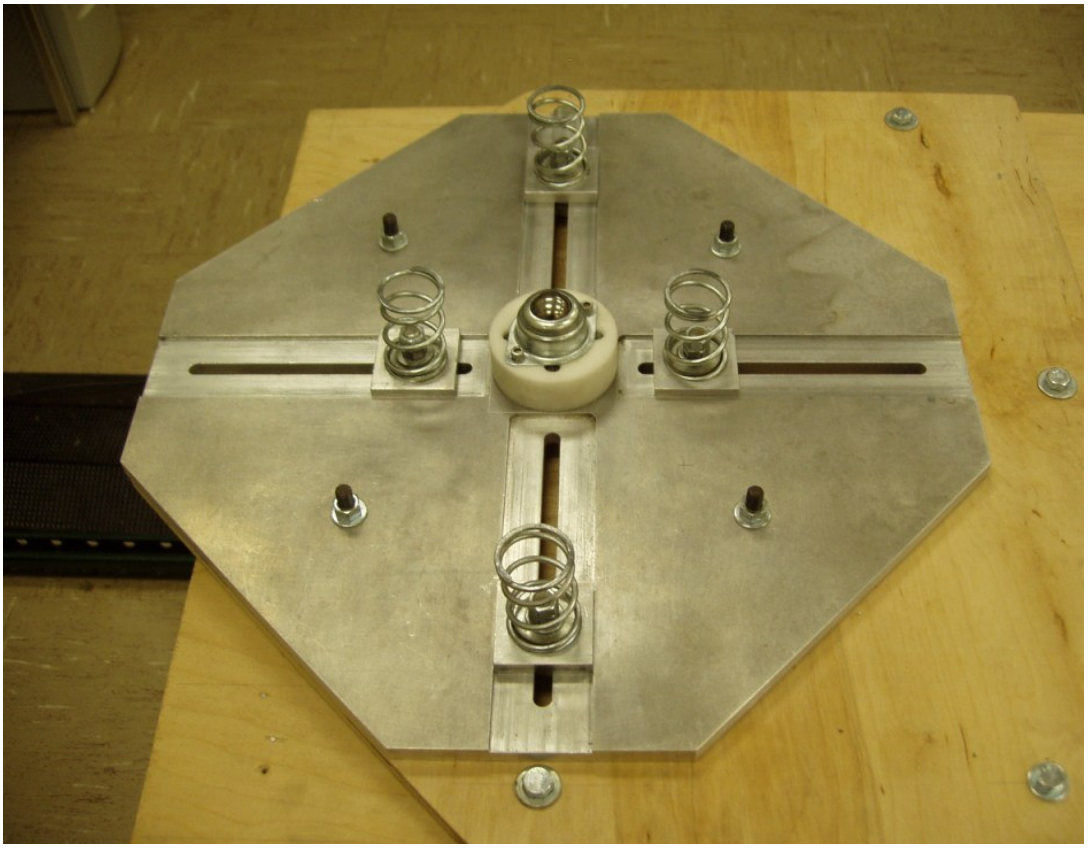

Figure 3.2: The wobble chair has four stabilizing springs that can be set to different distances to control the amount of restorative torque applied to the participant.

3.2.3 Experimental Protocol

Participants were instructed to sit on the wobble chair with arms crossed in front of the body and to attempt to maintain an upright posture. The data collection software, a custom Labview (National Instruments, Austin Texas) program, was executed. This program initialized the position sensor angles establishing a zero degree reference and began the angle recording process at 100 Hz. After a few seconds, stop blocks were removed destabilizing the wobble chair. The official start of the trial began 20 seconds into data collection following sensor initialization, block removal, and initial stabilization by the participant. Small dynamic

movements of the torso were used to maintain balance over the central ball joint. The participant was monitored for 60 seconds to determine if contact was made with the base of the seat indicating instability. Upon completion of the trial, stabilizing blocks were reinserted, and the participant was allowed to rest for at least one minute between trials to avoid mental and physical fatigue.

During the practice phase, spring distance was adjusted following each trial to determine the smallest spring distance at which the participant was able to maintain balance for the duration of the test without becoming unstable. This initial phase of the test served two purposes. It allowed the participant to practice balancing on the wobble chair to reduce learning effects, and it also helped the experimenter to find the approximate value of the threshold of stability. Beginning with this initial spring distance, trials were performed to locate the critical spring distance, i.e. the threshold of stability.

Participants were randomly selected to be tested first with eyes open or shut using a coin toss. After 50% of the people had been tested with eyes shut first, the remaining people were tested with eyes open first in order to make the overall numbers equal for testing order. For participants who were tested with eyes open first, the practice trials were performed with eyes open. For participants who were tested with eyes shut first, the first practice trial was performed with eyes open and the remaining trials were performed with eyes shut. Following each trial, the following rules were applied to determine the next spring setting used. If the participant did not become unstable and generally stayed within four degrees of the center ($\theta_1 = \theta_2 = 0$) as observed on a biofeedback device, the next spring setting would be reduced by 20% ∇G. If the participant did not become unstable and generally stayed within seven degrees of the center, the next spring setting would be reduced by 10% ∇G. If the participant became unstable and contacted the base,

the next spring setting would be increased by 5% ∇G. Subsequent adjustments were in 5% ∇G increments based on the outcome of the trial. Passing trials (i.e. contact was not made with the base) resulted in a decrease in spring setting for the next trial. Conversely, springs setting were increased following failing trials.

Tests with either eyes shut or open were performed following the practice trials. Eight trials were conducted using the spring adjustment procedure defined above to determine the threshold of stability for this condition. If the threshold of stability could not be determined in eight trials using the method described in the next section, additional trials were performed until a definitive result was obtained.

Preliminary investigations showed the difference in threshold of stability between eyes open and shut was approximately 20% ∇G. If eyes open was tested first, the initial spring setting for the eyes shut test was chosen to be 20% ∇G larger than the threshold of stability found for the eyes open test. Although the actual value of the threshold of stability was found through testing, this initial adjustment was effective at reducing the number of trials needed to obtain a definitive result. Conversely, if the eyes shut condition was tested first, the initial spring setting for the eyes open test was chosen to be 20% ∇G smaller than the threshold of stability found for the eyes shut test. Like the first test condition evaluated, a minimum of eight trials was performed to definitively determine the threshold of stability for the second test condition.

3.2.4 Analytical and Statistical Methods

The value for the threshold of stability was determined through examination of the test result at each spring setting (Figure 3.3). The number of passing and failing trials at each spring setting was tallied. When both passing and failing trials existed at a given spring setting, the

majority result was assigned to that spring setting. If upon completing eight trials a definitive line could be drawn separating passing and failing spring settings, testing at this level was considered complete. However, if the number of passing and failing trials was equal at a given level, additional trials were performed until a definitive outcome was obtained.

A t-test was performed to determine if differences in the threshold of stability were detected between the "with" and "without" visual feedback test conditions. A value of $\alpha = 0.5$ was used as the criterion for significance.

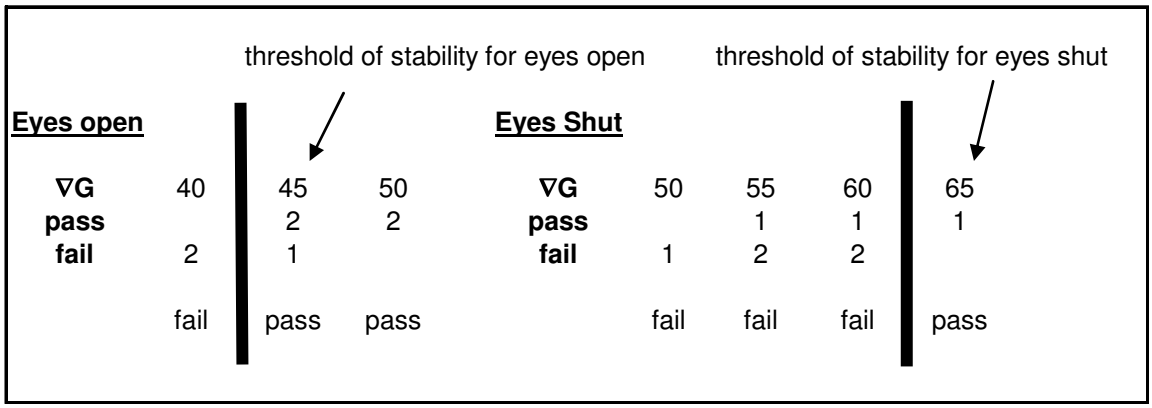

Figure 3.3: The threshold of stability was found by locating the lowest passing spring setting. In this case 45% ∇G for eyes open and 65% ∇G for eyes shut.

In addition, Lyapunov stability analysis was performed on the first passing trial at the threshold of stability for each test condition. The methods described in chapter 2 were applied to determine the time series averaged finite time Lyapunov exponent. Differences between the two test conditions for the Lyapunov exponent were also evaluated using a t-test.

3.3 Results

The time series shown in Figure 3.4 is typical of those collected. The angle of the lower body, θ_1, shows large variability. The upper body angle, θ_2, remains relatively constant. In some trials an initial adjustment was made during the beginning of the trial after which relatively

steady results were maintained. These differences are also visible when viewing θ_1 versus θ_2 (Figure 3.5).

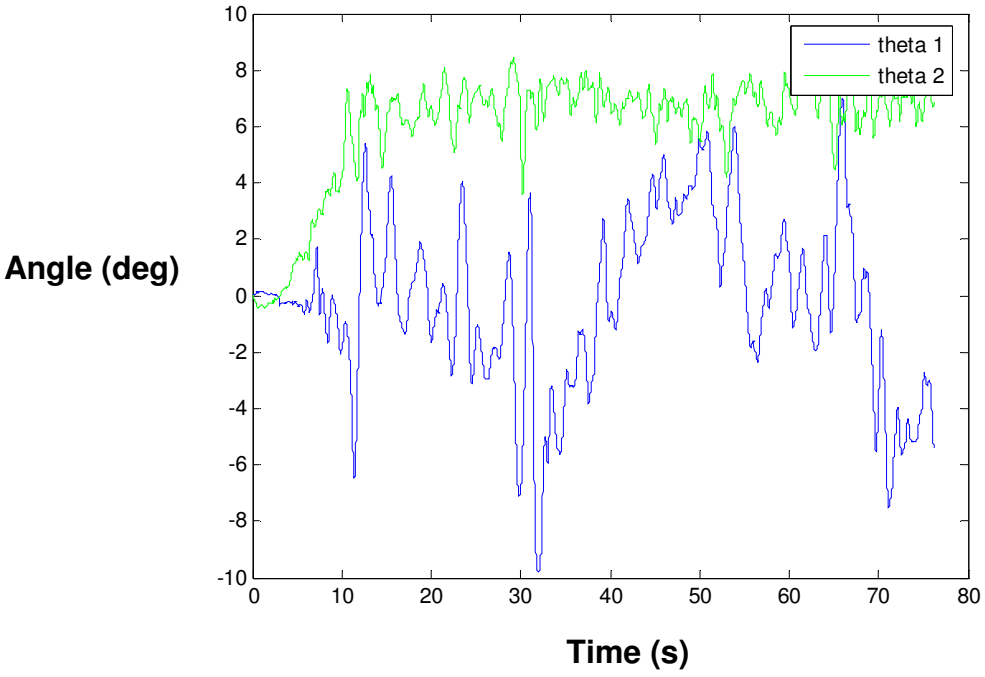

Figure 3.4: The lower body angle (blue) shows large variability and the upper body (green) variability is smaller.

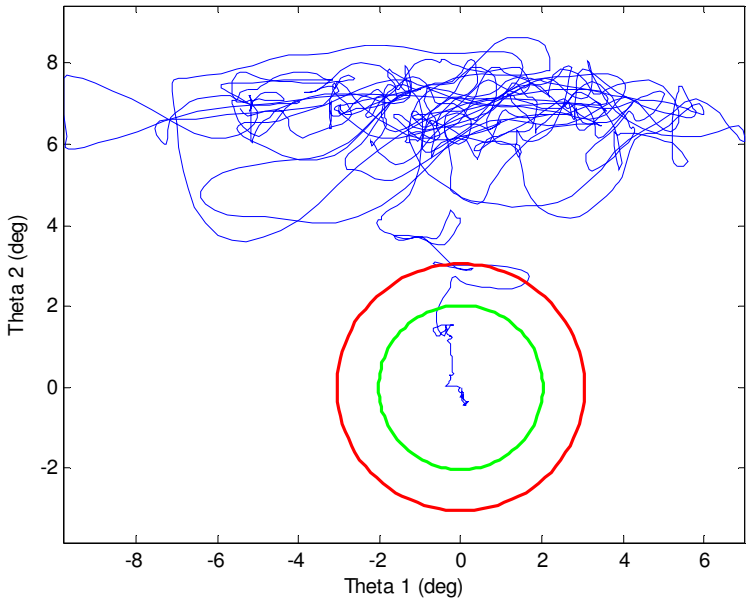

Figure 3.5: After an initial adjustment at the beginning of the trial, the upper body angle, θ_1, generally stabilized and motion was dominated by the lower body, θ_1. An RMS value of 3.0 degrees (red circle) was found for the θ_1 direction. In the θ_2 direction, the RSM value was 2.0 degrees.

The threshold of stability and maximum Lyapunov exponent were found for each participant under each condition of visual feedback (Table 3.1). For the threshold of stability, the mean value for eyes open and shut were 36 (6.4) and 51 (7.4) %∇G, respectively, difference of ~15% that was significant (t = 11.2; p = .0001). For the maximum Lyapunov exponent, the respective values for eyes open and shut were 0.40 (0.18) and 0.47 (0.20), though this difference was not be significant (t = 0.786; p = 0.46).

Table 3.1: Results of threshold of stability experiment

Participant	Eyes Open		Eyes Shut	
	Threshold of Stability	Maximum Lyapunov Exponent	Threshold of Stability	Maximum Lyapunov Exponent
1	35%	0.42	50%	0.52
2	45%	0.55	65%	0.43
3	35%	0.37	50%	0.44
4	45%	0.10	55%	0.65
5	30%	0.45	45%	0.52
6	40%	0.72	55%	0.74
7	30%	0.29	40%	0.11
8	30%	0.33	50%	0.31

3.4 Discussion

Significant differences in the threshold of stability were found between the two groups showing this method to be sensitive to differences in these two conditions. The maximum Lyapunov exponent did not show a significant difference. This may be due to the small number of trials in this pilot study. In addition, the maximum Lyapunov exponent was evaluated at different stability levels. This test would be more likely to show a difference in the Lyapunov exponent if the eyes open and eyes closed condition were tested at the same spring setting.

Preliminary data suggested that the amount of effort applied during the stability test was lower for easier tasks (Granata et al. 2006). As a result, peak performance of the neuromuscular control system may not have been applied during easier tasks in order to expend less energy. This may explain why the maximum Lyapunov exponent found during preliminary studies was not dramatically higher despite a much higher level of task difficulty. However, since maximal effort was required at each individual's limit of stability, this may be a more sensitive means of differentiating the performance capability of the individual's neuromuscular control system. The threshold of stability identifies a state where the kinematic variability due to system noise has grown to a value that it is just within the basin of stability for the individual (see Chapter 4). Any further increases in system perturbations or task difficulty will result in unstable behavior.

3.5 Summary and Conclusions

A pilot study was performed to evaluate the sensitivity of a new metric to detect differences in torso stability. This new metric, the threshold of stability, differs from other metrics in that it is associated with the boundary between stable and unstable regions of state space. Results found using this method showed significant differences in stability between these two conditions. The sensitivity of this method indicates that it may be a useful metric in larger studies for the evaluation of torso stability in low back pain patients.

This method may find application in a clinical setting. Although electronics were used in this study, the time series angle data collected were intended for evaluation in chapter 6 and were not needed to find the threshold of stability. Furthermore, although a force plate was used to find ∇G for each participant, a rough approximation of ∇G could also be obtained using

anthropometric parameters measured in the clinician's office. This would eliminate the need to purchase and maintain an expensive force plate. Its simplicity, sensitivity, and low cost may make it suitable for evaluating low back pain patients in a clinical practice. If desired, these initial results could then be confirmed in a fully instrumented biomechanics laboratory. Finally, the concept presented herein may be extended to evaluate other systems in which a threshold could be found separating two distinctly different outcomes.

Chapter 4

Locating Separatrices and Basins of Stability in a Reduced Order Model

4.1 Abstract

An approach is presented for identifying separatrices in state space generated from noisy time series data sets representative of those generated from experiments. This approach demonstrates how Lagrangian coherent structures (LCS), ridges in the state space distribution of finite-time Lyapunov exponents, can be used to locate these separatrices. This method can be performed using a single trajectory that evolves over time opposed to previous approaches which required an entire vector field at each instance in time. The method is applied to a biological simulation in which the separatrix reveals a basin of stability. The results of the nonlinear analysis show that the LCS calculated from only trajectory data aligns well with the LCS found using the traditional vector field analysis methods. In general, it is believed this method provides a fruitful approach for extracting information from noisy experimental data with regards to boundaries between qualitatively different kinds of motion.

4.2 Introduction

Increasingly, dynamical systems of interest are defined not by analytical models but by data from experiments or large-scale simulations. Some examples already exist in the areas of musculoskeletal biomechanics (Dingwell and Cusumano 2000; Akay 2006; England and Granata 2007) and geophysical fluid dynamics (Pierrehumbert 1991b; Pierrehumbert 1991a; Haynes 2005; Shadden et al. 2005).

In many cases, researchers want to ascertain if deterministic chaos is present (Akay 2006; Falconer et al. 2007). This can be achieved by determining characteristic exponents that describe the sensitivity of the solution to initially close-starting conditions. One popular technique is to estimate the (maximum) Lyapunov exponent averaged over the sampled portion of state space (Benettin et al. 1980a; Benettin et al. 1980b; Wolf et al. 1985; Eckmann et al. 1986; Rosenstein et al. 1993b; Kantz and Schreiber 2004). This method is well suited for analysis of time series data from experiments.

Higher values of the Lyapunov exponent indicate greater divergence rates in state space. When comparing the Lyapunov exponent found for two different experiments, a researcher may conclude that one system is more stable than another. However, this conclusion may not necessarily be true. If the trajectories of both systems remain within the same compact region of state space, then both systems can be considered stable over the finite time evaluated regardless of the value of the Lyapunov exponent. In order for the system to become unstable, according to Lyapunov, the system trajectory must cross the boundary separating the stable and unstable regions of state space.

The locations of these boundaries can be found by extracting additional information contained within the time series data. Rather than averaging the Lyapunov exponents over state space to obtain a single scalar value as traditionally done, one can generate a maximum Lyapunov exponent field. This field quantifies the expansion rate at different locations in state space. This state space perspective can lead to a better understanding of the system's behavior through identification of trajectory boundaries. In order to find these boundaries, techniques are borrowed that were developed for the analysis of fluid flows (Haller 2000; Haller and Yuan 2000; Haller 2001a; Haller 2001b; Haller 2002; Shadden et al. 2005). Lagrangian coherent structures (LCS) (Haller and Yuan 2000) are state space boundaries which are defined as the ridges of the finite-time Lyapunov exponent (FTLE) field (Shadden et al. 2005). These structures indicate the location of the separatrix demarking the boundary between qualitatively different kinds of motion. In general, LCS are time dependent and found by generating a FTLE field from the vector field of the system. However, vector fields are usually unavailable in biomechanics experiments where often only a small number of state variables are measured over time.

In this chapter, LCS theory is applied to a rigid body biodynamics problem to identify state space boundaries that are assumed to be time independent. It is shown that the LCS can be generated from individual trajectories obtained from time series data without the need of a full vector field at each instant in time. LCS have previously been shown to be robust with respect to noise (Haller 2001a; Haller 2002) making them attractive for use in experimental data analysis where noise sensitivity is an important issue (Casdagli et al. 1991; Ellner and Turchin 1995; Franca and Savi 2001).

4.2.1 Applications of LCS to Biomechanics

LCS have previously been used to analyze dynamical systems defined by fluid flow fields from data (Franca and Savi 2001; Haller 2002; Wang et al. 2003), analytical biochemical models (Aldridge et al. 2006), and low degree of freedom mechanical systems(El Rifai et al. 2007). Based on current knowledge, the work presented herein is the first application of LCS to time series data with the absence of a vector field. Data in this form is commonly generated in biomechanical experiments. The biodynamics problem analyzed in this paper may be categorized into a class of biomechanics problems that contain separatrices. There exists a variety of potential applications for these methods in which two or more qualitatively different types of movement exist. A few examples are illustrated below.

In biomechanics, a separatrix or recovery envelope exists between standing and falling. Standing with postural sway is a distinctly different type of motion than falling. During standing, the body remains in the vicinity of an equilibrium position and may be characterized as dynamically stable over a suitable finite-time horizon. Compare this motion to falling where the body rapidly diverges from the vicinity of the equilibrium position at an increasing velocity. In falling, the body behaves unstably with respect to the upright vertical position. If one allows an experimental subject to take a step during fall recovery, another boundary will develop. Now three states exist, standing, recovering from a fall with one step, and falling. Each type of motion is divided from the other by a separatrix. Extending this theory, a state space diagram with multiple fronts may be generated.

Previous studies have investigated the range of forward and backwards lean that can be attained while maintaining an upright posture without stepping (Kuo and Zajac 1993; Winter et al. 2001; Morasso and Sanguineti 2002). These studies considered the system to be quasi-static

where stability is controlled by muscle strength, base of support and the location of the center of mass. By analyzing the results of these studies, a stable region may be defined in one state space dimension (position) based on the above parameters. Pai et al. expanded this work to two dimensions by including velocity in his mathematical models (Pai and Patton 1997; Iqbal and Pai 2000). Pai used vector fields defined by the system's differential equations to determine regions of stability for balance recovery. Although this work expanded the evaluation of stability into state space, only a small portion of state space was evaluated, and errors in the governing equations resulted in criticism (Edwards 2001).

A comparable problem to standing postural sway is the challenge of maintaining torso stability. In this case, a separatrix exists delineating stable torso sway from unstable and potentially injurious motion. In our laboratory, torso stability is studied using an experimental apparatus known as the wobble chair. Torso stability is necessary to avoid large deformations in the lumbar spine which is often associated with low back injury and pain (Cholewicki and McGill 1996; Granata and Orishimo 2001). In this study, the separatrix is extracted from a reduced order model which captures the essential features of the experimental data.

The computation of finite-time Lyapunov exponents from experimental data has been used before in musculoskeletal biomechanics. In particular, it has been used to quantify local dynamic stability during locomotion (Dingwell and Cusumano 2000). However, separatrices between dynamically stable walking/running could also be evaluated using the methods developed in this paper.

4.2.2 Sensitivity analysis and finite-time Lyapunov exponents

In this section, we briefly review some mathematical preliminaries regarding stability or sensitivity of trajectories. Suppose we are given a reference trajectory x(t) going from x_0 at time t_0 to x_1 at time t_1. We assume the trajectory evolves under the dynamical equations of a time-independent (autonomous) system

$$\dot{x} = f(x) \quad x \in R^n \tag{4.1}$$

This equation describes a flow field or vector field. The sensitivity of the reference trajectory is discussed below.

Let the trajectories of the system (4.1) with $x(t_0) = x_0$ be denoted by $\phi(t,t_0)$.

In other words, $\phi(t,t_0) : x(t_0) \rightarrow x(t)$ denotes the flow map of the dynamical system (4.1) when mapping particles from their initial location at time t_0 to their location at time t. For our purposes, the flow map will be denoted as $\phi(t,t_0; x_0)$ or simply $\phi(t; x_0)$ so the dependence on the initial condition $x(t_0) = x_0$ is made clear.

Consider a second trajectory that starts slightly away from the reference trajectory x(t), i.e., starts from the perturbed initial vector $x_0+\delta x_0$ at time t_0. As the trajectories evolve, the vector displacement (or perturbation vector)

$$\delta x(t) = \phi(t; x_0 + \delta x_0) - \phi(t; x_0) \tag{4.2}$$

will also evolve. For our purposes, the "second trajectory" might be the result of another experimental trial or another portion of the same trajectory separated by a sufficient amount of time to avoid a substantial autocorrelation. This is discussed further below.

The linear relationship between small initial perturbations and perturbations at some time t is

$$\delta x(t) = \Phi(t, t_0)\delta x_0 \tag{4.3}$$

where

$$\Phi(t, t_0) = \frac{\partial \phi(t; x_0)}{\partial x_0} \tag{4.4}$$

is the state transition matrix (also known as the fundamental matrix). The state transition matrix can be viewed as a deformation gradient. If an (infinitesimal) n-dimensional spherical blob of particles is placed about the reference trajectory, then after a duration $T = t\text{-}t_0$, the blob will have expanded in some directions and compressed in others to form an n-dimensional ellipsoid (Figure 4.1).

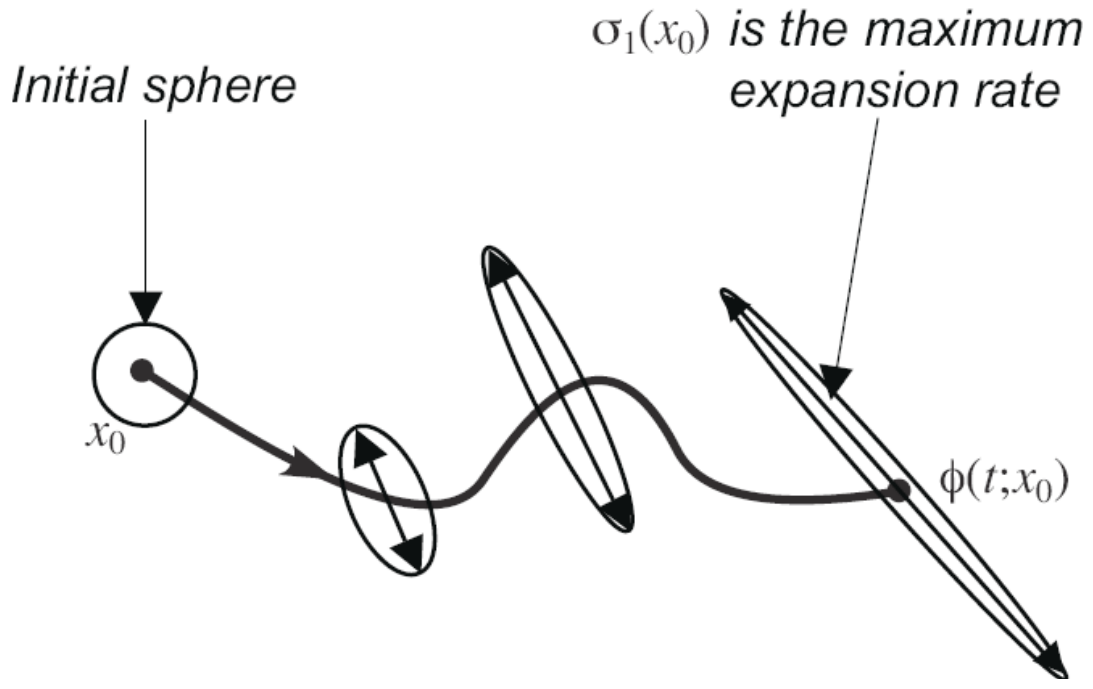

Figure 4.1: The state transition matrix is a deformation gradient about the reference trajectory describing how an initially spherical blob of surrounding particles deforms into an ellipsoid.

The matrix $\Phi(t,t_0)$ contains information about this expansion and contraction as well as the rotation of the initial blob of particles due to the locally deforming nature of the flow.

Suppose there exists a state transition matrix over some interval, $\Phi(t,t_0)$. The size of the final perturbation at time t is given by

$$\left\|\delta x(t)\right\|^2 = \delta x_0^T [\Phi(t;t_0)^T \Phi(t;t_0)] \delta x_0 \qquad (4.5)$$

where $\|\cdot\|$ is the vector norm on $\mathbb{R}^n$, A^T denotes the transpose of the matrix A, and the perturbations are considered as column vectors. The symmetric matrix

$$C = \Phi(t;t_0)^T \Phi(t;t_0) \qquad (4.6)$$

is the finite-time right Cauchy-Green deformation tensor (Shadden et al. 2005). The matrix C is a rotation-independent measure of deformation; it gives the square of the local change in distances due to deformation (Fung 1993; Truesdell and Noll 2004).

Since C is a symmetric, positive definite matrix, it has n real, positive eigenvalues (Strang 1998; Lekien et al. 2007).

One can associate with point x_0 a maximum finite-time Lyapunov exponent, given by

$$\sigma_1(x_0) = \frac{1}{T} \ln \sqrt{\lambda_{\max}(C)}, \qquad (4.7)$$

where $T = t-t_0$ is the finite duration over which expansion is measured and $\lambda_{max}(C)$ is the maximum eigenvalue of C with the corresponding (normalized) eigenvector $\hat{e}_1(t_0)$. In other words, if δx_0 is along $\hat{e}_1(t_0)$ at time t_0, then maximum stretching occurs over the time T and the length of the perturbation vector becomes

$$\left\|\delta x(t)\right\| = e^{\sigma_1(x_0)T} \left\|\delta x_0\right\|, \tag{4.8}$$

where $t = t_0 + T$ (Shadden et al. 2005).

4.2.3 Determination of LCS

Lagrangian coherent structures (LCS, both singular and plural) are separatrices in state space, separating qualitatively different kinds of motion. These separatrices are co-dimension one boundaries in state space, i.e. n-dimensional surfaces dividing n dimensional space. Methods to generate LCS from vector fields are well established (Haller 2002; Shadden et al. 2005).

Briefly, the existing method to calculate LCS includes the measurement or calculation of a generally time-dependent vector field at each instant in time. Initial conditions at a given instant in time are allowed to evolve due to the vector field yielding a set of trajectories. From these trajectories, a finite time Lyapunov exponent (FTLE) field can be generated which represents the rate of local divergence at that instant in time. LCS are identified as the ridges in the FTLE field that separate two regions of flow (Figure 4.2). Since the locations of these boundaries are changing in a time dependent flow field, the complete vector field must be available for each instant of time.

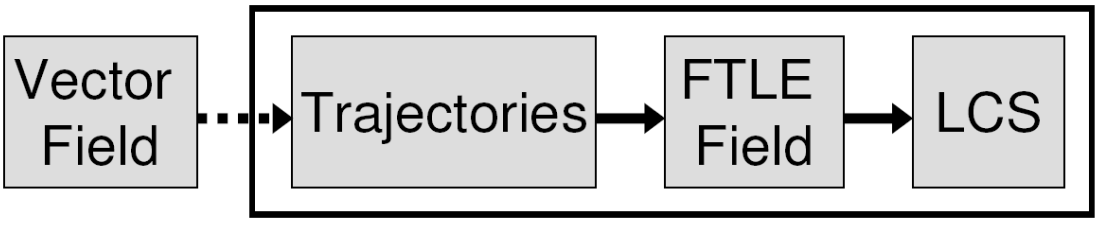

Figure 4.2: Flow chart depicting how the LCS are traditionally determined

Figure 4.3 below is used to explain why ridges develop in the FTLE field at the LCS. In this schematic representation, divergence of two points (a and b) within the stable region and two points (c and d) in the unstable region are compared. As the points a and b evolve over time, their trajectories only slightly diverge resulting in a small FTLE. This result may be plotted as a data point midway between a and b in state space. Similarly, points c and d also diverge slightly resulting in a small value for the FTLE which may be plotted midway between these two points. However, b and c which are on opposites sides of the LCS diverge greatly even over a short time. This results in a large value for the FTLE which when plotted in state space lies in the region of the separatrix. As more data points are entered, a "volcano shaped" ridge forms revealing the LCS at the separatrix.

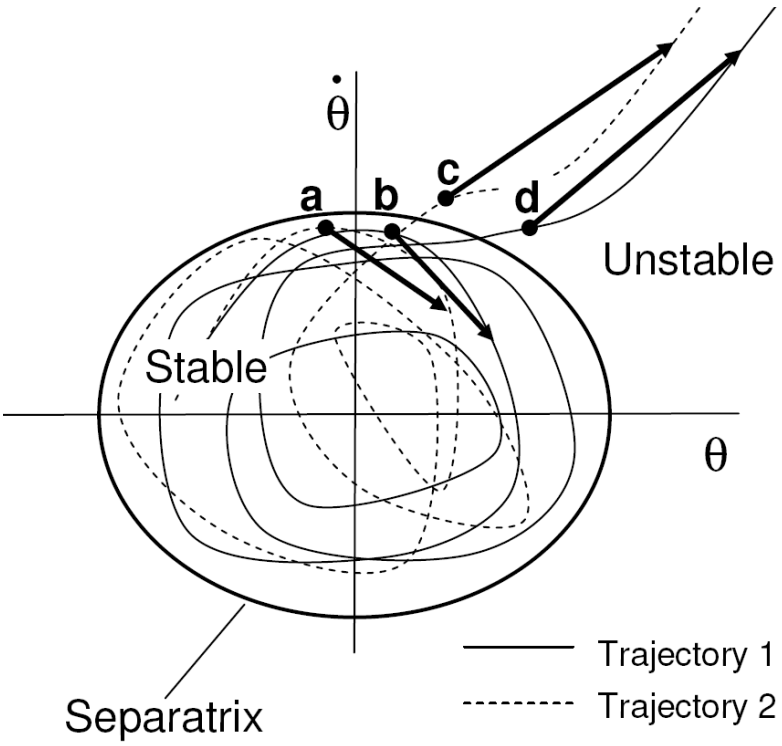

Figure 4.3: The divergence of two points on opposite sides of a separatrix is larger than the divergence of points on the same side. This generates a ridge in the FTLE field at the separatrix.

Unlike previous methods, the approach described in this paper constructs a FTLE field using only trajectory data. This eliminates the need to generate a vector field, which may not be accessible in an experimental setting. Of course, an FTLE field obtained in this way will be limited to the portion of state space sampled by trajectories.

4.3 Mathematical Model

The wobble chair has been used to isolate movement of the lumbar spine in order to gain a better understanding of the dynamics utilized to maintain torso stability and prevent injury (Figure 4.4) (Cholewicki et al. 2000; Tanaka and Granata 2007). The wobble chair consists of a seat pan and seat supported by a central ball joint. Rigidly attached to the seat is a leg rest to help minimize relative movement within the lower body. Stabilizing springs are located at the front, back, left and right of the ball joint and help to support the seat. These springs may be moved closer or further from the central pivot point to modify the amount of restorative torque provided at any given seat angle. Wobble chair experiments are typically performed at spring distances where the destabilizing gravitational moment exceeds the stabilizing spring torque. This configuration is statically unstable and neuromuscular control must be provided for the participant to maintain his/her balance on the seat. The wobble chair is able to tilt in the sagittal (forwards and backwards) and frontal (left and right) body planes, but rotation in the transverse plane and translation in all planes are restricted. The wobble chair and experimental protocol are designed to minimize relative movement within the lower body and upper body. Thus, the lower body and upper body may each be considered as rigid body segments. The lumber spine acts as a pivot between the lower and upper body segments where the center of rotation is assumed to be

located between the fourth and fifth lumbar vertebra. Given these assumptions, a person sitting on the wobble chair has four degrees of freedom (d.o.f). Two of these d.o.f. are due to the forward and backward rotation of the lower body and upper body, θ_S and θ_T, respectively. The remaining two d.o.f. are due to the left and right rotation of the lower and upper body, ϕ_S and ϕ_T, respectively. Thus, the state of the system may be described using an eight dimensional state space.

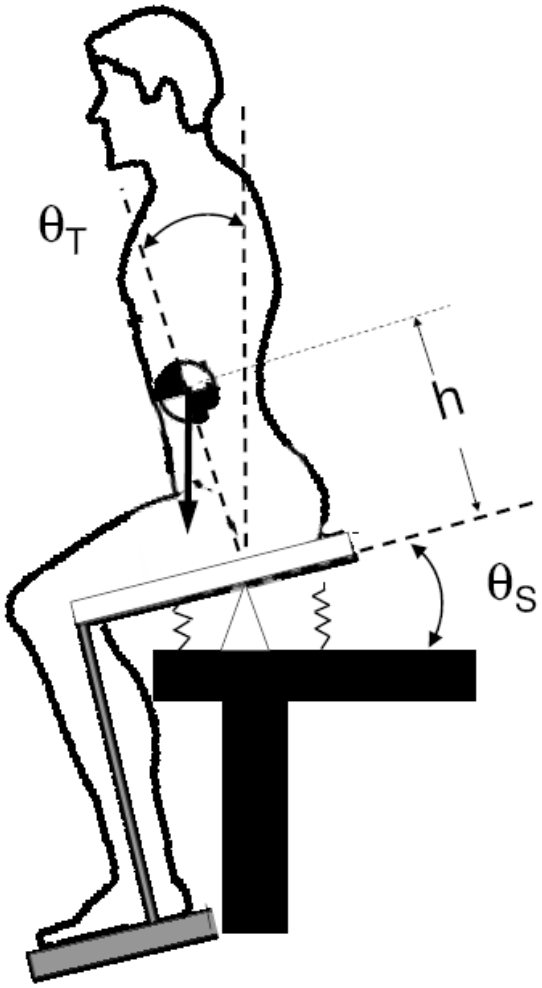

Figure 4.4: The wobble chair is an apparatus designed to isolate the movement of the low back to determine torso stability (Adapted from (Cholewicki et al. 2000; Tanaka and Granata 2007))

In order to begin to understand the behavior of the full dimensional system, a reduced model was developed for the wobble chair (Figure 4.5). In this model, motion is restricted to the sagittal plane, and the angle between the lower body and upper body is fixed. These constraints allow the system to be modeled as a planar inverted pendulum. These constraints effectively reduce the system from an 8-dimensional state space system to two dimensions. Indeed, even the 8-dimensional state space is only an approximation to the almost infinite number of dimensions inherent in the human body.

In addition to reducing the computation time, order reduction allows one to visualize system properties that may not be understandable in higher dimensions. This is the case with the LCS. In the reduced order model, the LCS are readily apparent as lines dividing 2-dimensional state space. However in the full order system, it is difficult to visualize an LCS since it exists as a 7-dimensional hyper-surface dividing 8-dimensional state space.

4.3.1 Planar Inverted Pendulum Model

The planar inverted pendulum model consists of a point mass at the end of a rigid mass-less rod (Figure 4.5). Stabilizing springs like those used in the actual wobble chair are included in the model. In addition, a proportional-derivative control is used to maintain stability. However, the gain of the proportional controller will be limited to a maximum value, thus simulating a linear increase in muscle force up to the level of maximum voluntary contraction (MVC). These stabilizing components allow the system to have a stable equilibrium point at the upright vertical position. The existence of this stable region was observed in wobble chair experiments where participants were able to balance for 60 seconds in a statically unstable configuration (Granata and Lee 2008).

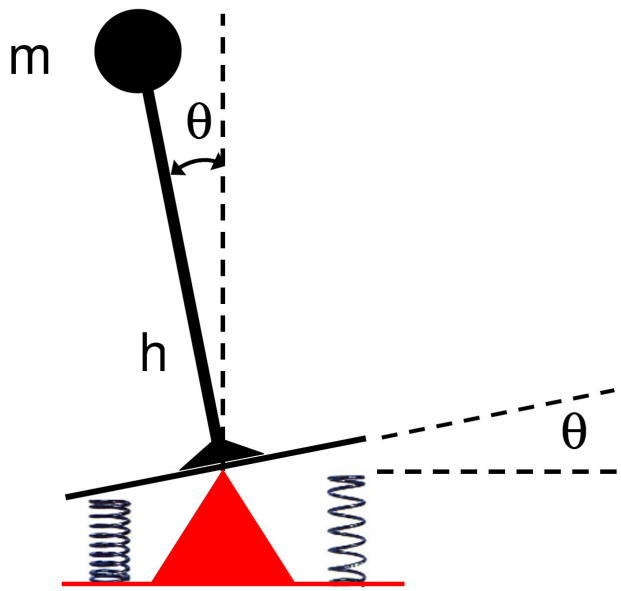

Figure 4.5: The reduced order model of the wobble chair consists of a planar inverted pendulum with stabilizing springs and a limited gain control.

The vector from the pivot to the center of mass when the pendulum is in the equilibrium position (upright vertical) is defined as **c**.

$$\vec{c} = \begin{bmatrix} 0 \\ h \\ 0 \end{bmatrix} \qquad \vec{g} = \begin{bmatrix} 0 \\ -g \\ 0 \end{bmatrix} \tag{4.9}$$

Where h is the height of the center of mass above the pivot point. The acceleration of gravity vector is given by **g** and is expressed in terms of the scalar value of g equal to 9.8 m/s^2. Rotations in the x-y plane are defined by the angle theta, θ. A rotation about the z-axis from local to global coordinates is given by the rotation matrix, R_θ.

$$R_\theta = \begin{bmatrix} Cos\theta & -Sin\theta & 0 \\ Sin\theta & Cos\theta & 0 \\ 0 & 0 & 1 \end{bmatrix} \tag{4.10}$$

Note that the transformation matrix to convert from global to local coordinates is the inverse of the transformation matrix to convert from local to global coordinates. Also, note that the inverse of a rotation matrix is its transform. In order to calculate the velocity, it is necessary to calculate the time derivative of the rotation matrix. This is obtained by using the chain rule.

$$\frac{d}{dt}(R_\theta) = \frac{d}{d\theta}(R_\theta)\frac{d\theta}{dt} = R'_\theta\dot{\theta} = \begin{bmatrix} -Sin\theta & -Cos\theta & 0 \\ Cos\theta & -Sin\theta & 0 \\ 0 & 0 & 0 \end{bmatrix}\dot{\theta} \tag{4.11}$$

The position vector in global coordinates is calculated by applying the transformation, R_θ, to the position vector in local coordinates, c.

$$\vec{x} = R_\theta \vec{c} \tag{4.12}$$

The velocity is found by taking the time derivative of the position vector.

$$\dot{\vec{x}} = \frac{d}{dt}(\vec{x}) = \frac{d}{dt}(R_\theta \vec{c}) = \left(\frac{d}{dt}(R_\theta)\right)\vec{c} + R_\theta\left(\frac{d}{dt}(\vec{c})\right)^{0} \tag{4.13}$$

$$\dot{\vec{x}} = R'_\theta\dot{\theta}\,\vec{c}$$

The potential energy, V, is a function of the height of the mass in the gravitational field and given by,

$$V = m\,\vec{g}\cdot(R_\theta \vec{c}) \tag{4.14}$$

The kinetic energy, T, is a function of the velocity of the center of mass. Since the pendulum model is a point mass, the moment of inertia of the body is zero. Thus, T is simply,

$$\begin{aligned} T &= \tfrac{1}{2}\, m\,(R'_\theta \vec{c})\cdot(R'_\theta \vec{c})\,\dot{\theta}^2 \\ T &= \tfrac{1}{2}\, m\,\|\vec{c}\|^2\,\dot{\theta}^2 \end{aligned} \tag{4.15}$$

The Lagrangian, L, is given by the difference in kinetic energy, T, and potential energy, V. The Lagrangian is computed as follows.

$$L = T - V = \tfrac{1}{2} m \left\| \vec{c} \right\|^2 \dot{\theta}^2 - m \vec{g} \cdot \left(R_\theta \vec{c} \right) \tag{4.16}$$

Lagrange's equations are applied to find the equations of motion.

$$\frac{d}{dt}\left(\frac{\partial L}{\partial \dot{\theta}}\right) - \frac{\partial L}{\partial \theta} = \tau \tag{4.17}$$

Where τ is the sum of all torques applied to the system. The equation is solved for each component.

$$\frac{\partial L}{\partial \theta} = m\vec{g} \cdot \left(R'_\theta \vec{c} \right) \tag{4.18}$$

$$\frac{\partial L}{\partial \dot{\theta}} = 2\left(\tfrac{1}{2} m \left\| \vec{c} \right\|^2 \dot{\theta} \right) \tag{4.19}$$

$$\frac{d}{dt}\left(\frac{\partial L}{\partial \dot{\theta}}\right) = m\left\| \vec{c} \right\|^2 \ddot{\theta} \tag{4.20}$$

Combining these equations yields the equation of motion,

$$m\left\| \vec{c} \right\|^2 \ddot{\theta} - m\vec{g} \cdot \left(R'_\theta \vec{c} \right) = \tau \tag{4.21}$$

This equation is further simplified.

$$\left\| \vec{c} \right\|^2 = \left\| \begin{bmatrix} 0 \\ h \\ 0 \end{bmatrix} \right\|^2 = h^2 \tag{4.22}$$

$$m\vec{g} \cdot \left(R'_\theta \vec{c} \right) = m \begin{bmatrix} 0 \\ -g \\ 0 \end{bmatrix} \cdot \left(\begin{bmatrix} -Sin\theta & -Cos\theta & 0 \\ Cos\theta & -Sin\theta & 0 \\ 0 & 0 & 0 \end{bmatrix} \begin{bmatrix} 0 \\ h \\ 0 \end{bmatrix} \right)$$

$$= m \begin{bmatrix} 0 \\ -g \\ 0 \end{bmatrix} \cdot \left(\begin{bmatrix} -hCos\theta \\ -hSin\theta \\ 0 \end{bmatrix} \right) = mghSin\theta \tag{4.23}$$

$$mh^2\ddot{\theta} - mghSin\theta = \tau \tag{4.24}$$

Solving for the angular acceleration yields the following equation.

$$\ddot{\theta} = \frac{mghSin\theta + \tau}{mh^2} \tag{4.25}$$

Four torque/moment components will contribute to the motion of the system. The first component is the gravitational moment, M_g, calculated previously.

$$M_g = mghSin\theta \tag{4.26}$$

The second component is spring torque, T_s. It is given by the spring force applied at a distance, d, from the pivot point. The spring compression is given by d*Sinθ. Using the spring constant, k, previously defined, the spring torque can be calculated.

$$T_S = F \times d = k(dSin\theta) \times d = kd^2 Sin\theta \tag{4.27}$$

The third component is limited gain proportional-derivative control, $C(\theta, \dot{\theta})$. The equation for the limited gain PD control, C, is given by,

$$C(\theta,\dot{\theta}) = G_d\dot{\theta} + \begin{cases} G_p\theta & if \quad \theta < \theta_{cr} \\ G_{p\max} & otherwise \end{cases} \tag{4.28}$$

where, G_d is the derivative gain constant, $\theta_{cr} = G_{p\ max}/G_p$ is the smallest angle at which the maximum gain is achieved, G_p is the proportional gain constant, and $G_{p\ max}$ is the maximum value of proportional gain. Physiologically, a limited gain controller represents the limited muscle strength of the abdominal and spinal extensor muscles.

The fourth component is noise. System noise, N, is introduced into the model as random force perturbations (Figure 4.6). It is simulated by a zero mean Gaussian normal distribution with a standard deviation, σ, equal to 1% of ∇G. Constraints are included in the program to bound the noise level to an amplitude of ±3σ. A noise frequency (20 Hz) is selected such that it substantially exceeds the natural frequency of the system (<~3 Hz). Physiologically, noise can

be introduced into the system from muscle twitches, inaccurate motor unit activation, involuntary movements, or external environmental forces. In order to solve the system using an ordinary differential equation (ODE) solver, it is necessary to determine the noise at each time instant prior to solving the ODE. Within the ODE, the noise at any time can be interpolated from the closest predetermined values allowing the solver to converge on a solution. This method is necessary because the solver will be unable to converge on a solution if the noise is randomly determined within the system dynamics subroutine. For the simulation, Gaussian random noise is be calculated at a frequency of 20 Hz and an amplitude of 3 standard deviations equal to 1% of the gravitational gradient.

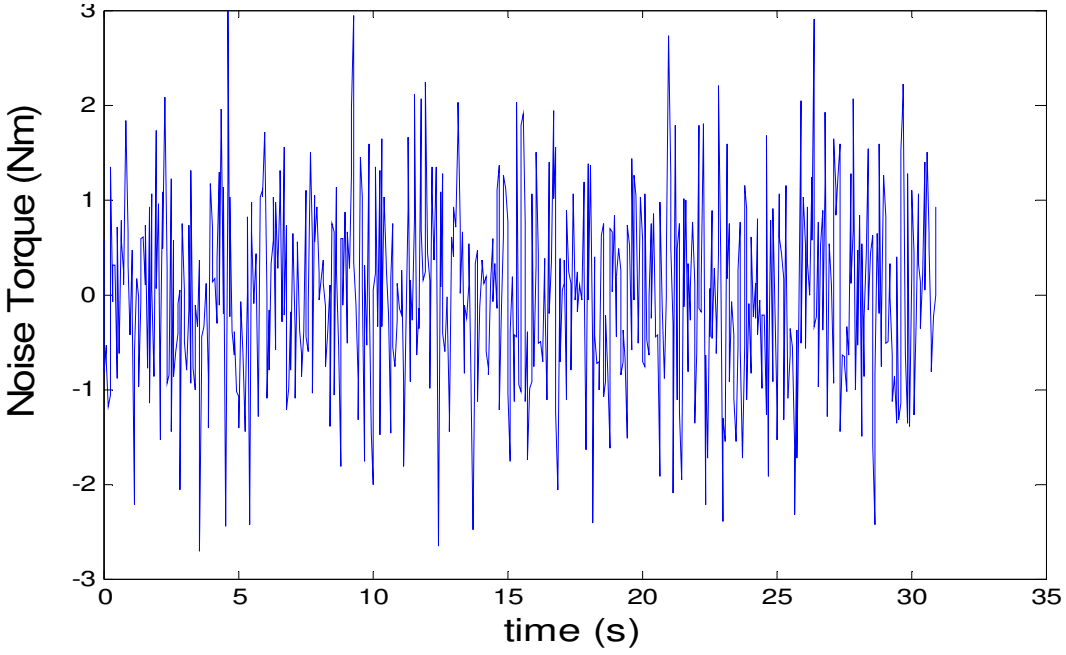

Figure 4.6: Gaussian random noise with a frequency of 20 Hz, and amplitude of 3 standard deviations equal to 1% of the gravitational gradient.

Thus, the reduced order model, hereafter referred to simply as the model, is governed by the following differential equation

$$\ddot{\theta} = \frac{mgh\sin\theta - kd^2\sin\theta - C(\theta,\dot{\theta}) + N}{mh^2} \qquad (4.29)$$

where, $\ddot{\theta}$, m, g, h, θ, $\dot{\theta}$, k and d are the angular acceleration, mass, acceleration of gravity, height, rotation angle, angular velocity, spring stiffness, and the distance of the springs from the central ball joint respectively.

4.3.2 Effective potential function

In the mathematical model, the limited gain control causes a well to develop in the effective potential energy curve of the system, V_{eff}, at the upright vertical position (Figure 4.7). This potential energy well acts as a local attractor in state space. Physiologically, this well allows the participant to balance near the vertical position. However, larger perturbations that exceed the well's dimensions in state space will cause the participant to fall away, hence being repelled from the vertical position. Thus, the well is of finite size, and the system is not globally stable.

Insight into the system's behavior can be gained by examining the effective potential function

$$V_{eff} = mgh\cos\theta - kd^2\cos\theta + \begin{cases} \frac{1}{2}G_p\theta^2 & if \quad \theta < \theta_{cr} \\ \frac{1}{2}G_p\theta_{cr}^2 + G_{p\max} & otherwise \end{cases} \qquad (4.30)$$

which is the sum of all the potential functions. When the distance from the stabilizing springs to the central ball joint is small, the upright vertical position is unstable. As the springs are moved further out, the upright vertical position remains unstable until the threshold of stability is reached. A well forms in the potential curve at the upright vertical position upon reaching the

threshold of stability. This well is a region of local stability (Figure 4.7). The size of the well may be enlarged by increasing the restorative torque provided by the springs or the controller gain.

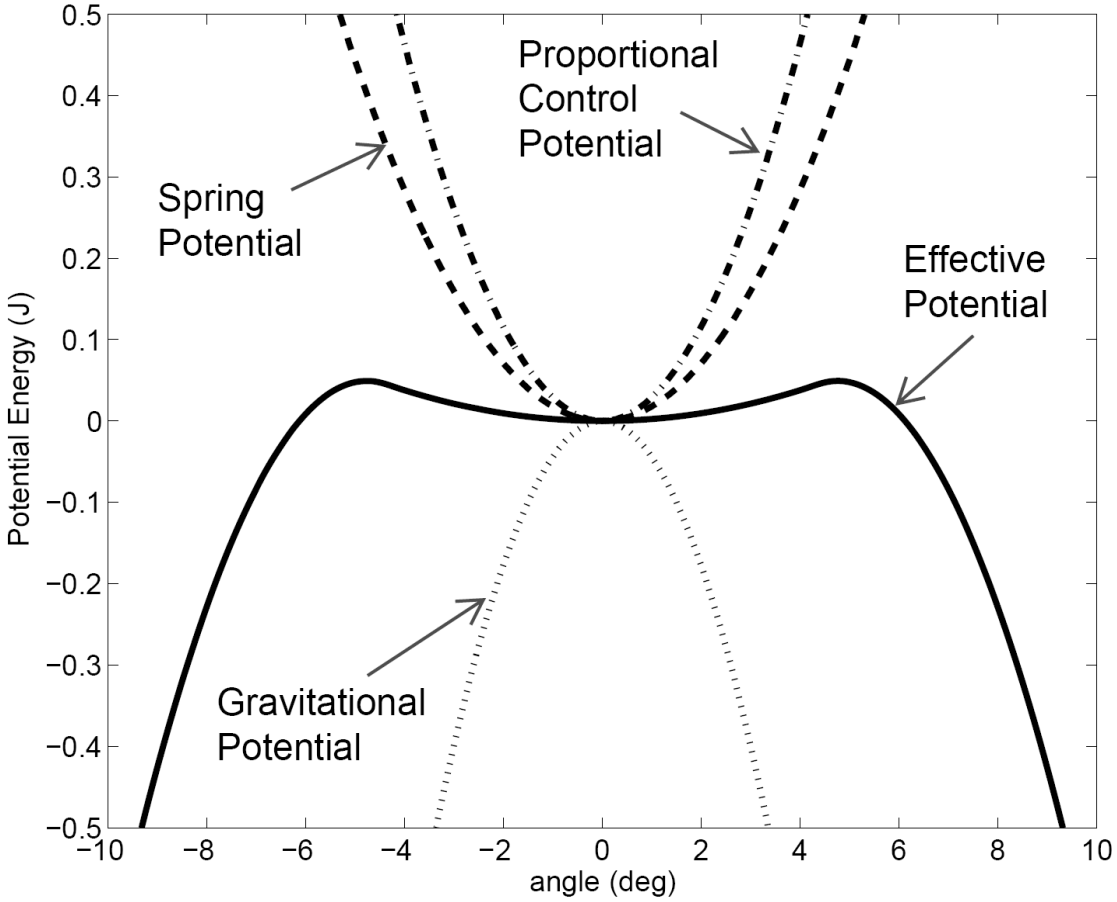

Figure 4.7: The effective potential energy function is the sum of the individual components. Under some conditions, a potential well develops near the equilibrium point.

This stable region may be visualized by examining iso-energy plots and the flow map in state space (Figure 4.8 in section 4.4.1). The flow map may be divided into two distinct regions based on the type of motion. The first region is characterized by elliptical orbits centered around the equilibrium point. The second region is characterized by hyperbolic orbits. The heteroclinic

orbit separates the two regions and also locates the material flow lines on which the hyperbolic orbits are aligned.

4.3.4 Model Calibration

The model may be calibrated to match anthropometric data of a typical participant performing tests on the wobble chair. In order to calibrate the apparatus for a specific participant, the gravitational gradient of the subject is determined. The gravitational gradient, ∇G, is defined as $\partial M_g/\partial\theta$, where M_g is the moment about the pivot due to gravity. ∇G is a function of the participant's body mass and mass distribution.

For this simulation, model parameters were selected to match typical values for participants (Table 4.1). A participant with a mass of 69 kg and a gravitational gradient of 291 Nm was used. The resulting height of the center of mass was calculated to be 43.0 cm. Using the wobble chair spring stiffness of 10,900 N/m, the distance from the springs to the pivot was calculated to be 10.35 cm for a spring setting of 40% ∇G.

An important indicator of the participant's neuromuscular control capability is the threshold of stability. This parameter is the minimum value of the restorative force (i.e. spring distance) at which the participant is able to maintain balance on the wobble chair. Its value is expressed as a percentage of ∇G. Pilot data collected from two healthy subjects yielded a typical value of 35% ∇G. The model was calibrated by modifying the controller values, G_p and $G_{p\,max}$, so that the threshold of stability matched the value found experimentally.

Table 4.1: Model Parameters for the Reduced Model

parameter	value	source
m	69 kg	typical subject
g	9.81 m/s^2	typical subject
h	43.0 cm	calculated from ∇G
k	10,900 N/m	wobble chair
d	10.35 cm	value to generate 40% ∇G
G_d	1 Nm/(rad/s)	calibration parameter
G_p	190 Nm/rad	calibration parameter
$G_{p\ max}$	14.5 Nm	calibration parameter

4.4 Nonlinear Analysis

In this section, nonlinear analysis techniques are applied to study how the model behaves under different conditions and using different analysis techniques. First, the parameters of the human postural control model will be set so that the system is deterministic and conservative. This model will be used to generate a vector field from the governing differential equation. It will then be shown how the Lagrangian coherent structures calculated from this vector field align with the lines associated with the heteroclinic orbit. Second, random noise and a damping component will be introduced to this deterministic model. The vector field generated from this model will be used to determine the LCS for this scenario. Third, a model of human postural control will be used to generate simulated experimental data in the form of a single trajectory. The trajectory will be analyzed and it will be demonstrated that the LCS can be found without a vector field.

4.4.1 Deterministic and Conservative Simulation

For the deterministic and conservative simulation, the system noise and damping function of the controller are set to zero. The system is modeled using MATLAB (MathWorks, Natick,

MA). Since the system in its current configuration is conservative, the heteroclinic orbit can be determined by generating an iso-energy contour in state space where the total energy is equal to the maximum effective potential energy. The heteroclinic orbit along with lower and higher energy orbits are shown in Figure 4.8.

A vector field is generated from a regular grid of points in state space centered around the upright vertical position. Each of these points are taken as an initial condition to determine the flow map as the vector field evolves over time. The differential equation [4.9] is solved using a Runge Kutta (4,5) ordinary differential equation solver function (MATLAB function ode45). The forward time flow map for the system is shown to correlate well with the iso-energy orbits in Figure 4.8.

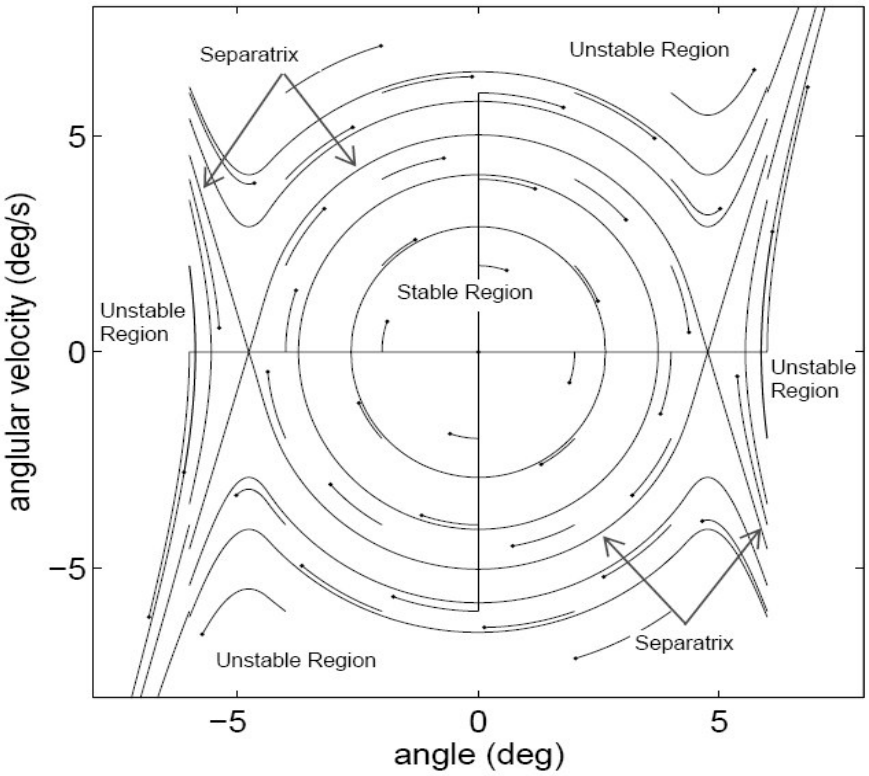

Figure 4.8: Orbits and flow map for the deterministic conservative configuration. Lines ending with a point show the resulting trajectories based on the initial conditions. The heteroclinic orbit is a separatrix between the stable and unstable regions.

The FTLE is calculated for each point on the interior of the grid based on the expansion of the state transition matrix. These results are combined over state space to produce a FTLE field. The FTLE field was first calculated by flowing time forward 3 seconds. Recalling that the LCS are ridges of the FTLE field, these structures form a "volcano" like shape in the three dimensional view (Figure 4.9).

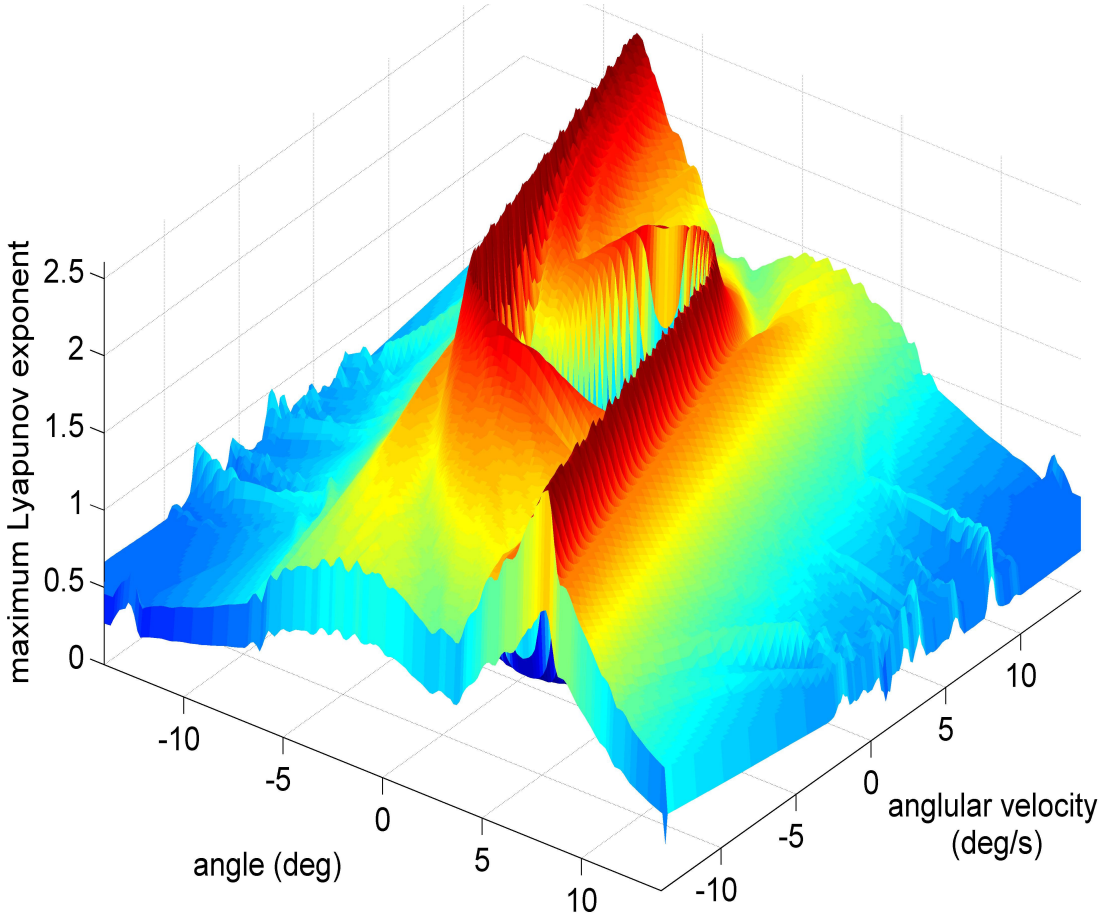

Figure 4.9: The 3D view shows the LCS to be easily observable as ridges in the FTLE field. This plot was generated from a 200 by 200 point grid over a range of ±15 degrees by ± 15 deg/sec.

Viewing Figure 4.9 from the top (Figure 4.10), the LCS are observed to align well with the iso-energy lines associated with the heteroclinic orbit. A ridge is formed around the heteroclinic orbit which separates stable motion near the upright vertical position from unstable motion further from the origin in state space. In addition, two other LCS are noticeable. In the lower right, an LCS generates a hyperbolic material line (Haller 2002) that is aligned with the iso-energy line associated with the heteroclinic orbit. As the trajectory approaches the heteroclinic orbit, the flow on either side of the LCS splits. Physically, this represents initial conditions beginning in the unstable region with large angles and large negative angular velocities. As the trajectories approach the heteroclinic orbit, those trajectories on the right side of the LCS have insufficient kinetic energy to reach the stable region of state space before achieving zero velocity. As time progresses, this trajectories fall back in the direction from which they came.

Trajectories on the left side of the LCS have sufficient energy to approach the upright vertical position. In fact, these trajectories have too much energy to enter the stable region of state space, and they pass over the vertical position to the other side. For the conservative and deterministic system, there does not exist an approach from the unstable region of state space that results in an orbit within the stable region. The LCS forms an impenetrable barrier between the two regions. The LCS in the upper left describes motion analogous to the LCS on the lower right but approaching from the other side.

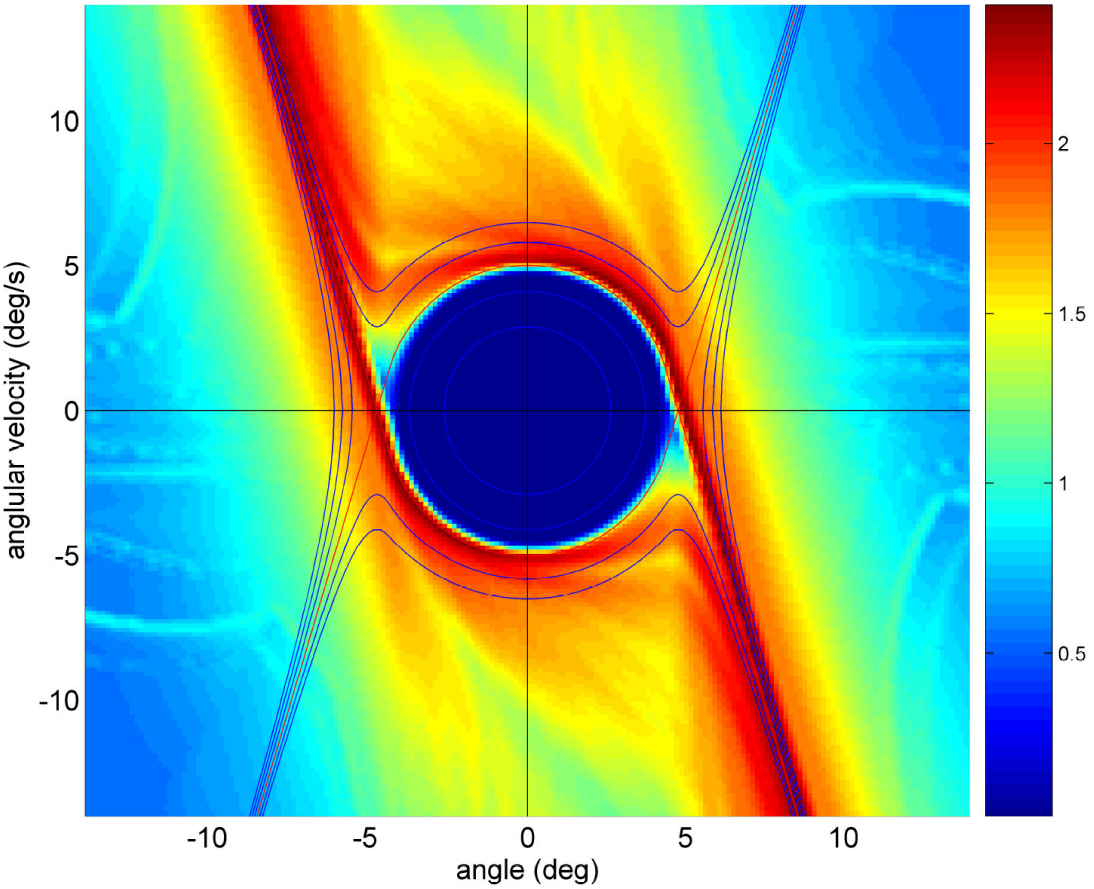

Figure 4.10: LCS form separatrices in the forward time flow (T = 3 seconds). Locations of the LCS matches well with the heteroclinic orbit and its isoenergy lines.

The LCS can also be generated for the backward flow of time (Figure 4.11). In this case, the LCS indicates divergence of the backward time flow which can be equally viewed as convergence of the forward time flow. Once again, the LCS are observed to correlate with the line associated with the heteroclinic orbit. Notice that an LCS is also present around the heteroclinic orbit in the backwards time flow. Thus, this separatrix exists in both temporal orientations (i.e. it is not an attractor of trajectories). An LCS associated with convergence is observed in the upper right. Physically, this LCS represents the convergence of two groups of trajectories. Trajectories to the right of the flow approach the LCS after having insufficient

energy to reach the heteroclinic orbit. Flow lines to the right of the LCS originally approached form the opposite side, passed over the upright vertical position, and continued past the stable region with too much energy to stop. These two trajectories converge with each having only slightly different energies. Like the forward time flow, LCS also from an impenetrable barrier between the two regions in the backward time flow.

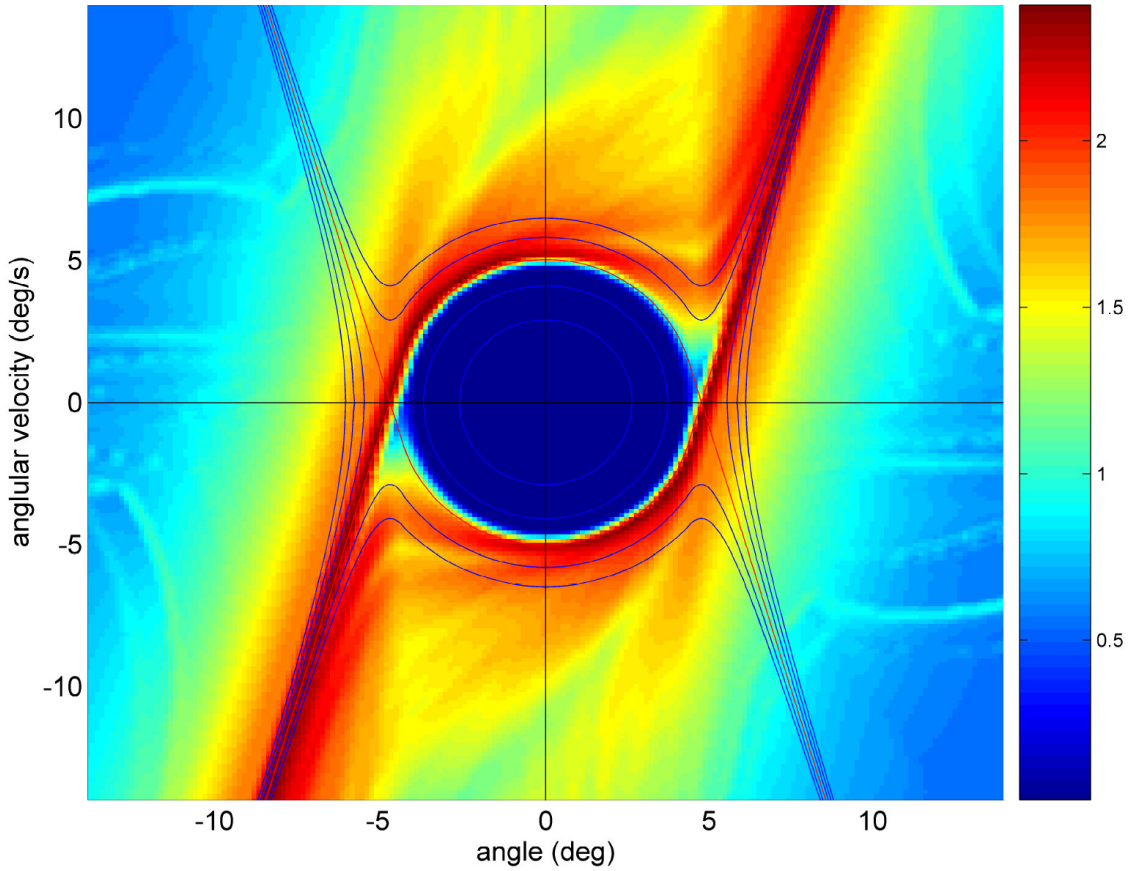

Figure 4.11: LCS form separatrices in the backward time flow. Locations of the LCS match well with the heteroclinic orbit and its isoenergy lines.

Depending on the system, the LCS may have different meanings. In this case, the LCS forms a boundary or separatrix between the region of stable postural sway (around the origin) and unstable falling motion (beyond the boundary). In this biological example, the

characteristics of the stable region and its boundary location depend on the accuracy of a number of neurological sensory systems, the feedback gain associated with core muscle strength, and the time delay of the postural control system.

4.4.2 Deterministic Simulation with Noise

In the previous section, the noise level and the damping component were set to zero making the system deterministic and conservative. In this section, noise and damping are introduced to better approximate the actual system. Taking these factors into account in equation [4.9], the flow map is generated (Figure 4.12). For reference, the orbits for the conservative deterministic configuration are also shown.

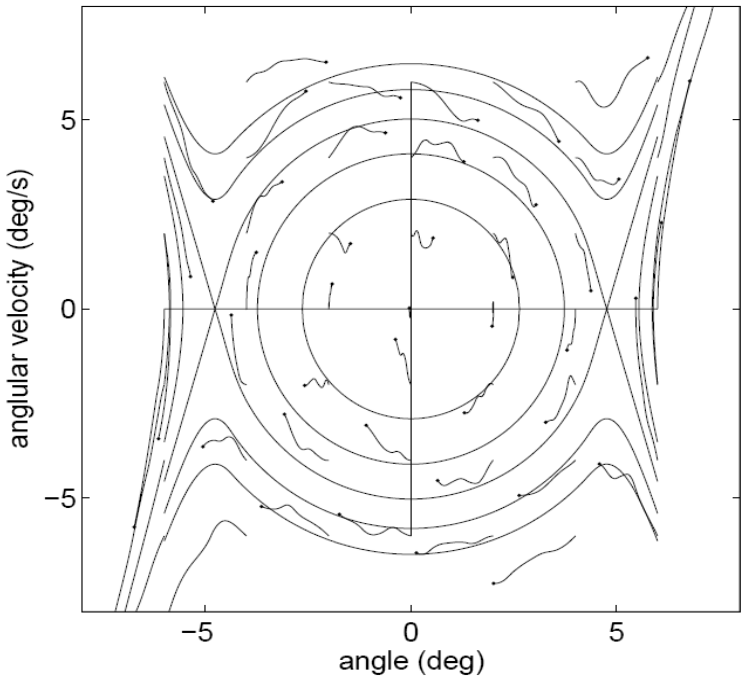

Figure 4.12: The flow map evolved over 0.3 seconds for the damped system with noise is plotted simultaneously with the orbits for the conservative deterministic configuration.

This damping has the effect of reducing the system energy attracting the trajectories towards the origin in state space. This is observed as a slight inward arcing of the flow paths

over the 0.3 second evolution time. Random noise slightly perturbs the trajectories as they evolve making the system no longer deterministic. This has the potential to have a dramatic effect on the future of a trajectory. Trajectories near the LCS may be perturbed to the opposite side crossing the barrier. Thus, stable trajectories may become unstable, and unstable trajectories may become stable. Shifts may also occur over the hyperbolic material lines. The forward (Figure 4.13) and backward (Figure 4.14) time flow plots are shown for the noisy damped configuration. Notice that the perturbations cause the LCS to be less distinct than the noise free LCS. However, the location of the LCS is unaltered, and it is still very noticeable despite the presence of noise. By rotating Figure 4.13, the ridge of the FTLE field is apparent (Figure 4.15).

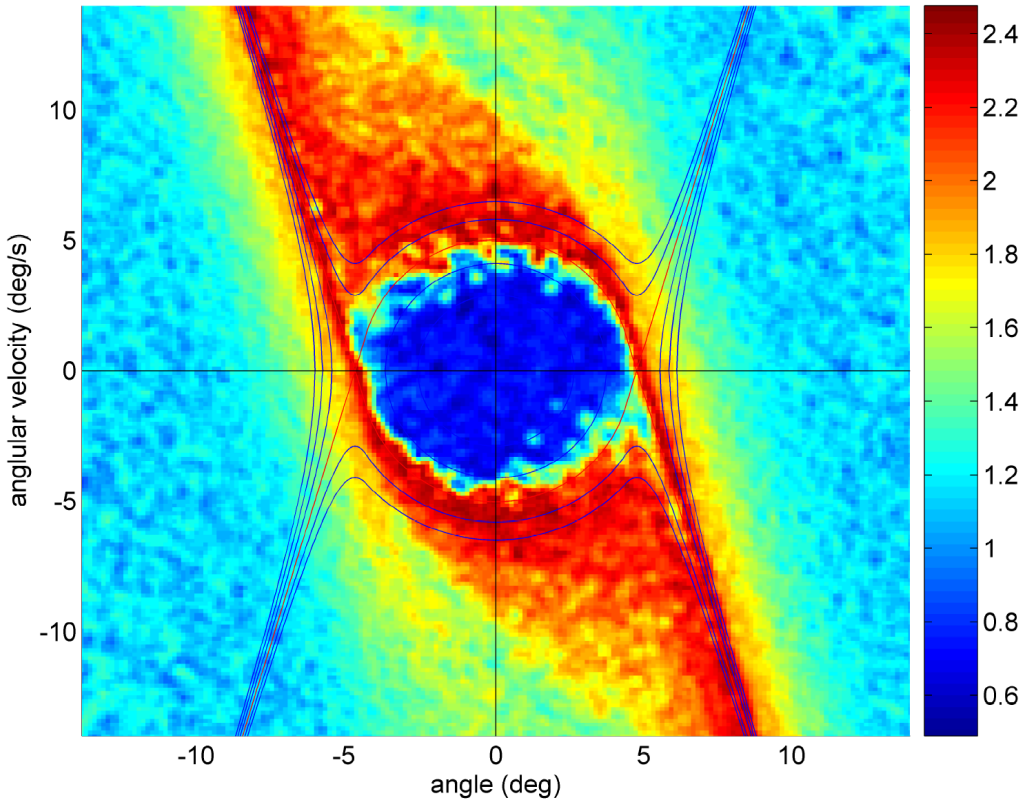

Figure 4.13: The location of the LCS aligns well with the lines of the heteroclinic orbit in the forward time flow damped system with noise. Although the flow is more diffused than the conservative noise free system, the results are essentially the same.

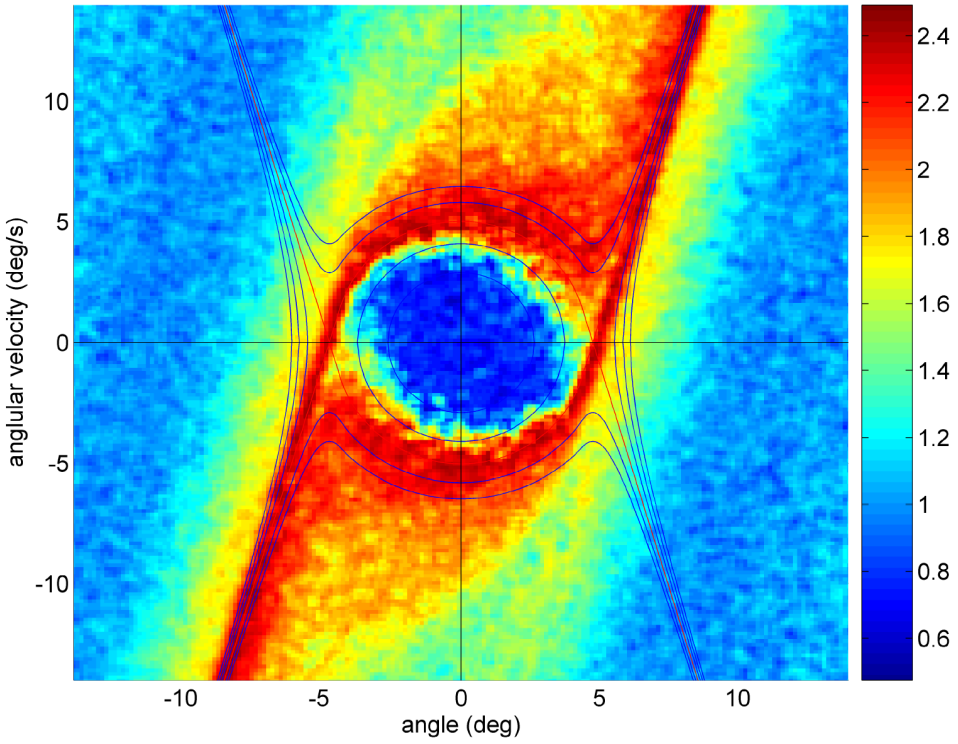

Figure 4.14: The backward time flow analysis shows LCS that also align well with the lines of the heteroclinic orbit for the damped system with noise.

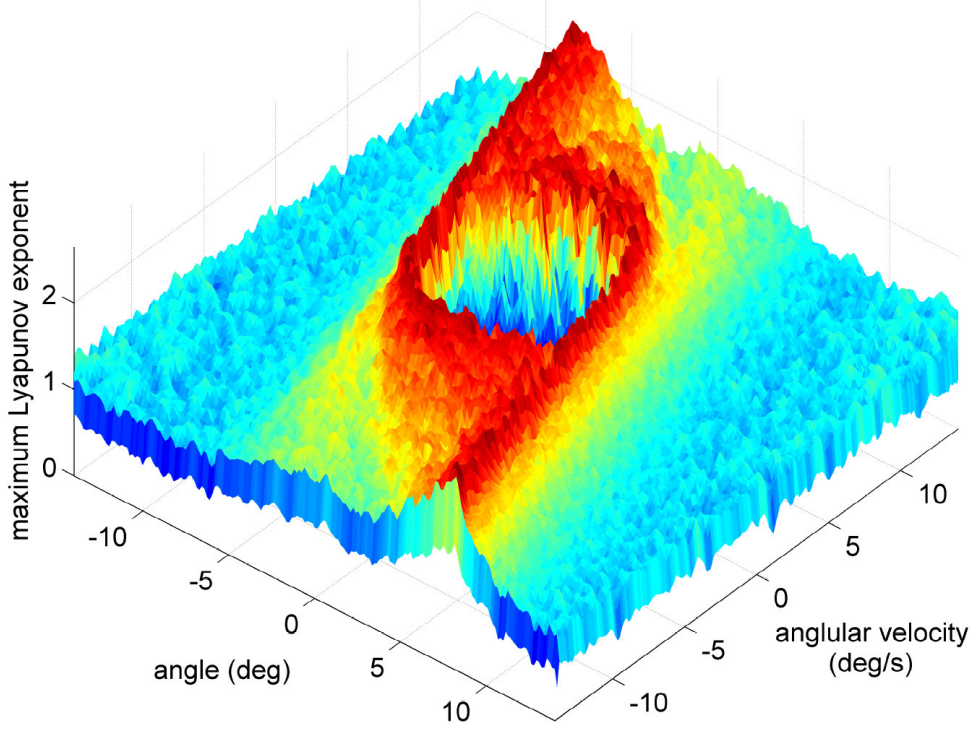

Figure 4.15: The LCS can be easily observed in a 3 dimensional plot of (Figure 4.13).

4.4.3 Generation and Analysis of Simulated Experimental Data

The next step toward evaluation of the real biodynamic system is to simulate trajectories similar to those recorded during experiments. In this simulation, the system begins at the origin in state space and is perturbed with Gaussian random force perturbations. These forces generate movement that is attenuated by a controller. As a result, the system is able to maintain stability for a period of time before a sequence of perturbations causes the system to become unstable (unrecoverable). Physiologically, this represents a person balancing on the wobble chair initially having a tilt angle and angular velocity equal to zero. During the experiment, system noise causes the person to sway, and neuromuscular control effort must be applied to maintain a stable upright posture. The angle is recorded for each segment (lower and upper body) typically at a frequency of 100 or 1000 Hz. Each simulated trial lasts 30 seconds or until the trajectory becomes unstable and diverges beyond a certain boundary (15 degrees). Twenty independent trials are generated from the model, and the results are concatenated into a single trajectory (Figure 4.16). This trajectory represents a single biodynamic experiment in which the participant spends time balancing near the equilibrium point and falling.

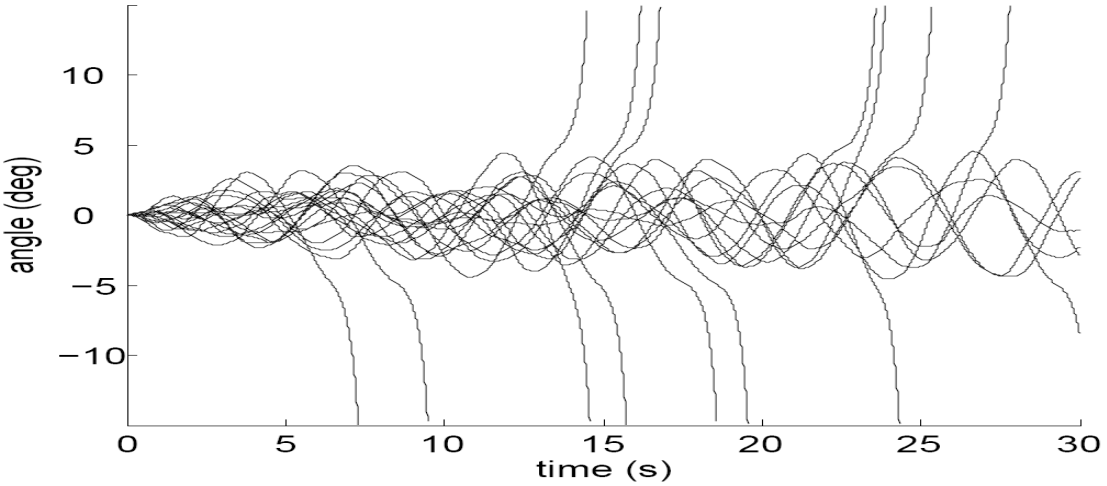

Figure 4.16: The time-series data analyzed came from several simulated experimental trials.

Unlike vector field data which is much richer, a single trajectory only contains information about one point in state space at any instant of time. In order to compensate for this deficiency in information, data are collected as the trajectory explores different locations in state space over the duration of the experiment. Since the system is assumed to be autonomous, these data can be combined to generate a FTLE field even though the locations in state space may have been explored at times separated by several seconds or minutes. Furthermore, the lack of a complete vector field introduces new challenges. Unlike a vector field which is continuous over space, time series data, viewed as trajectories, may be sparse or absent in many regions of state space. As a result, the FTLE field may be incomplete, and only portions of the state space may be evaluated. Therefore, an important aspect of both an experiment and a simulation is that the trajectory spans as much of state space as possible. This is especially important when trying to locate LCS because it is not possible to experimentally determine their locations unless data is available on both sides of the LCS.

With the simulated trajectory now generated, it is possible to conduct the numerical analysis. However, in order to better understand the numerical simulation, the theoretical basis for calculating the FTLE field from a single trajectory first will be illustrated. The maximum FTLE field can be approximated if it is assumed that the direction of maximum expansion dominates the dynamics of perturbations in arbitrary directions (Rosenstein et al. 1993b). Under this assumption, equation [4.7] is presumed to hold for all perturbation vectors regardless of their initial state space direction. This will result in a lower bound approximation to the actual value since the perturbation direction will not be exactly aligned with the direction of maximum expansion. As the focus is now on the maximum FTLE, the maximum FTLE will be referred to as simply the FTLE hereafter.

The FTLE is estimated as the rate of separation of neighboring trajectories. In order to understand how this is determined from experimental data, consider the reference trajectory shown in Figure 4.17. With a reference point established, a target location p_1 is identified that is a perturbation distance δq from the reference point in state space. The data point closest to p_1 on another trajectory, n_1, is then found. This other trajectory can be from either a different run of the experimental trial or another portion of the same trial separated by a sufficient amount of time to avoid a strong correlation with the reference point. This process is repeated for other state space directions. Using this method, 2n neighbors are found for each reference point corresponding to positive and negative directions of each dimension of state space. If multiple nearest neighbors are considered, perturbations are sampled in multiple state space directions which increases the likelihood of a separation lying in the direction of maximum expansion.

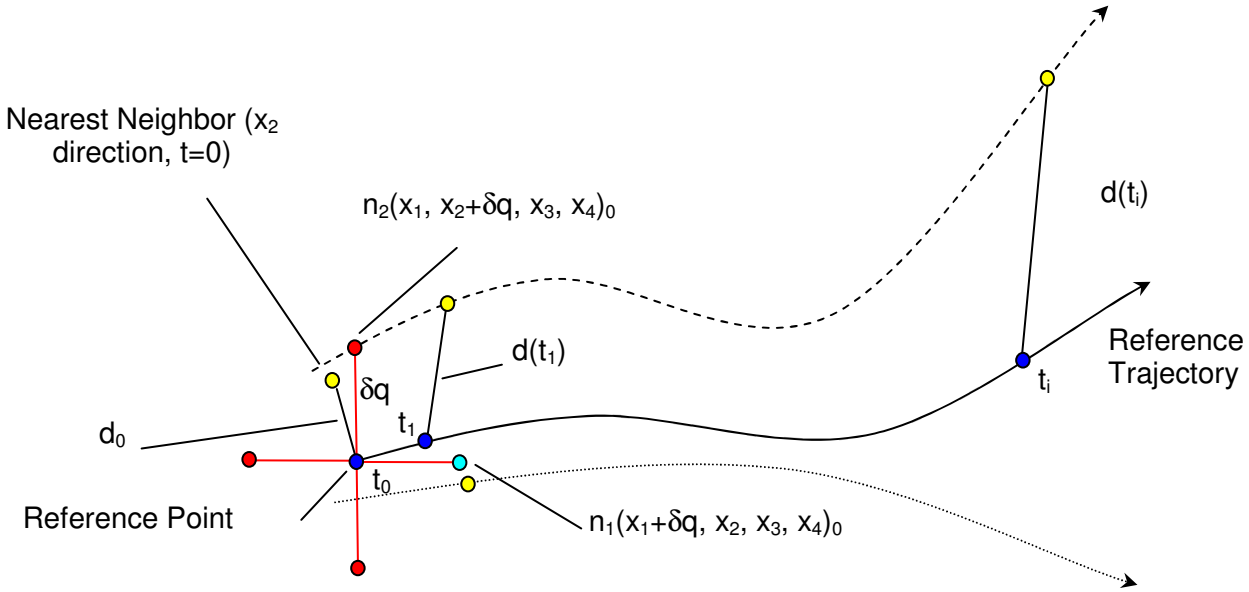

Figure 4.17: The maximum FTLE is found by calculating the growth of perturbation vectors in multiple state space directions. The assumption is made that the maximum FTLE dominates the evolution of the perturbation vectors.

Each point in the data set is sequentially evaluated by considering it to be a reference point. The FTLE is calculated for each pair. Unlike previous biomechanics analyses that averaged the FTLE over time and space (Wolf et al. 1985; Rosenstein et al. 1993b; Akay 2006; England and Granata 2007), the FTLE value over a finite time, T, is associated with a state-space location. Since the expansion will be calculated based on two points, the reference and the neighbor, it is logical to assign the expansion value to the midpoint between these two points (green points) (Figure 4.18).

In this way, the state space distribution of the FTLE is developed. The FTLE field is generated by placing an n-dimensional grid over the state space and using the distribution of the FTLE to generate an n-dimensional surface. At each state space location, x, the height of the surface is the scalar value $\sigma_1(x)$ from equation [4.6].

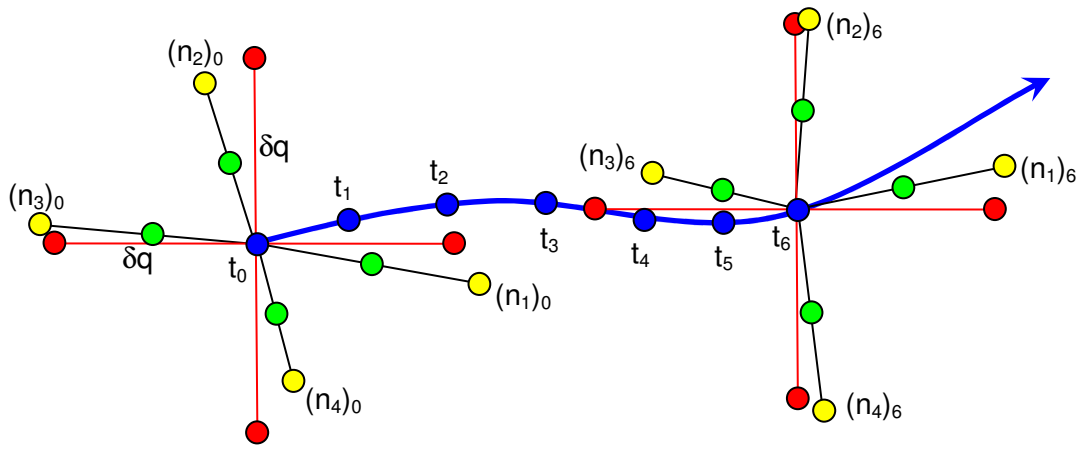

Figure 4.18: Values for the finite time Lyapunov exponents were stored in a location midway (green) between each reference (blue) and each nearest neighbor (yellow). These values were used to generate the FTLE field in state space.

The choice of δq may influence the FTLE field. The perturbation distance δq is a coarse-graining parameter selected to be large enough to overcome system noise and small enough to reveal local features of the FTLE field. However, parameter sensitivity analysis shows this method to be relatively insensitive to the value of δq. Reductions in the value of δq by two orders of magnitude reduced the smoothness of the FTLE field but did not change the locations of the LCS.

Using the approach described above, a numerical analysis was performed to calculate the FTLE field from trajectory data. In both the mathematical model and wobble chair experiment, angular position data was available for each d.o.f. of the system. Since the velocities can easily be calculated from the position data, actual d.o.f. were available for all dimensions of state space. As a result, there is no need to reconstruct state space using the method of delays as others have done. For the mechanical system being modeled, the measured coordinate (q) was used to numerically construct the time derivative ($\dot{q}$). These two parameters form the 2D state space of $x = (q, \dot{q})$. However, note that the method of using an FTLE field to find LCS is not tied to any particular means of state space construction.

Analysis of the simulated experimental data for an evolution time of 0.6 seconds is shown in Figure 4.19. At this short evolution time, the LCS begins to form near the ejection regions of state space. These ejection regions are located to the upper right and lower left of the heteroclinic orbit. For short evolution times these are the locations where rapid divergence occurs. However, unlike the vector field simulations presented earlier that map the flow of both unstable and stable trajectories, the simulated experimental data only maps stable trajectories and initially stable trajectories that become unstable. As a result, the hyperbolic material lines associated with the approaching unstable trajectory are not present. Despite being less complete

than the LCS generated from vector field data, the displayed portion of the LCS generated from trajectory data matches well with the location of the heteroclinic orbit and the LCS found from the vector field of the underlying conservative system (Figures 4.10 & 4.13).

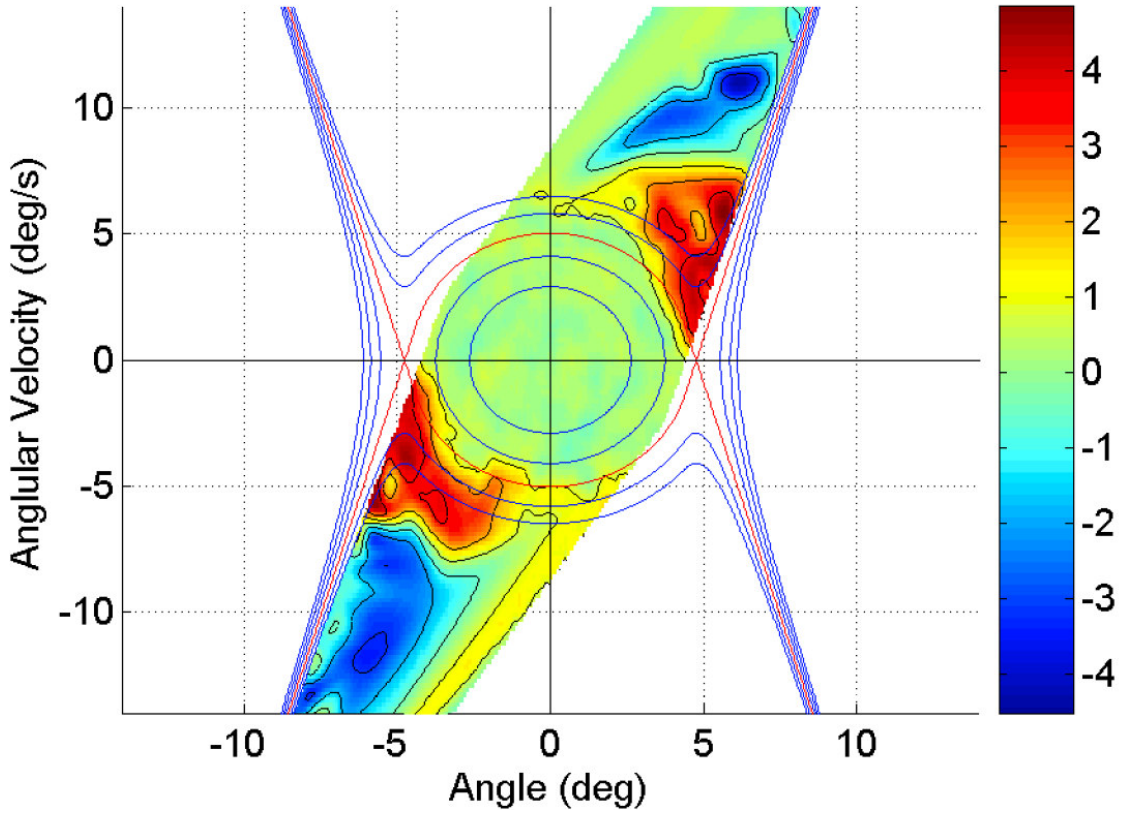

Figure 4.19: At an evolution time of T = 0.6 seconds the LCS is observable near the ejection points in state space.

For a longer evolution time, 1.2 seconds, the dominant peaks of the LCS shift further to the left on the top portion of the heteroclinic orbit and further to the right on the bottom portion (Figure 4.20). The LCS still aligns well with the heteroclinic orbit and for this evolution time covers the heteroclinic orbit in the first and third quadrants. In addition, the LCS still matches well with the location of the LCS generated from vector field data. The reason why the LCS is visible over a large portion of state space is a result of the longer evolution time. Consider two

near points on opposite sides of the LCS on the upper portion of the heteroclinic orbit. Trajectories that originate more to the left will flow together further before reaching the ejection region where their orbits split. As a result, trajectories originating from this region require longer evolution times before the LCS is noticeable. A similar condition exists on the lower portion of the heteroclinic orbit where trajectories originating more to the right flow together longer.

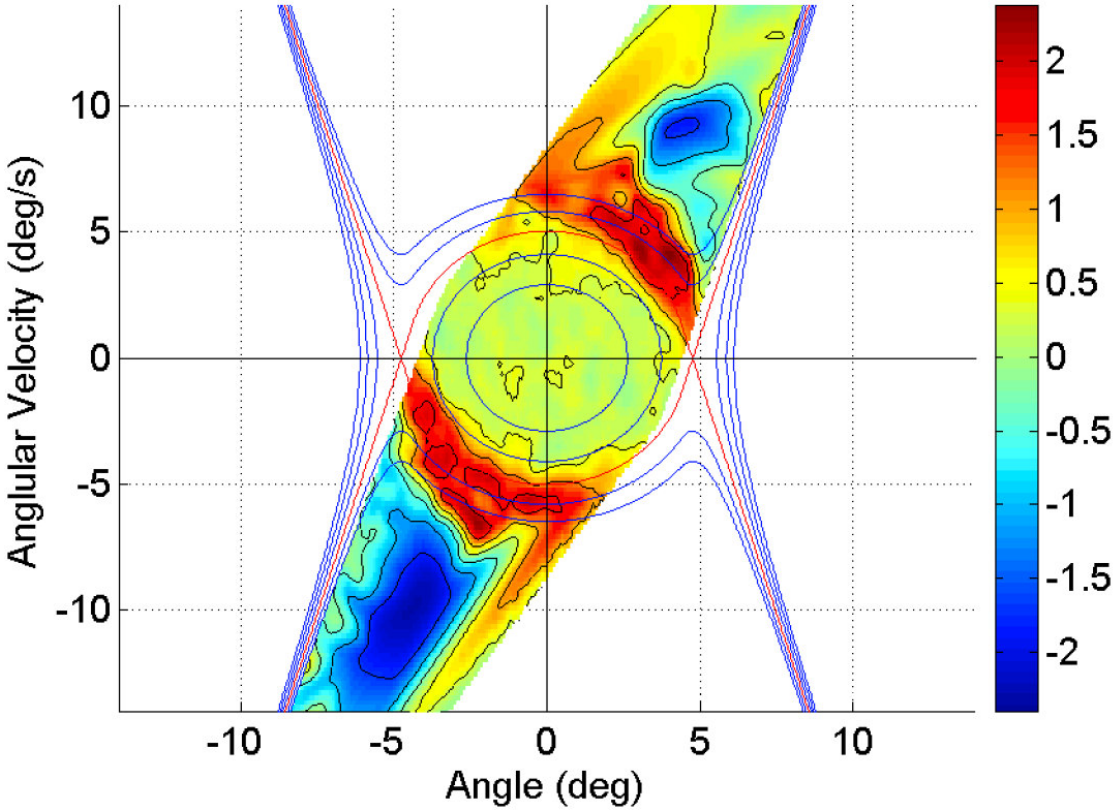

Figure 4.20: By T = 1.2 seconds the LCS is clearly observable spanning more of the boundary.

For an even longer evolution time, 1.8 seconds, the visible portion of the LCS continues to rotate in the counter clockwise direction (Figure 4.21). By an evolution time of 2.0 seconds the LCS is visible near the opposite side of the heteroclinic orbit. Increasing the evolution time

beyond 2 seconds only results in a loss of contrast in the FTLE field with no new information becoming available (Figure 4.22).

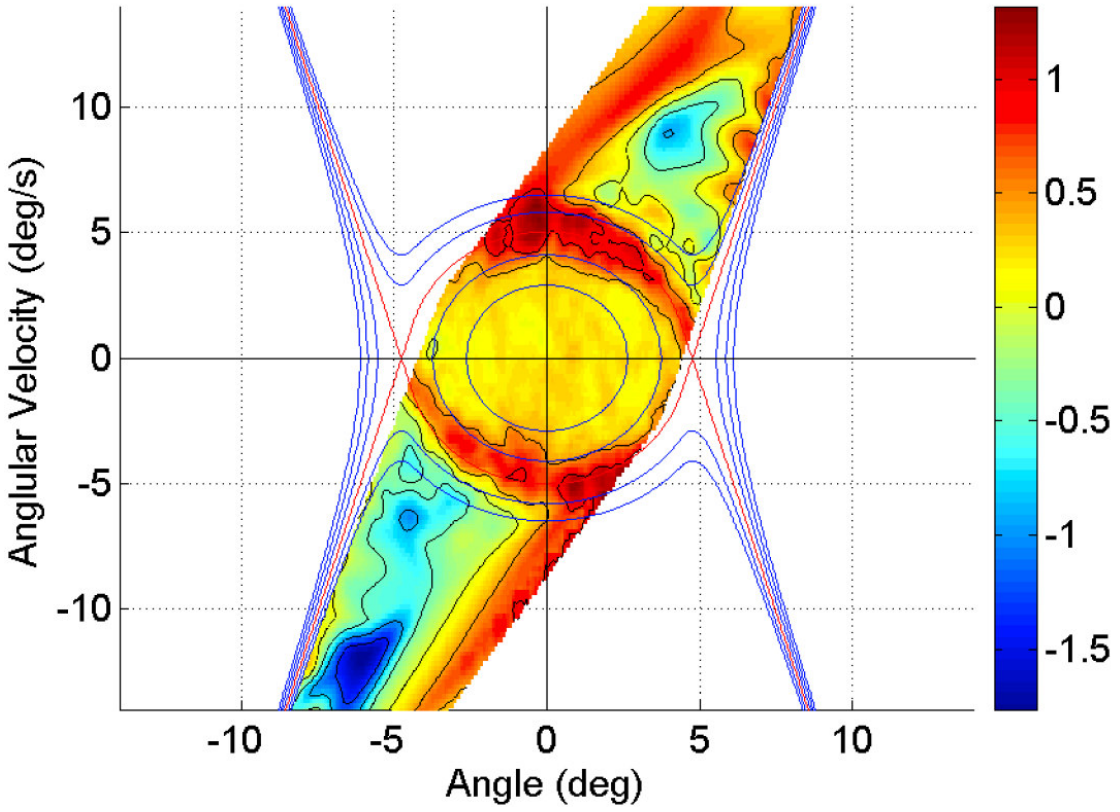

Figure 4.21: By T = 1.2 seconds the LCS is clearly observable spanning more of the boundary.

Although 20 trials were evaluated for this simulation, a separate simulation indicates that LCS structures may be identified with as little as two time series using this method. However, smaller trial numbers will tend to be more affected by random noise than larger sets because the net effect of random noise reduces as the number of trials increases.

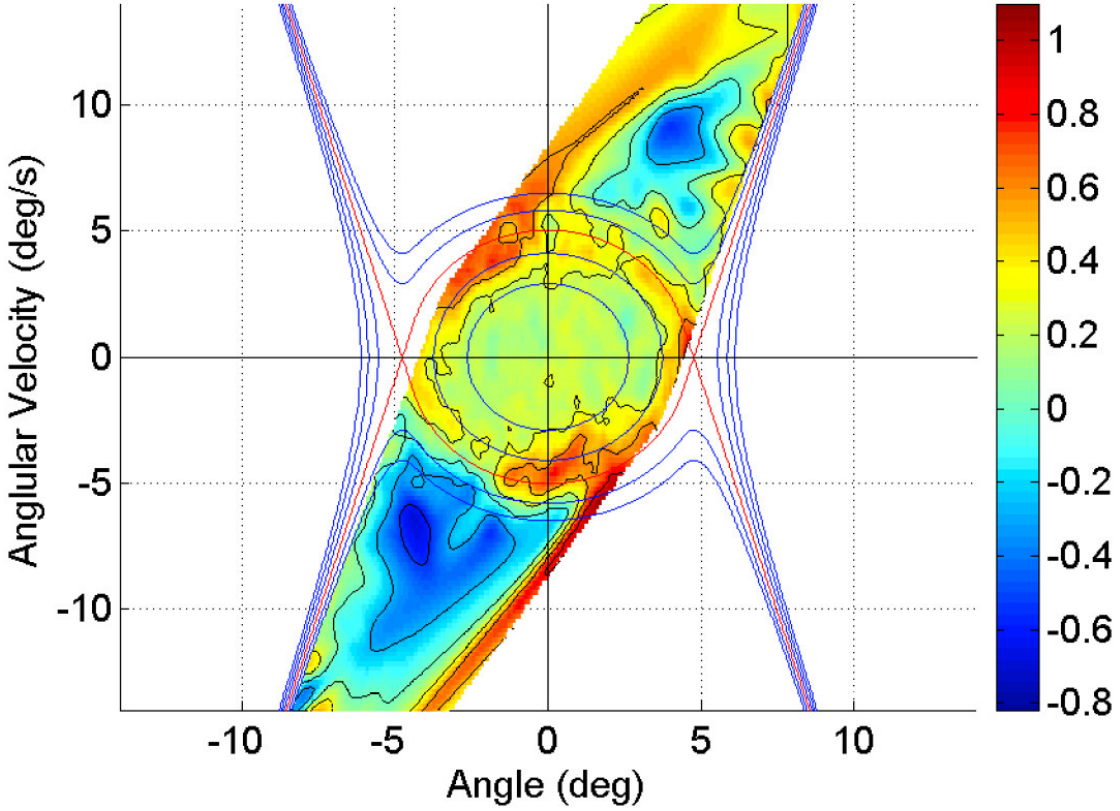

Figure 4.22: FTLE field at an evolution time, T = 2.4 seconds.

4.5 Conclusions

In this chapter, it has been shown how boundaries that separate qualitatively different kinds of motion can be found using the method of Lagrangian coherent structures applied to time series data. This is different than previous approaches to computing the LCS that required a vector field to be known. Its has been demonstrated that the location of the LCS aligned well with the heteroclinic orbit, a separatrix, of the underlying conservative system even in the presence of system noise. A demonstration of a computational method to find LCS using only trajectory data as is commonly obtained from time series data from biomechanics experiments has also been presented. The LCS was calculated from simulated data and shown to also align

well with the heteroclinic orbit. Overall, consistent results were obtained for the location of the separatrix using all methods.

In this biological example, the LCS forms the boundary of a basin of stability. Defining the basin of stability in state space provides a much richer understanding of the system dynamics over previous methods that calculate a single scalar value. The boundary, or recovery envelope, could be used in conjunction with sway data to define new measures of individual fall risk, e.g., the average distance of an individual's state from the boundary.

It is noted that the state-space-averaged FTLE for any time T can be obtained by computing the average of the FTLE field over the sampled region of state space. This provides the link between the current method and previous methods for finding an averaged Lyapunov exponent from time series data. In forthcoming work, this method will be demonstrated on higher dimensional data and actual experimental data. In general, it is believed the method demonstrated in this study provides a fruitful approach for extracting additional information from noisy experimental data, namely boundaries between qualitatively different kinds of motion.

4.6 Acknowledgments

The author would like to express his gratitude to Dr. Kevin P. Granata for his contributions and guidance during the early portions of this research. Tragically, Dr. Granata was killed in the April 16th shootings at Virginia Tech. Although he left this world far too early, his visionary spirit has guided the author throughout this research.

Chapter 5

Mathematical Modeling and Simulation of the Planar Wobble Chair

5.1 Abstract

Various unstable seat apparatus have been used to isolate motion of the lumbar spine in order to quantify torso stability, a factor associated with low back pain. A mathematical model of a human sitting on one such apparatus, the wobble chair, was developed. Motion was restricted to the sagittal plane and anthropometric data was used for model calibration. Numerical simulations were conducted to find trajectories which were evaluated to determine finite time Lyapunov exponents (FTLE) from each initial location in state space. The FTLE field was used to find Lagrangian coherent structures, ridges in the FTLE field, in order to determine the location of the basin of stability. Both deterministic and stochastic simulations were performed. The dynamics depend strongly on the control algorithm of the subject and finding a stable controller was a significant portion of this investigation. The wobble chair is an apparatus used to isolate certain features of the control germane to torso stability.

5.2 Introduction

Spinal stability is often associated with low back pain (Bergmark 1989; Granata and Orishimo 2001; McGill 2001; Van Dieen et al. 2003; Brown and McGill 2005; Reeves et al. 2007b). Since usual engineering methods sacrifice the test sample during stability testing, these are not suitable for application to human subjects. An unstable seat apparatus has been used to isolate motion of the lumbar spine in order to quantify torso stability (Cholewicki et al. 2000; Reeves et al. 2006; Tanaka and Granata 2007; Granata and Lee 2008). Kinematic variability methods such as RMS distance, ellipse area, and path velocity (Granata and Lee 2008) as well as dynamic stability methods such as stability diffusion (Cholewicki et al. 2000) and Lyapunov stability (Tanaka and Granata 2007; Granata and Lee 2008) have been used to quantify the system dynamics. In addition to analysis of experimental data, a mathematical model can be a useful tool to gain better insight into the underlying system dynamics. Often, underlying dynamics that are not readily apparent through observation may be detected through simulations. In addition, simulations may be performed to show system behavior under controlled conditions that may not be possible in highly coupled systems.

In this chapter, simulations of torso stability will be conducted on the planar model of the wobble chair (Figure 2.1). The planar wobble chair model is a highly nonlinear system that exhibits complex behavior due to strong coupling between the two segments. In order to gain a better understanding of the system behavior, a similar dynamic system, the "Acrobot", will first be evaluated. The Acrobot consists of a double inverted pendulum with actuation on the joint between the segments and no actuation at the attachment point. It has been studied by multiple

researchers for almost 20 years, with a moderate amount of published work on this system. Since the Acrobot is a diffeomorphism of the wobble chair, some of the same properties exhibited by the Acrobot are also present in the wobble chair (Note: Two systems which are diffeomorphisms share the same dynamics and one system can be morphed into the other). After solving for this simpler system, the model configuration will be morphed into the wobble chair to reveal the solution to this more complex system of interest.

5.2.1 History and properties of the Acrobot

The Acrobot consists of a double inverted pendulum with an actuator between the two segments and no actuator at the pin joint where the Acrobot attaches to the inertial reference frame (Figure 5.1). Since the Acrobot model is a diffeomorphism of the wobble chair model, the differential equations developed for the wobble chair also apply to the Acrobot. The only differences are in the parameter values (i.e. masses, moments of inertia, vector direction and magnitude to the joint, and vector directions and magnitudes to the center of mass). It is advantageous to study this slightly simpler and more well-known system in order to gain a better understanding of the results that may be obtained from the wobble chair.

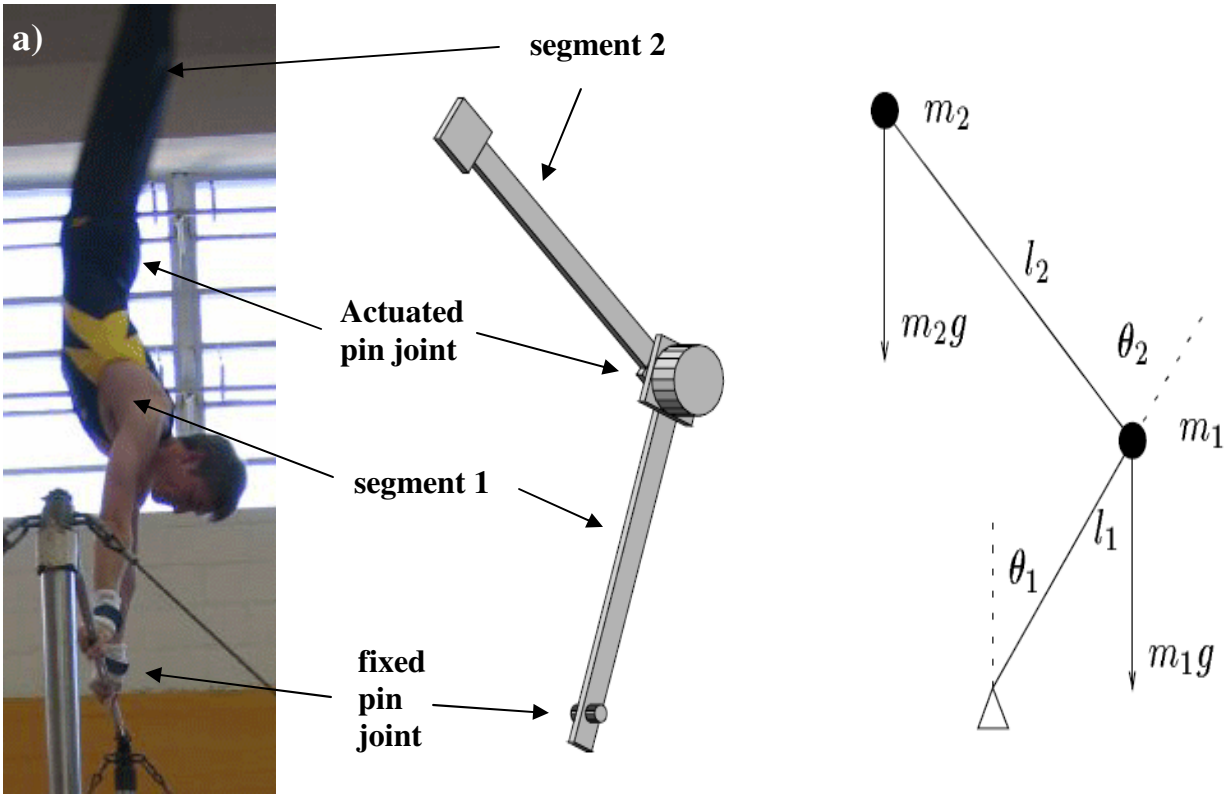

Figure 5.1: The Acrobot (acrobatic robot) is patterned after a gymnast on a high bar (a). Actuation occurs only at the middle joint (hip) with the first joint (hands) being free to spin about its axis (Murray and Hauser 1991)

Both the Acrobot and wobble chair are underactuated systems, meaning they posses fewer actuations directions than degrees of freedom (Spong 1995). Murray and Hauser coined the term "Acrobot" and were the first to show that this underactuated system was controllable at any equilibrium point .(Hauser and Murray 1990). Controllability in this case denotes the ability to move the segments within configuration space and near an equilibrium point using only the single actuator. Since then, others have evaluated the dynamics of the Acrobot (Spong 1995; Boone 1997) and similar dynamic systems (Hou and Luecke 2003). The Acrobot is highly nonlinear with strong coupling between segments. This coupling was used by Spong to achieve a linear response from the first segment through momentum coupling with the second segment.

This resulted in exponential convergence of segment one. However, the movement of segment two was complex since its motion was dictated by the dynamics required to generate the coupling forces needed to control segment one (Spong 1995). Thus, segment two could not be controlled for exponential convergence simultaneously with segment one.

One important property of the Acrobot is the existence of an equilibrium manifold (Murray and Hauser 1991). The manifold exists when the combined center of mass of the two segments lies directly above the free swinging pin joint. With an appropriate torque at the middle joint, this configuration is able to achieve static equilibrium where the two angles, θ_1 and θ_2, are static. One way to fix the angle is to apply an appropriate torque at the joint between the segments. In the examples below, the equilibrium manifold was generated for two sets of parameter values, the balanced parameters and the actual system parameters (Figure 5.2).

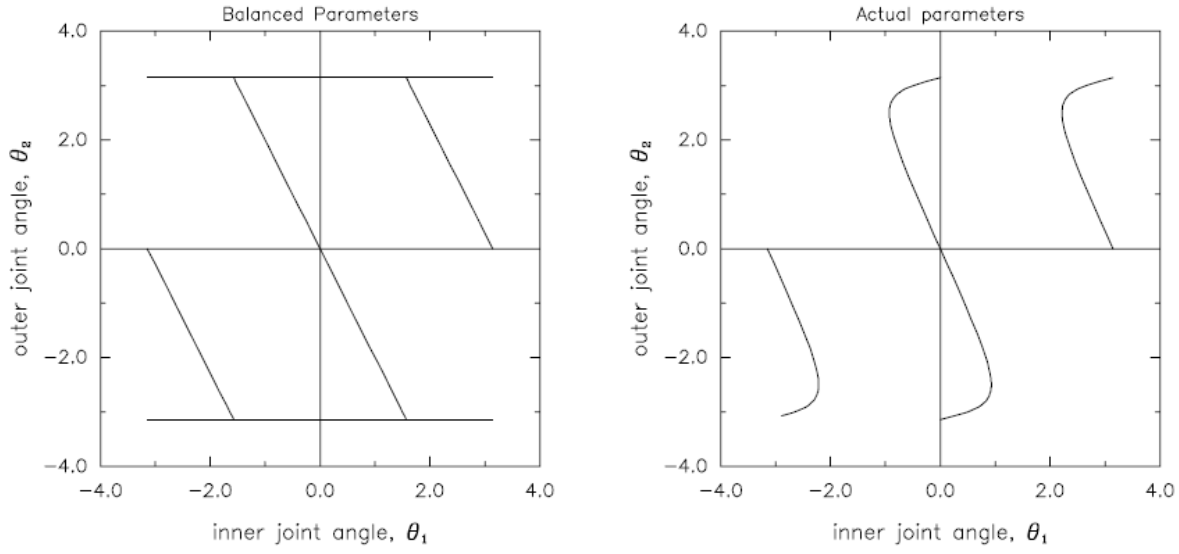

Figure 5.2: Equilibrium manifold for the Acrobot. Balanced parameter values were 0.5, 1, 8, 8, and 10 for the length of segment 1, length of segment 2, mass of segment 1, mass of segment 2, and acceleration of gravity, respectively. Actual parameters were 0.5, 0.75, 7, 8, and 9.8 respectively (Murray and Hauser 1991).

Bortoff, a student of Spong, was the first to produce experimental results for the Acrobot (Bortoff 1992) (Figure 5.3). Quantitatively, the results differed from Murray and Hauser for two reasons. First, the systems had different parameter values: masses, lengths, moments of inertia, friction and damping. Second, Murray and Hauser defined the second joint angle as the angle between the two segments, and Bortoff defined the second angle from the vertical reference. However, despite these differences, the results are qualitatively similar. The existence of an equilibrium manifold is significant because it indicates that there are an infinite number of equilibrium points which exists along the length of the manifold. Thus, stability for the Acrobot (and the wobble chair) may be achieved with more than one combination of θ_1 and θ_2.

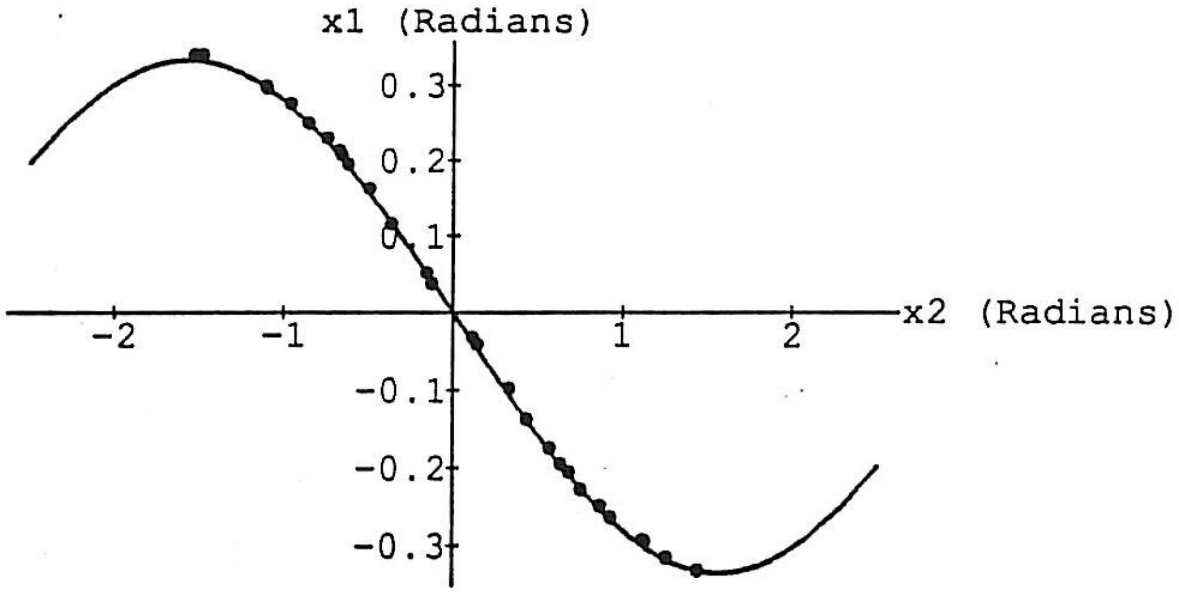

Figure 5.3: Equilibrium manifold for the physical Acrobot (Bortoff 1992). Note that the axes are switched when compared with Figure 5.2.

A second property of the Acrobot is the location of the basin of stability. The basin of stability for the balanced system was found to be a diagonal band around the vertical position when plotted in (θ_1,θ_2) variables for both segments at zero velocity (Figure 5.4a)(Murray and Hauser 1991). Although not shown, it is presumed that the basin of stability is centered over the equilibrium manifold. Bortoff also found a basin of stability for the Acrobot with linear control (Figure 5.4b) (Bortoff 1992). The solid line encircles a basin of stability for a controller which has been linearized about the origin. The dashed line encircles the basin of stability for a controller that is linearized about a balanced configuration in which the second segment is horizontal. Three important conclusions may be made from the basins of stability. First, the basins of stability are generally, but not exactly, aligned with the equilibrium manifold. Second, the size of the basin of stability becomes smaller when the system is linearized about a point further from the vertical configuration (the origin). Third, stability may be achieved further from the origin by using a controller that is linearized about a remote point on the equilibrium manifold near the state of the system.

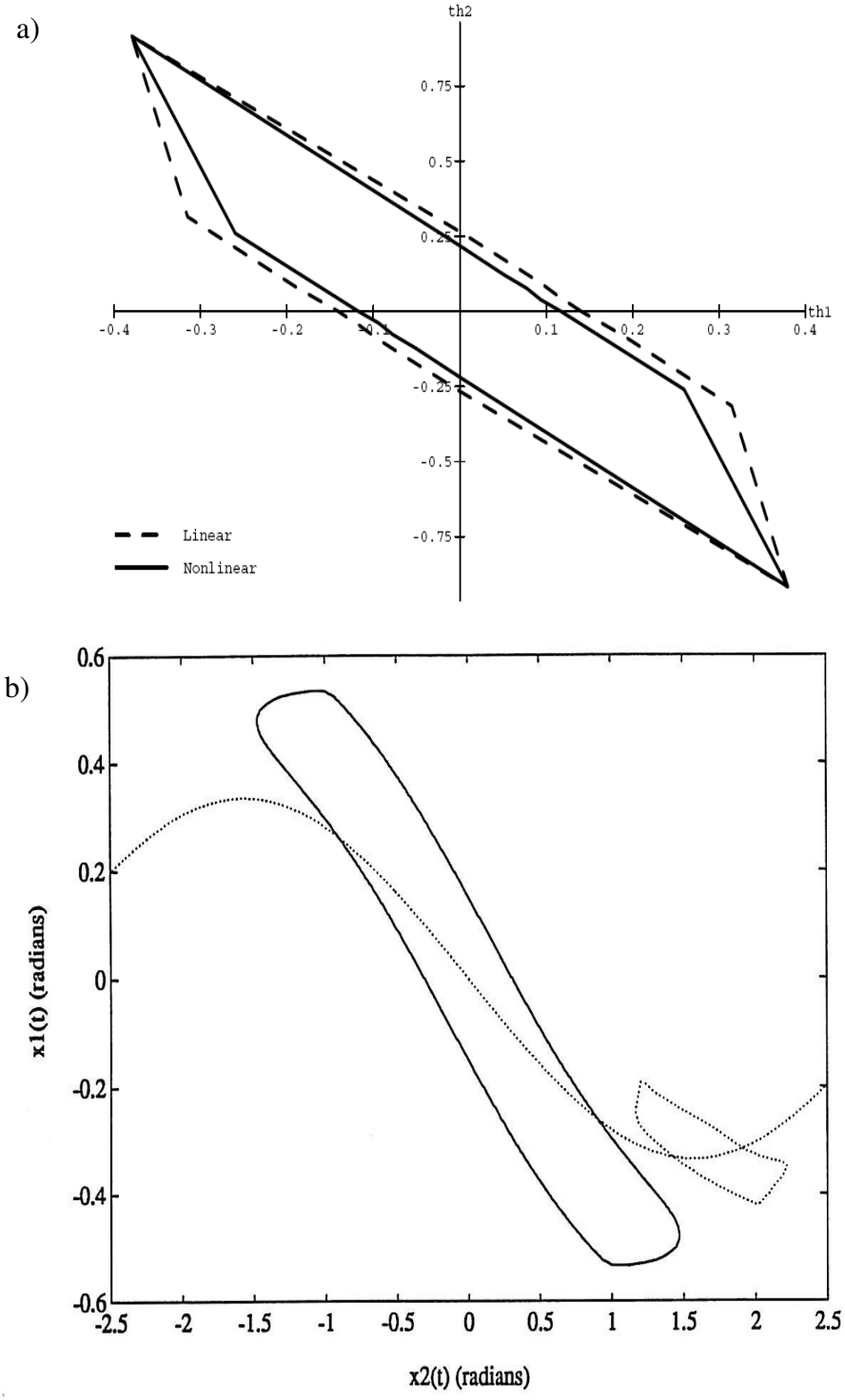

Figure 5.4: Basin of stability for (a) the balanced Acrobot (Murray and Hauser 1991) and (b) the physical Acrobot (Bortoff 1992).

5.2.2 Morphing the Acrobot into the Wobble Chair

The FTLE field (see section 4.2.3) for the wobble chair was generated by slowly morphing the Acrobot into the wobble chair. Controller gains were modified during the progression to ensure that LCS could still be seen at each step of the transformation. First, keeping all other parameters the same, the masses were increased from the Acrobot values to the wobble chair values ($m_1 = 8 \rightarrow 27.4$ kg ; $m_2 = 8 \rightarrow 31.8$ kg). Next, the moments of inertia were changed ($I_1 = 0 \rightarrow 2.35$ kg·m^2 ; $I_2 = 0 \rightarrow 4.86$ kg·m^2). Next the segment and center of mass vectors were slowly changed. The vectors for the Acrobot and wobble chair are shown in Table 5.1. In order to morph all vectors simultaneously, a morphing percent, *morph*, was defined. Each vector was *morph* percent Acrobot and (100- *morph*) percent wobble chair. Some of the intermediate configurations are shown in Figure 5.5.

Table 5.1: Segment and center of mass vectors

	Wobble chair			Acrobot		
	x	y	z	x	y	z
L_1	0.1272	0.1580	0	0	0.5	0
L_2	0	0.7179	0	0	0.5	0
c_1	-0.1771	0.0780	0	0	1.0	0
c_2	0	0.2736	0	0	1.0	0

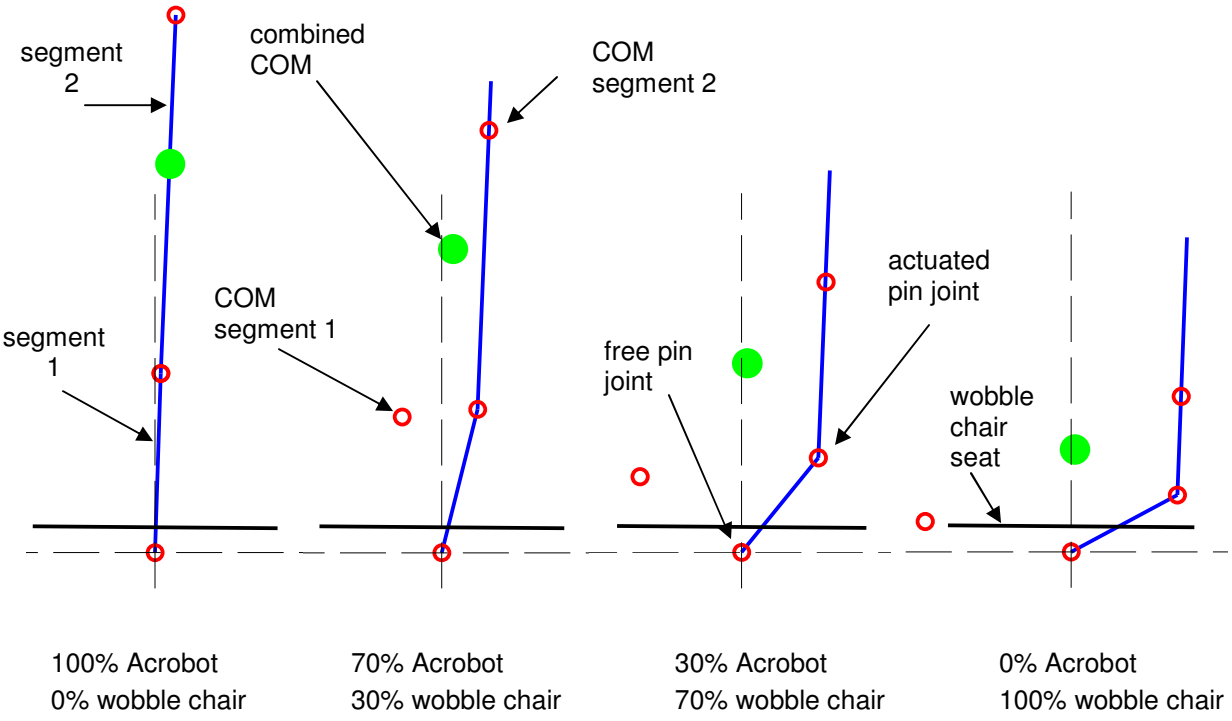

Figure 5.5: Center of mass and segment vectors for the Acrobot were slowly changed to those of the wobble chair. This effectively morphed one model into the other.

5.3 Mathematical Model of the Planar Wobble Chair

The planar wobble chair was modeled as a double inverted pendulum. In the wobble chair, the first segment consisted of the lower body and the chair. The second segment consisted of the head, arms, and torso. The pivot joint between the two segments was located between the fourth and fifth lumbar vertebrae (Van Dieen et al. 2003).

5.3.1 Anthropometric Parameters

A segmented human model (Figure 5.6) was created so that the location of the center of mass (COM) for each segment and the joint location between the two segments could be calculated.

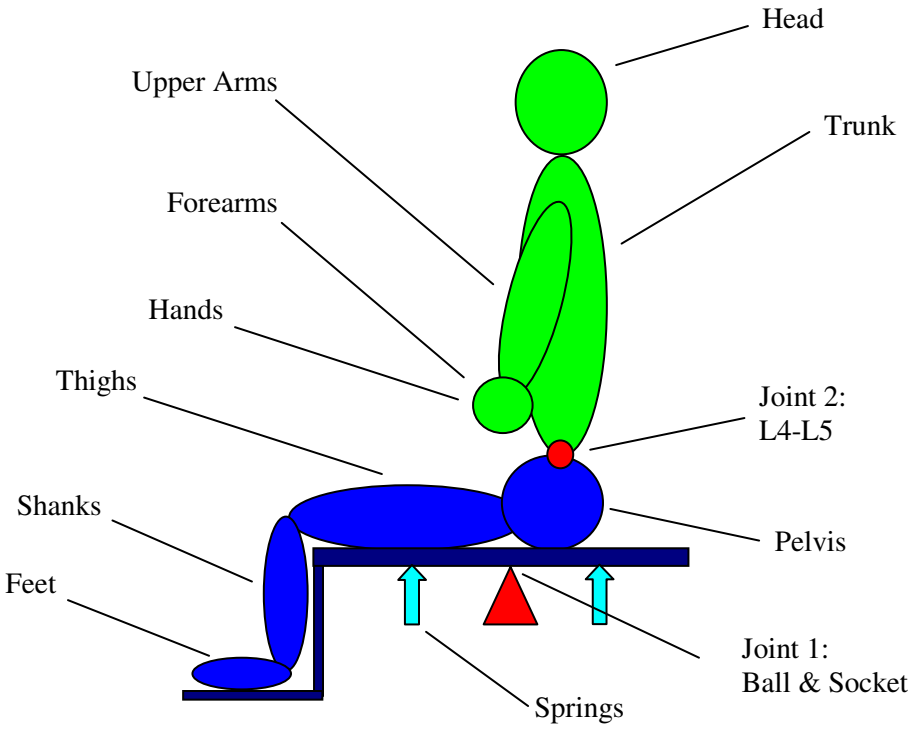

Figure 5.6: Model of the person sitting on the wobble chair. Blue components contribute to segment one. Green components make up segment 2. The joints are shown in red and the springs in aqua.

Individual body segments were modeled using anthropometric data (de Leva 1996). Anthropometric parameters used in the model included segment masses, COM locations, and radiuses of gyration for a typical person. Segment values were obtained by multiplying the given ratios by the subject's height or weight. Using the anthropometric data and human subject measurements the following three dimensional vectors were generated from components of the lower body while configured in the seated position (Table 5.2 and Figure 5.7).

Table 5.2: Lower body vector table

	Beginning location	**Ending location**	**Source**
$\mathbf{r}_{oh}$	Origin (ball joint)	Hip (greater trochanter)	Measurements
$\mathbf{r}_{hCOMt}$	Hip	COM of the thigh	Anthropometric
$\mathbf{r}_{ot}$	Origin	COM of the thigh	$\mathbf{r}_{ot} = \mathbf{r}_{oh} + \mathbf{r}_{hCOMt}$
$\mathbf{r}_{hk}$	Hip	Knee	Anthropometric
$\mathbf{r}_{kCOMs}$	Knee	COM of the shank	Anthropometric
$\mathbf{r}_{os}$	Origin	COM of the shank	$\mathbf{r}_{os} = \mathbf{r}_{oh} + \mathbf{r}_{hk} + \mathbf{r}_{kCOMs}$
$\mathbf{r}_{ka}$	Knee	Ankle	Anthropometric
$\mathbf{r}_{aCOMf}$	Ankle	COM of the foot	Anthropometric
$\mathbf{r}_{of}$	Origin	COM of the foot	$\mathbf{r}_{os} = \mathbf{r}_{oh} + \mathbf{r}_{hk} + \mathbf{r}_{ka} + \mathbf{r}_{aCOMf}$

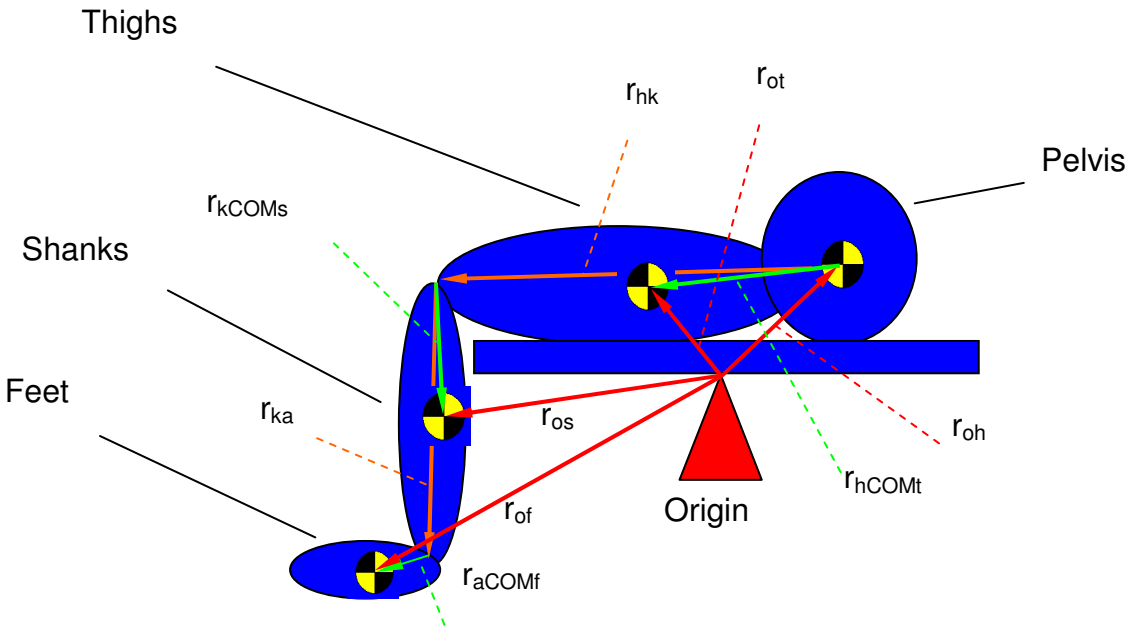

Figure 5.7: Vectors were used to find the locations of the center of mass of each body segment.

The mass of each component was found from tabulated data. The radius of gyration for each segment was used to determine the moment of inertia for each component about its center of mass.

$$I_{jj\_i} = m_i g^2_{jj\_i} \qquad j = x, y \qquad i = h, t, s, f \tag{5.1}$$

Where, i represents the component (hip, thigh, shank, foot) and j corresponds to the axis. The parallel axis theorem was applied to obtain the moment of inertia of each component about the origin.

$$I_{jjo\_i} = I_{jj\_i} + m_i\left(r^2_{oi}\right) \qquad j = x, y \qquad i = h, t, s, f \tag{5.2}$$

All components were combined to develop a composite moment of inertia for the lower body, $I^{(1)}$.

$$I^{(1)}_{jj} = I_{jj\_pv} + 2I_{jj\_t} + 2I_{jj\_s} + 2I_{jj\_f} \qquad j = x, y \tag{5.3}$$

The mass of the lower body, m_1, was determined by calculating the sum of the component masses. The vector from the origin to the center of mass of the lower body was found as follows:

$$\vec{c}_1 = \frac{\vec{r}_{oh}m_h + 2\vec{r}_{ot}m_t + 2\vec{r}_{os}m_s + 2\vec{r}_{of}m_f}{m_h + 2m_t + 2m_s + 2m_f} \tag{5.4}$$

The upper body was calculated in a similar manner. Upper body components consisted of the head, torso, two upper arms, two forearms, and two hands. The upper body mass, m_2, was determined by evaluating the sum of the component masses. The center of mass of the upper body, $\bar{c}_2$, was calculated with the same techniques used to calculate $\bar{c}_1$ above.

A reduced model was developed for the body, simplifying it into two rigid segments pivoted at the joint between the fourth and fifth lumbar vertebrae, L4 and L5 (Figure 5.8). $\bar{L}_1$ and $\bar{L}_2$ are the segment vectors of the reduced model. Notice that if the vectors $\bar{c}_1$ equal $\bar{L}_1$ and $\bar{c}_2$ equals $\bar{L}_2$, then the wobble chair and Acrobot converge to the same system.

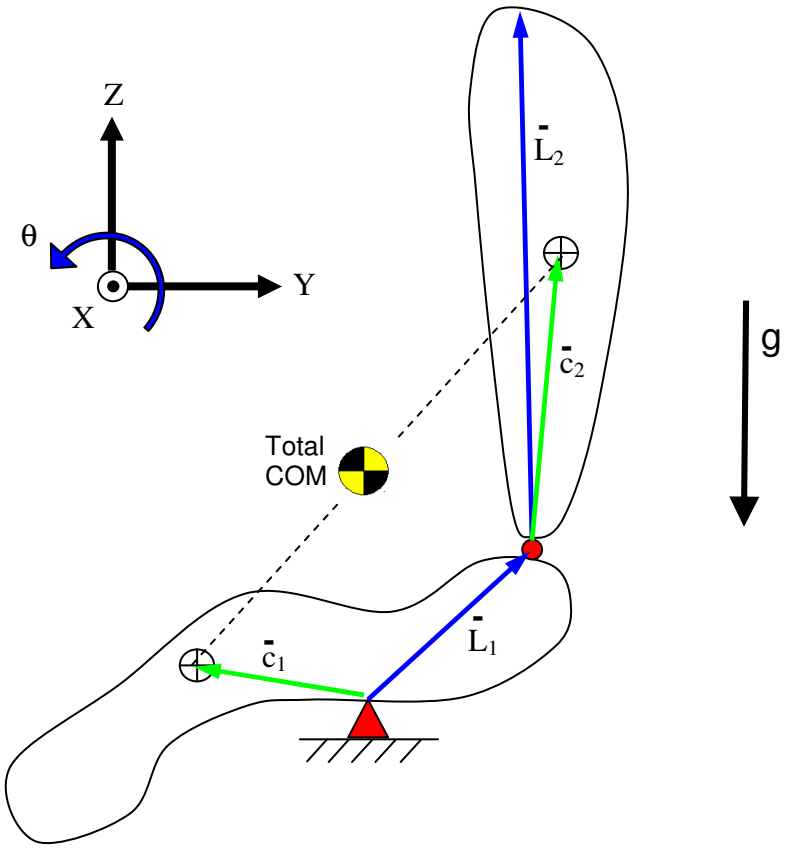

Figure 5.8 – Simplified model of the person sitting on the wobble chair. Position vectors, $\bar{L}_1$ and $\bar{L}_2$, show the connectivity of the model. Vectors $\bar{c}_1$ and $\bar{c}_2$ are from the joint to the center of mass of each segment. In the initial balanced configuration shown, the segment angles $\theta_1$and θ_2 are set to zero.

5.3.2 Planar Wobble Chair Model

A proportional-derivative (PD) controller was used to maintain stability. However, only one actuator between the two segments was included. This was used to represent flexion or extension of the spine in the lumbar region. No control torque was applied between the base and the chair to simulate the presence of the ball joint. In addition, compression springs were included in the model to provide a stabilizing torque. Stabilizing control was achieved by

causing flexion between the two joints when the overall center of mass is to the right of equilibrium and extension when the overall center of mass is to the left of equilibrium.

A Lagrangian approach was used to determine the equations of motion. The vectors $\bar{c}_1$, $\bar{c}_2$, $\bar{L}_1$ and $\bar{L}_2$ are position vectors that move with the local reference frame and are defined in the global reference frame when the system is in equilibrium. The vector from the ball joint to the center of mass of the lower body segment is $\bar{c}_1$. The vector from the ball joint to the hinge joint at the lumbar spine is $\bar{L}_1$. The vector, $\bar{c}_2$, is from the hinge joint at the spine to the center of mass of the upper body segment. The vector from the hinge joint at the spine to the center of mass of the head is $\bar{L}_2$

$$\vec{c}_1 = \begin{bmatrix} c_{1\_x} \\ c_{1\_y} \\ 0 \end{bmatrix} \quad \vec{L}_1 = \begin{bmatrix} L_{1\_x} \\ L_{1\_y} \\ 0 \end{bmatrix} \quad \vec{c}_2 = \begin{bmatrix} c_{2\_x} \\ c_{2\_y} \\ 0 \end{bmatrix} \quad \vec{L}_2 = \begin{bmatrix} L_{2\_x} \\ L_{2\_y} \\ 0 \end{bmatrix} \quad \vec{g} = \begin{bmatrix} 0 \\ -g \\ 0 \end{bmatrix} \qquad (5.5)$$

where, c_{1_x} and c_{1_y} are vector components in the local reference frame in the x and y directions respectively. The other terms were defined in a similar manner. The acceleration of gravity vector is given by $\bar{g}$ and is expressed in terms of the scalar value of g equal to 9.8 m/s^2. Rotations in the x-y plane are defined by angles θ_1 and θ_2 with the index defining the segment number. Rotations about the z-axis from local to global coordinates are given by the rotation matrices, $R_{\theta 1}$ and $R_{\theta 2}$.

$$R_{\theta 1} = \begin{bmatrix} Cos\theta_1 & -Sin\theta_1 & 0 \\ Sin\theta_1 & Cos\theta_1 & 0 \\ 0 & 0 & 1 \end{bmatrix} \quad R_{\theta 2} = \begin{bmatrix} Cos\theta_2 & -Sin\theta_2 & 0 \\ Sin\theta_2 & Cos\theta_2 & 0 \\ 0 & 0 & 1 \end{bmatrix} \qquad (5.6)$$

The position vectors in global coordinates were calculated by applying the rotation transformations to the position vector in local coordinates.

$$\begin{aligned} \vec{x}_{c1} &= R_{\theta 1}\vec{c}_1 & \vec{x}_{L1} &= R_{\theta 1}\vec{L}_1 \\ \vec{x}_{c2} &= R_{\theta 1}\vec{L}_1 + R_{\theta 2}\vec{c}_2 & \vec{x}_{L1} &= R_{\theta 1}\vec{L}_1 + R_{\theta 2}\vec{L}_2 \end{aligned} \tag{5.7}$$

The velocity vectors were found by taking the time derivative of the position vectors.

$$\begin{aligned} \dot{\vec{x}}_{c1} &= R'_{\theta 1}\dot{\theta}_1\vec{c}_1 & \dot{\vec{x}}_{L1} &= R'_{\theta 1}\dot{\theta}_1\vec{L}_1 \\ \dot{\vec{x}}_{c2} &= \frac{d}{dt}\left(R_{\theta 1}\vec{L}_1 + R_{\theta 2}\vec{c}_2\right) = R'_{\theta 1}\dot{\theta}_1\vec{L}_1 + R'_{\theta 2}\dot{\theta}_2\vec{c}_2 \\ \dot{\vec{x}}_{L2} &= \frac{d}{dt}\left(R_{\theta 1}\vec{L}_1 + R_{\theta 2}\vec{L}_2\right) = R'_{\theta 1}\dot{\theta}_1\vec{L}_1 + R'_{\theta 2}\dot{\theta}_2\vec{L}_2 \end{aligned} \tag{5.8}$$

The potential energy, V, is a function of the height of the masses in the gravitational field and given by,

$$\begin{aligned} V &= m_1\vec{g}\cdot\vec{x}_{c1} + m_2\vec{g}\cdot\vec{x}_{c2} \\ &= m_1\vec{g}\cdot\left(R_{\theta 1}\vec{c}_1\right) + m_2\vec{g}\cdot\left(R_{\theta 1}\vec{L}_1 + R_{\theta 2}\vec{c}_2\right) \end{aligned} \tag{5.9}$$

The kinetic energy, T, is a function of the velocities of the centers of mass and the angular velocities of the rigid bodies.

$$\begin{aligned} T &= \tfrac{1}{2}m_1\dot{\vec{x}}_{c1}\cdot\dot{\vec{x}}_{c1} + \tfrac{1}{2}m_2\dot{\vec{x}}_{c2}\cdot\dot{\vec{x}}_{c2} + \tfrac{1}{2}\omega_1\cdot I_1\cdot\omega_1 + \tfrac{1}{2}\omega_2\cdot I_2\cdot\omega_2 \\ &= \tfrac{1}{2}m_1\left(R'_{\theta 1}\dot{\theta}_1\vec{c}_1\right)\cdot\left(R'_{\theta 1}\dot{\theta}_1\vec{c}_1\right) \\ &\quad + \tfrac{1}{2}m_2\left(R'_{\theta 1}\dot{\theta}_1\vec{L}_1 + R'_{\theta 2}\dot{\theta}_2\vec{c}_2\right)\cdot\left(R'_{\theta 1}\dot{\theta}_1\vec{L}_1 + R'_{\theta 2}\dot{\theta}_2\vec{c}_2\right) \\ &\quad + \tfrac{1}{2}\dot{\theta}_1\cdot I_1\cdot\dot{\theta}_1 + \tfrac{1}{2}\dot{\theta}_2\cdot I_2\cdot\dot{\theta}_2 \\ &= \tfrac{1}{2}m_1\left\|\vec{c}_1\right\|^2\dot{\theta}_1^2 + \tfrac{1}{2}m_2\left\|\vec{L}_1\right\|^2\dot{\theta}_1^2 + m_2\left(R'_{\theta 1}\vec{L}_1\right)\cdot\left(R'_{\theta 2}\vec{c}_2\right)\dot{\theta}_1\dot{\theta}_2 \\ &\quad + \tfrac{1}{2}m_2\left\|\vec{c}_2\right\|^2\dot{\theta}_2^2 + \tfrac{1}{2}I_1\dot{\theta}_1^2 + \tfrac{1}{2}I_2\dot{\theta}_2^2 \end{aligned} \tag{5.10}$$

The Lagrangian, L, is given by the difference in kinetic energy, T, and potential energy, V. Lagrange's equations were applied to find the equations of motion.

$$\frac{d}{dt}\left(\frac{\partial L}{\partial \dot{\theta}}\right) - \frac{\partial L}{\partial \theta} = \tau \qquad L = T - V$$
$$\frac{d}{dt}\left(\frac{\partial (T - V)}{\partial \dot{\theta}}\right) - \frac{\partial (T - V)}{\partial \theta} = \tau \tag{5.11}$$
$$\frac{d}{dt}\left(\frac{\partial T}{\partial \dot{\theta}}\right) - \frac{d}{dt}\left(\frac{\partial V}{\partial \dot{\theta}}\right) - \frac{\partial T}{\partial \theta} + \frac{\partial V}{\partial \theta} = \tau$$

Where, τ is the sum of all torques applied to the system. The equation was solved for each component

$$\frac{\partial V}{\partial \theta_1} = m_1 \vec{g} \cdot \left(R'_{\theta 1} \vec{c}_1\right) + m_2 \vec{g} \cdot \left(R'_{\theta 1} \vec{L}_1\right)$$
$$\frac{\partial V}{\partial \theta_2} = m_2 \vec{g} \cdot \left(R'_{\theta 2} \vec{c}_2\right)$$

$$\frac{\partial V}{\partial \dot{\theta}_1} = 0 \qquad \frac{\partial V}{\partial \dot{\theta}_2} = 0$$

$$\frac{\partial T}{\partial \theta_1} = m_2 \left(R''_{\theta 1} \vec{L}_1\right) \cdot \left(R'_{\theta 2} \vec{c}_2\right) \dot{\theta}_1 \dot{\theta}_2 \tag{5.12}$$
$$\frac{\partial T}{\partial \theta_2} = m_2 \left(R'_{\theta 1} \vec{L}_1\right) \cdot \left(R''_{\theta 2} \vec{c}_2\right) \dot{\theta}_1 \dot{\theta}_2$$

$$\frac{\partial T}{\partial \dot{\theta}_1} = m_1 \left\|\vec{c}_1\right\|^2 \dot{\theta}_1 + m_2 \left\|\vec{L}_1\right\|^2 \dot{\theta}_1 + m_2 \left(R'_{\theta 1} \vec{L}_1\right) \cdot \left(R'_{\theta 2} \vec{c}_2\right) \dot{\theta}_2 + I_1 \dot{\theta}_1$$
$$\frac{\partial T}{\partial \dot{\theta}_2} = m_2 \left(R'_{\theta 1} \vec{L}_1\right) \cdot \left(R'_{\theta 2} \vec{c}_2\right) \dot{\theta}_1 + m_2 \left\|\vec{c}_2\right\|^2 \dot{\theta}_2 + I_2 \dot{\theta}_2$$

$$\frac{d}{dt}\left(\frac{\partial T}{\partial \dot{\theta}_1}\right) = m_1 \left\|\vec{c}_1\right\|^2 \ddot{\theta}_1 + m_2 \left\|\vec{L}_1\right\|^2 \ddot{\theta}_1 + m_2 \left(R''_{\theta 1} \vec{L}_1\right) \cdot \left(R'_{\theta 2} \vec{c}_2\right) \dot{\theta}_1 \dot{\theta}_2$$
$$+ m_2 \left(R'_{\theta 1} \vec{L}_1\right) \cdot \left(R''_{\theta 2} \vec{c}_2\right) \dot{\theta}_2^2 + m_2 \left(R'_{\theta 1} \vec{L}_1\right) \cdot \left(R'_{\theta 2} \vec{c}_2\right) \ddot{\theta}_2 + I_1 \ddot{\theta}_1$$

$$\frac{d}{dt}\left(\frac{\partial T}{\partial \dot{\theta}_2}\right) = m_2\left(R''_{\theta 1}\vec{L}_1\right)\cdot\left(R'_{\theta 2}\vec{c}_2\right)\dot{\theta}_1^2 + m_2\left(R'_{\theta 1}\vec{L}_1\right)\cdot\left(R''_{\theta 2}\vec{c}_2\right)\dot{\theta}_1\dot{\theta}_2$$
$$+ m_2\left(R'_{\theta 1}\vec{L}_1\right)\cdot\left(R'_{\theta 2}\vec{c}_2\right)\ddot{\theta}_1 + m_2\left\|\vec{c}_2\right\|^2\ddot{\theta}_2 + I_2\ddot{\theta}_2$$

Combining these equations yields the equations of motion,

$$\theta_1: \quad \frac{d}{dt}\left(\frac{\partial T}{\partial \dot{\theta}_1}\right) - \frac{d}{dt}\left(\frac{\partial V}{\partial \dot{\theta}_1}\right) - \frac{\partial T}{\partial \theta_1} + \frac{\partial V}{\partial \theta_1} = \tau_1$$

$$\begin{aligned}
&\left(\begin{array}{l} m_1\left\|\vec{c}_1\right\|^2\ddot{\theta}_1 + m_2\left\|\vec{L}_1\right\|^2\ddot{\theta}_1 + m_2\left(R''_{\theta 1}\vec{L}_1\right)\cdot\left(R'_{\theta 2}\vec{c}_2\right)\dot{\theta}_1\dot{\theta}_2 \\ + m_2\left(R'_{\theta 1}\vec{L}_1\right)\cdot\left(R''_{\theta 2}\vec{c}_2\right)\dot{\theta}_2^2 + m_2\left(R'_{\theta 1}\vec{L}_1\right)\cdot\left(R'_{\theta 2}\vec{c}_2\right)\ddot{\theta}_2 + I_1\ddot{\theta}_1 \end{array}\right) \\
&- (0) - \left(m_2\left(R''_{\theta 1}\vec{L}_1\right)\cdot\left(R'_{\theta 2}\vec{c}_2\right)\dot{\theta}_1\dot{\theta}_2\right) \\
&+ \left(m_1\vec{g}\cdot\left(R'_{\theta 1}\vec{c}_1\right) + m_2\vec{g}\cdot\left(R'_{\theta 1}\vec{L}_1\right)\right) = \tau_1
\end{aligned}$$

$$\begin{aligned}
&m_1\left\|\vec{c}_1\right\|^2\ddot{\theta}_1 + m_2\left\|\vec{L}_1\right\|^2\ddot{\theta}_1 + m_2\left(R'_{\theta 1}\vec{L}_1\right)\cdot\left(R''_{\theta 2}\vec{c}_2\right)\dot{\theta}_2^2 \\
&+ m_2\left(R'_{\theta 1}\vec{L}_1\right)\cdot\left(R'_{\theta 2}\vec{c}_2\right)\ddot{\theta}_2 + I_1\ddot{\theta}_1 + m_1\vec{g}\cdot\left(R'_{\theta 1}\vec{c}_1\right) \\
&+ m_2\vec{g}\cdot\left(R'_{\theta 1}\vec{L}_1\right) = \tau_1
\end{aligned} \tag{5.13}$$

$$\theta_2: \quad \frac{d}{dt}\left(\frac{\partial T}{\partial \dot{\theta}_2}\right) - \frac{d}{dt}\left(\frac{\partial V}{\partial \dot{\theta}_2}\right) - \frac{\partial T}{\partial \theta_2} + \frac{\partial V}{\partial \theta_2} = \tau_2$$

$$\begin{aligned}
&\left(\begin{array}{l} m_2\left(R''_{\theta 1}\vec{L}_1\right)\cdot\left(R'_{\theta 2}\vec{c}_2\right)\dot{\theta}_1^2 + m_2\left(R'_{\theta 1}\vec{L}_1\right)\cdot\left(R''_{\theta 2}\vec{c}_2\right)\dot{\theta}_1\dot{\theta}_2 \\ + m_2\left(R'_{\theta 1}\vec{L}_1\right)\cdot\left(R'_{\theta 2}\vec{c}_2\right)\ddot{\theta}_1 + m_2\left\|\vec{c}_2\right\|^2\ddot{\theta}_2 + I_2\ddot{\theta}_2 \end{array}\right) - (0) \\
&- \left(m_2\left(R'_{\theta 1}\vec{L}_1\right)\cdot\left(R''_{\theta 2}\vec{c}_2\right)\dot{\theta}_1\dot{\theta}_2\right) + \left(m_2\vec{g}\cdot\left(R'_{\theta 2}\vec{c}_2\right)\right) = \tau_2
\end{aligned}$$

$$\begin{aligned}
&m_2\left(R''_{\theta 1}\vec{L}_1\right)\cdot\left(R'_{\theta 2}\vec{c}_2\right)\dot{\theta}_1^2 + m_2\left(R'_{\theta 1}\vec{L}_1\right)\cdot\left(R'_{\theta 2}\vec{c}_2\right)\ddot{\theta}_1 \\
&+ m_2\left\|\vec{c}_2\right\|^2\ddot{\theta}_2 + I_2\ddot{\theta}_2 + m_2\vec{g}\cdot\left(R'_{\theta 2}\vec{c}_2\right) = \tau_2
\end{aligned} \tag{5.14}$$

These two equations were put into a matrix equation with the following form

$$M\ddot{\theta} + C\dot{\theta}^2 + G(\theta) = \tau \tag{5.15}$$

with the matrices defined below.

$$M = \begin{bmatrix} m_1\left\|\vec{c}_1\right\|^2 + m_2\left\|\vec{L}_1\right\|^2 + I_1 & m_2\left(R'_{\theta 1}\vec{L}_1\right)\cdot\left(R'_{\theta 2}\vec{c}_2\right) \\ m_2\left(R'_{\theta 1}\vec{L}_1\right)\cdot\left(R'_{\theta 2}\vec{c}_2\right) & m_2\left\|\vec{c}_2\right\|^2 + I_2 \end{bmatrix}$$

$$C = \begin{bmatrix} 0 & m_2\left(R'_{\theta 1}\vec{L}_1\right)\cdot\left(R''_{\theta 2}\vec{c}_2\right) \\ m_2\left(R''_{\theta 1}\vec{L}_1\right)\cdot\left(R'_{\theta 2}\vec{c}_2\right) & 0 \end{bmatrix}$$

$$G = \begin{bmatrix} m_1\vec{g}\cdot\left(R'_{\theta 1}\vec{c}_1\right) + m_2\vec{g}\cdot\left(R'_{\theta 1}\vec{L}_1\right) \\ m_2\vec{g}\cdot\left(R'_{\theta 2}\vec{c}_2\right) \end{bmatrix}$$

$$\tau = \begin{bmatrix} \tau_1 \\ \tau_2 \end{bmatrix}$$

$$\theta = \begin{bmatrix} \theta_1 \\ \theta_2 \end{bmatrix}$$

τ_1 and τ_2 are composed of multiple components as described below

$$\tau = \begin{bmatrix} T_{Spr} - \left(T_{sk} + T_{sd} + C_p + C_d + Noise\right) \\ T_{sk} + T_{sd} + C_p + C_d + Noise \end{bmatrix} \tag{5.16}$$

where, T_{Spr} is the spring torque as described above for the inverted pendulum model. C_p, C_d, and noise are also described above. T_{sk} is the torque due to stiffness of the spine, and T_{sd} is the torque due to damping of the spine.

5.4 Nonlinear Analysis

Nonlinear methods were used to simulate and analyze the Acrobot and the wobble chair models. First, the Matlab model of the Acrobot was simulated as a deterministic system. The results were compared to those found by other researchers. Next, the segment and center of mass

vectors were slowly morphed from the Acrobot values to the wobble chair values. A deterministic simulation was performed on this system and compared to the Acrobot. Next, a simulation was run with noise applied to the wobble chair and time series data was generated. Finally, a stochastic analysis was performed on the noisy time series data to find the location of the basin of stability.

One challenge with this analysis is that the basin of stability lies within the four dimensions of state space. Although one, two, and three dimensional geometries are relatively easy to understand, visualization in four our more dimensions is non-intuitive, and techniques must be used to evaluate the results. One method is to view a slice of a high dimensional system using a Poincaré sections. In the following analysis, three sections will be examined. In the first Poincaré section, the sensitivity to θ_1 and θ_2 will be evaluated while the angular velocity of θ_1 and θ_2 are near zero (Figure 5.9). Using set notation this Poincaré section is given by

$$\Sigma_0 = \left\{ (\theta_1, \theta_2) \in S^1 \times S^1 \,\middle|\, \dot{\theta}_1 \approx \dot{\theta}_1 \approx 0 \right\} \tag{5.17}$$

where S^1 is the configuration space of a circle. The second Poincaré section is a $(\theta_1, \dot{\theta}_1)$ slice of state space while the angle and angular velocity of θ_2 are near zero. Set notation this Poincaré section is given by

$$\Sigma_0 = \left\{ (\theta_1, \dot{\theta}_1) \in S^1 \times \Re \,\middle|\, \theta_2 \approx \dot{\theta}_2 \approx 0 \right\} \tag{5.18}$$

where $\Re$ is the set of all real numbers representing the tangent space of θ_1. The third Poincaré section is a $(\theta_2, \dot{\theta}_2)$ slice of state space, more precisely,

$$\Sigma_0 = \left\{ (\theta_2, \dot{\theta}_2) \in S^1 \times \Re \,\middle|\, \theta_1 \approx \dot{\theta}_1 \approx 0 \right\} \tag{5.19}$$

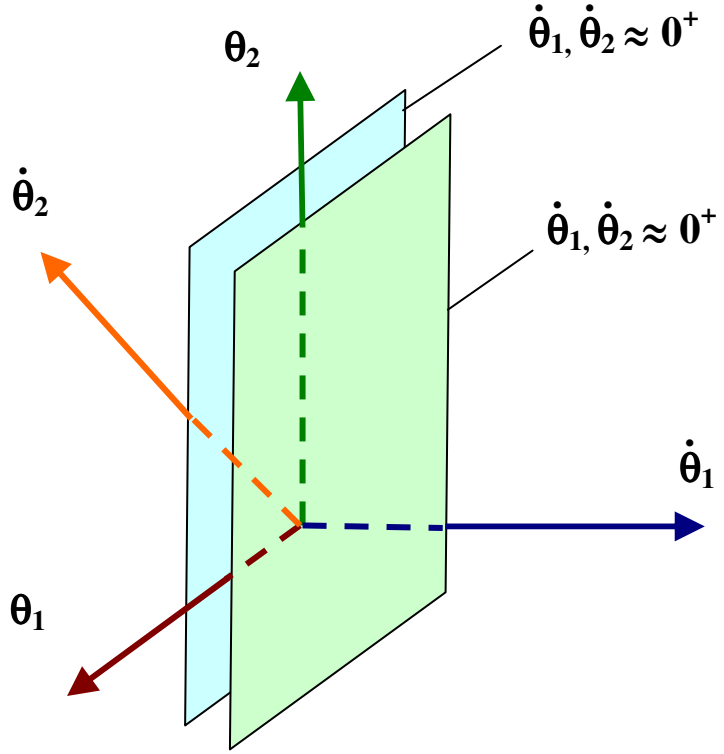

Figure 5.9: Poincaré section is a (θ_1, θ_2) slice of state space while the angular velocities $(\dot{\theta}_1, \dot{\theta}_2)$ are near zero.

5.4.1 Analysis of the Deterministic Acrobot

A mathematical model was developed with parameter values that matched the balanced system created by Murray and Hauser. Since the system is underactuated, both segments cannot be controlled. Therefore, a proportional-derivative (PD) controller was used to drive the location of the total center of mass to the equilibrium manifold. Empirical methods were used to determine the gain parameters needed to stabilize the Acrobot. The process of determining appropriate gains can be difficult in highly nonlinear and unstable systems. However, finding appropriate controller gains for the balanced parameter Acrobot was relatively simple when

compared to the wobble chair. These stable controller gains will be used as a starting point in trying to find stable gains for the wobble chair in the next section.

A simulation was conducted using a proportional gain of $9x10^3$ and a derivative gain of six. The controller was able to drive the total center of mass from an initial angle of 1 degree to within 0.1 degrees with what appears to be exponential convergence (Figure 5.10). Although the center of mass approached zero, the segments oscillated between ~ ± 5 degrees (Figure 5.11). The phase plot clearly shows that the system developed a limit cycle (Figure 5.12.)

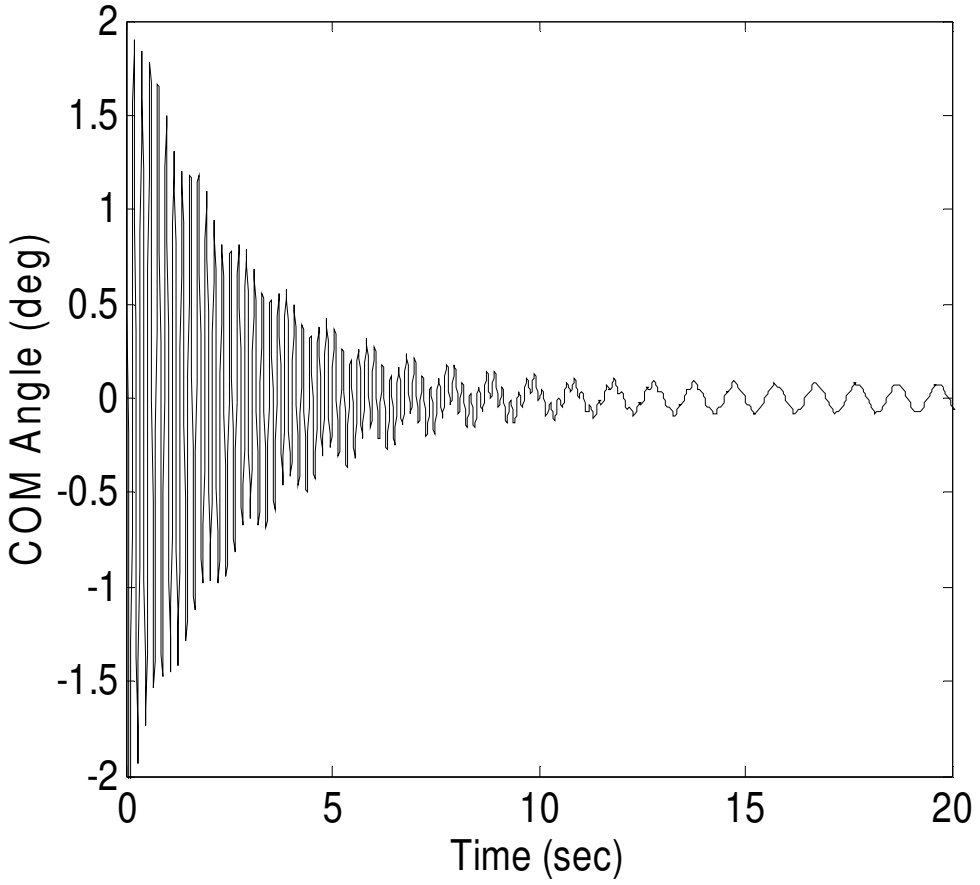

Figure 5.10: Simulation results showing that PD controller drove the center of mass to near the equilibrium manifold.

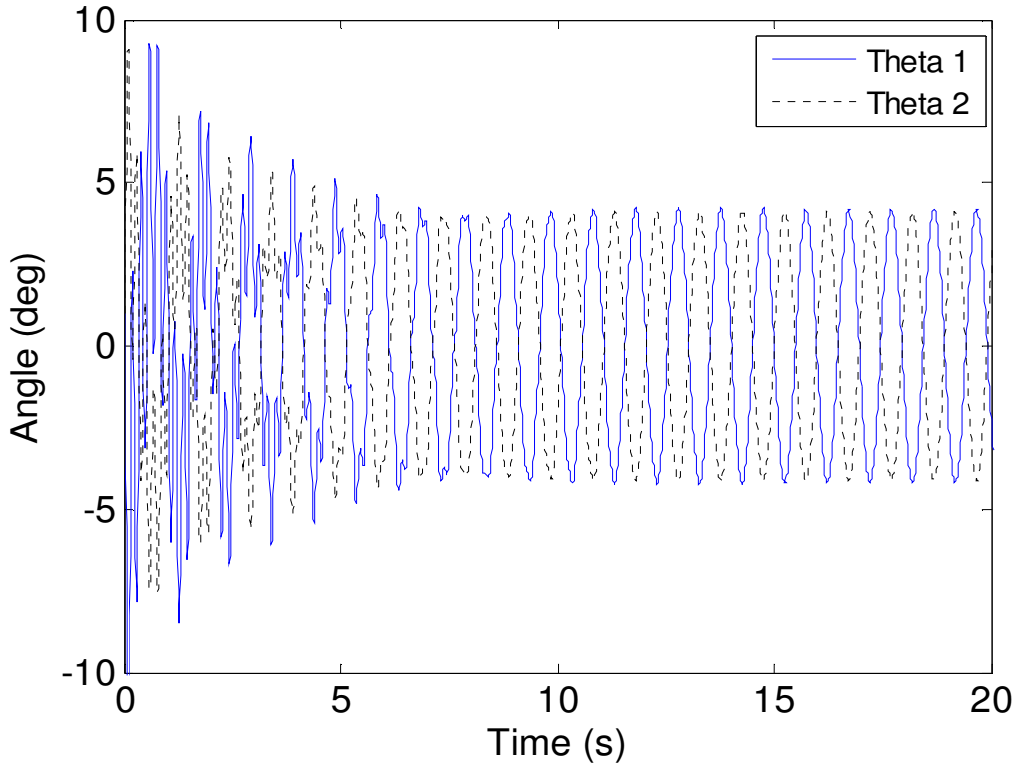

Figure 5.11: Time plot for the upper and lower segments of the Acrobot.

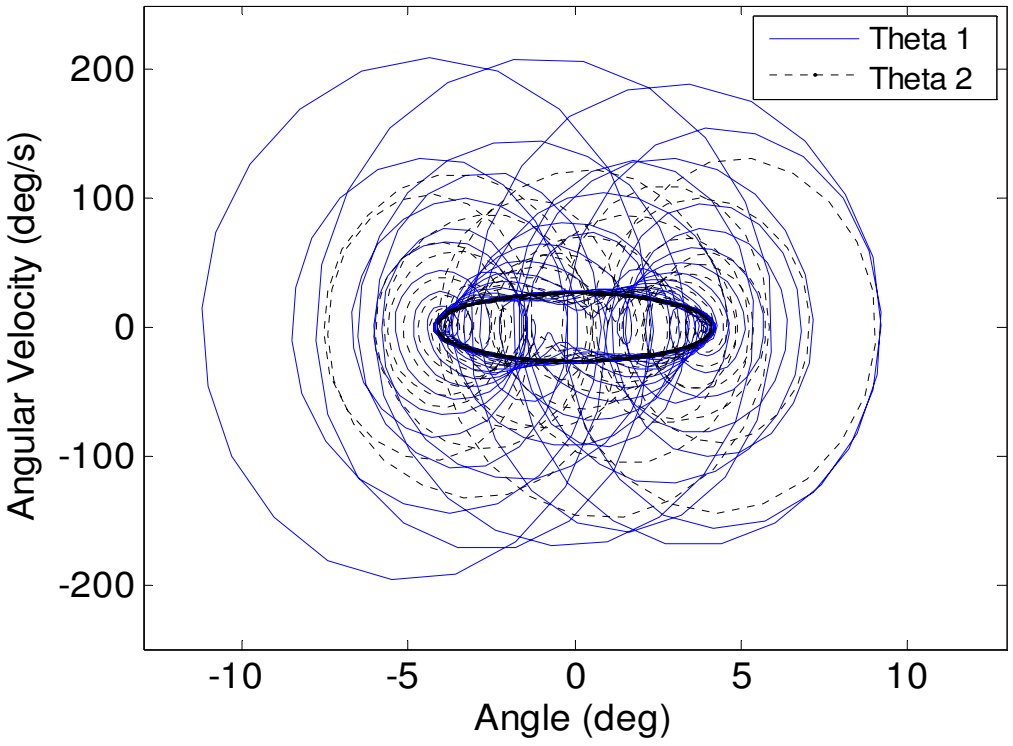

Figure 5.12: Phase plot for the upper and lower segments of the Acrobot.

The equilibrium manifold was calculated for the balanced Acrobot. Since m_1 and m_2 are equal and l_1 is twice l_2 (refer to Figure 5.1), the balanced Acrobot is in static equilibrium when $\theta_1 = \theta_2$, provided that an appropriate torques is applied at the mid joint to stop movement (Note that Murray and Hauser define θ_2 as the angle between segments while the model developed herein considers θ_2 to be the angle with respect to the global vertical reference). Thus, the equilibrium manifold for the balanced Acrobot is simply a line with a slope of -1 plotted on the zero velocity plane ($\dot{\theta}_1 = \dot{\theta}_2 = 0$) (Figure 5.13).

Trajectories were calculated for a 31x31 grid of initial values between the angles of ± 15 degrees. These trajectories were allowed to evolve for 5 seconds. Stable trajectories remained close to the origin in state space and unstable trajectories quickly diverged. Unstable trajectories were evolved until they reached an angle exceeding 300 degrees, definitively indicating unstable behavior. Those trajectories that failed to stay within the bounds (±300°) were considered unstable and marked with a cross at their initial location in state space. Those trajectories that remained bounded for 5 seconds were considered stable marked with a circle (Figure 5.13). Notice that the stable trajectories lie close to the equilibrium manifold found using an independent method. In addition, results are found to be similar to those shown in Figure 5.4. There are a few stable outliers in the field. Perhaps, these represent trajectories that generally lie outside the stable region but happen to move into the stable region at some time during their evolution. As a result, these trajectories may also be attracted toward the equilibrium manifold.

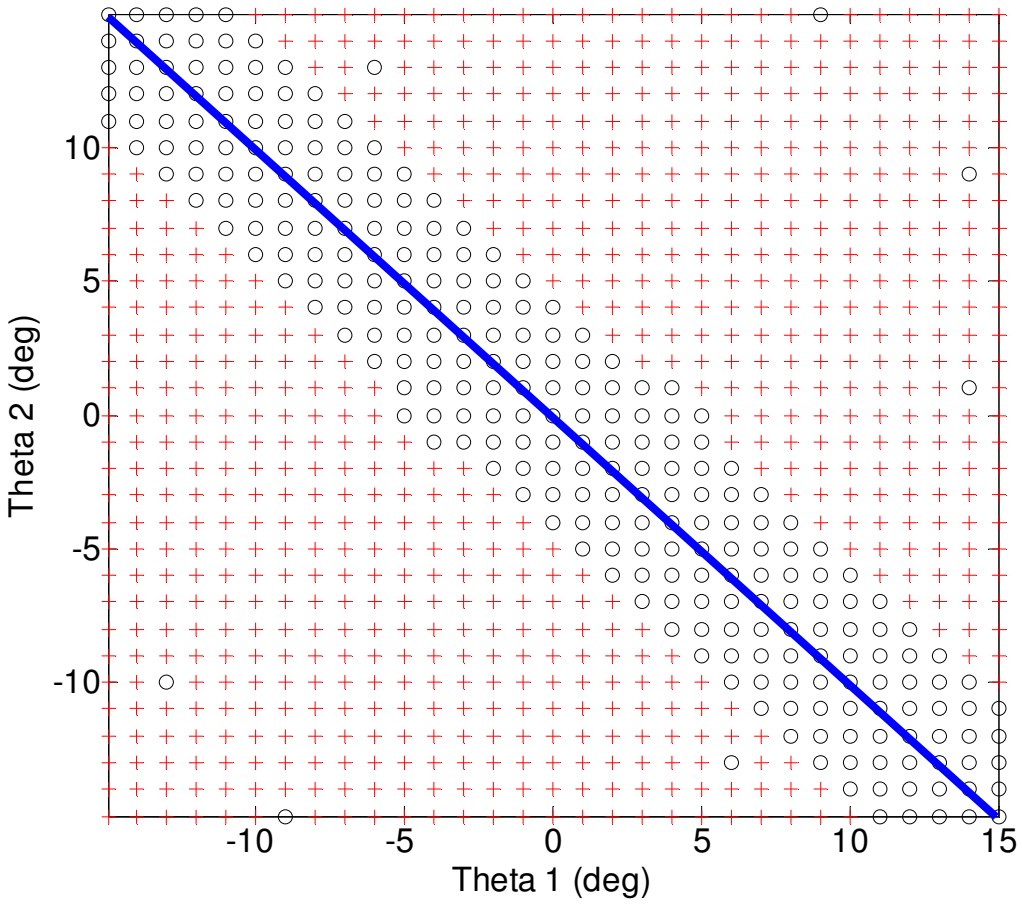

Figure 5.13: The blue line show the location of the equilibrium manifold. Circles show initial locations where trajectories remained in the neighborhood of the origin. Crosses represent initial locations that resulted in unstable trajectories.

The methods used to calculate the FTLE field for the inverted pendulum were expanded to four dimensions and applied to the Acrobot. The FTLE field generated (using the regular grid method) showed a trough near the location of the equilibrium manifold (Figure 5.14). In addition, LCS were observed on each side of the trough. Since the LCS represent separatrices in trajectories, they should lie on the boundary between the stable and unstable regions of state space. Indeed, the LCS are observed to align well with the boundary between stable and unstable trajectories shown in Figure 5.13.

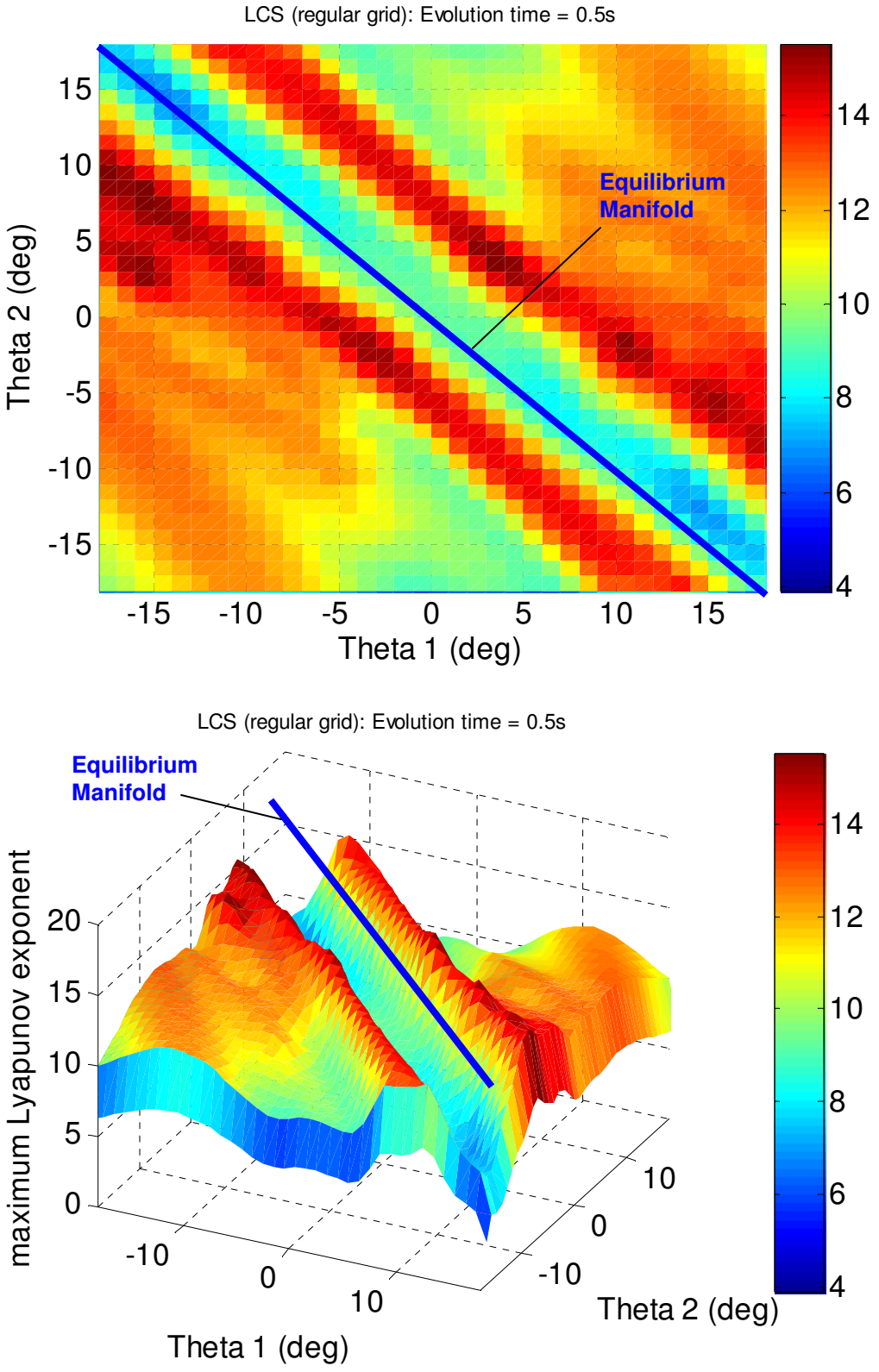

Figure 5.14 – LCS are visible in both the (a) top view and (b) 3D view of the FTLE field for the Acrobot.

With a stable controller found for the Acrobot and the ability to generate LCS for this system, these initial parameter values were used as a starting point to generate similar results for the wobble chair. The FTLE field for the wobble chair was generated by slowly morphing the Acrobot into the wobble chair as described above and applying the FTLE calculation technique described in section 4.2.3.

5.4.2 Analysis of the Deterministic Planar Wobble Chair

The existence of the equilibrium manifold for the wobble chair was not known prior to evaluation of the Acrobot. However, since the wobble chair is a diffeomorphisms of the Acrobot and it was known that an equilibrium manifold exists for the Acrobot, one may conclude that an equilibrium manifold must also exist for the wobble chair. This is yet another example of how evaluating a defeomorphism can add new insight into a system.

In order to find the location of the equilibrium manifold, a series of equilibrium points were calculated. For a given angle of segment one, equilibrium points were found by determining the angle of the second segment needed for the sum of the moments about the free pin joint to equal zero (Figure 5.15). An appropriate torque was applied at the actuated pin joint in order to resist motion. The results were similar to the unbalanced Acrobot (Figure 5.2) and the physical Acrobot (Figure 5.3). In the actual wobble chair experiments, participants were constrained by the equipment to remain close to the origin of the graph, within ± 15 degrees. Over this range, the equilibrium manifold is almost linear when plotted on the zero velocity plane of state space.

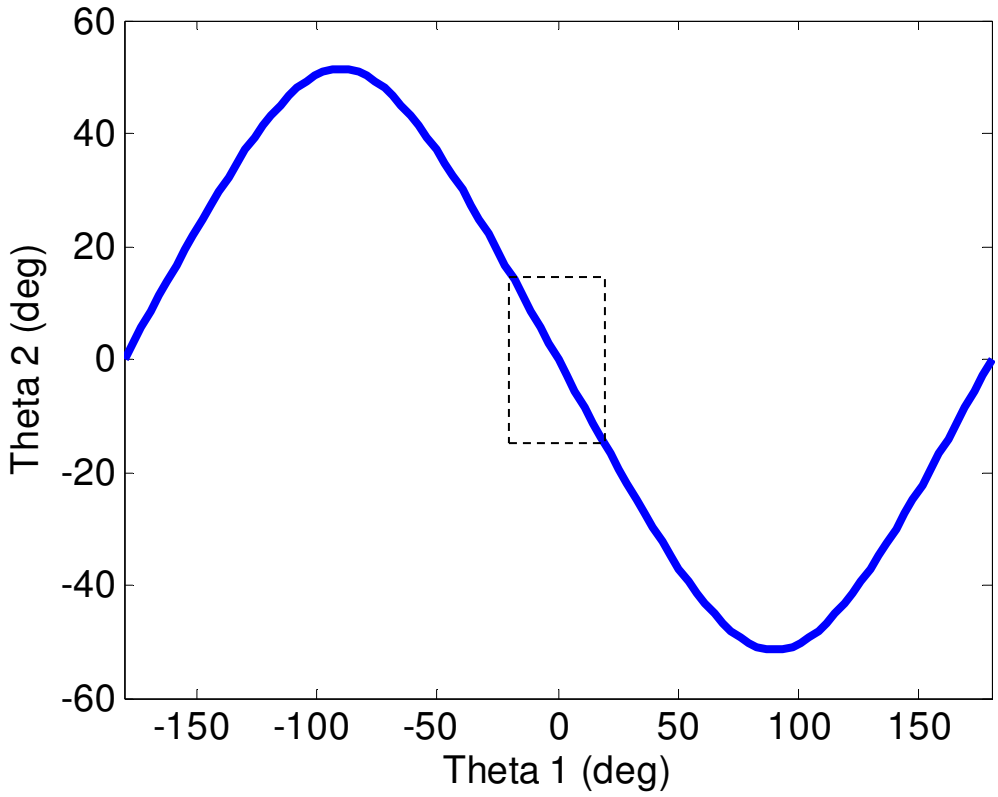

Figure 5.15: Equilibrium manifold for the wobble chair. The box indicated the region that is attainable in wobble chair experiments. Results are plotted on the zero velocity plane ($\dot{\theta}_1 = \dot{\theta}_2 = 0$).

Beginning with these controller gains for the balanced Acrobot made finding appropriate gains for the wobble chair easier than finding these "from scratch". Through morphing stable controller gains were found for the wobble chair which previously could not be found through trial and error.

Starting from initial angles of -2.2 and 1.8 for theta 1 and theta 2, respectively, the wobble chair dynamics were simulated. A truly convergent system was found using a proportional gain of 3×10^5 and a derivative gain of 200 (Figure 5.16). With this system, the segment oscillations converged to zero (Figure 5.17). The phase plot is also consistent with a convergent system (Figure 5.18).

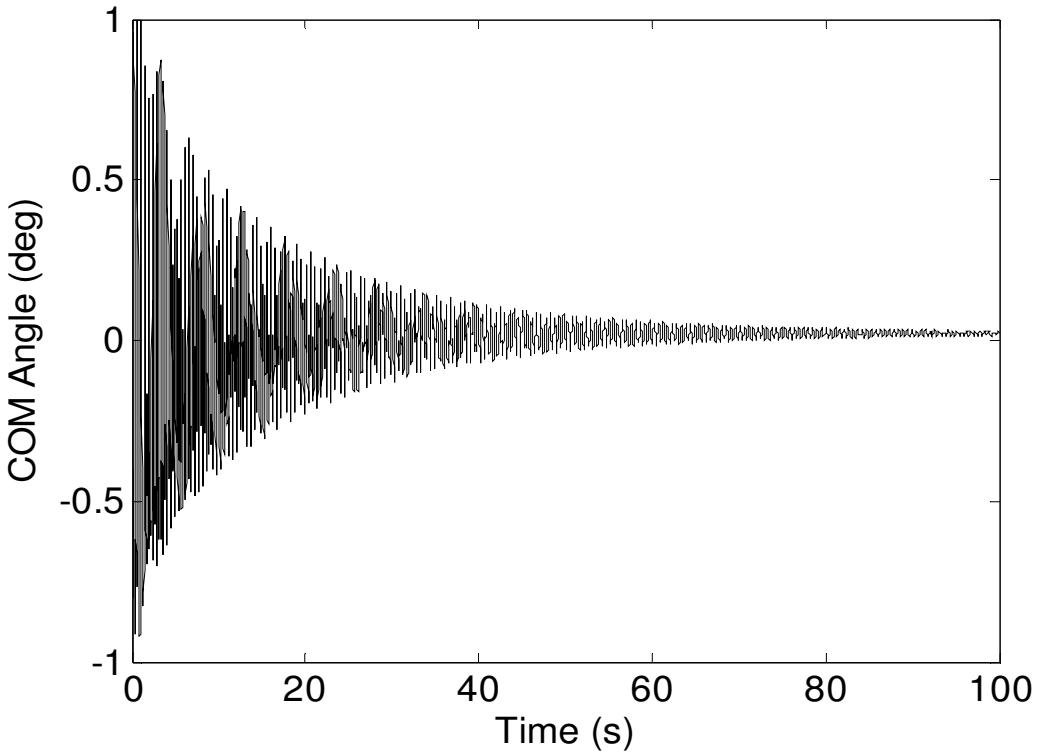

Figure 5.16: Simulation results showing that PD control drove the center of mass to the equilibrium manifold.

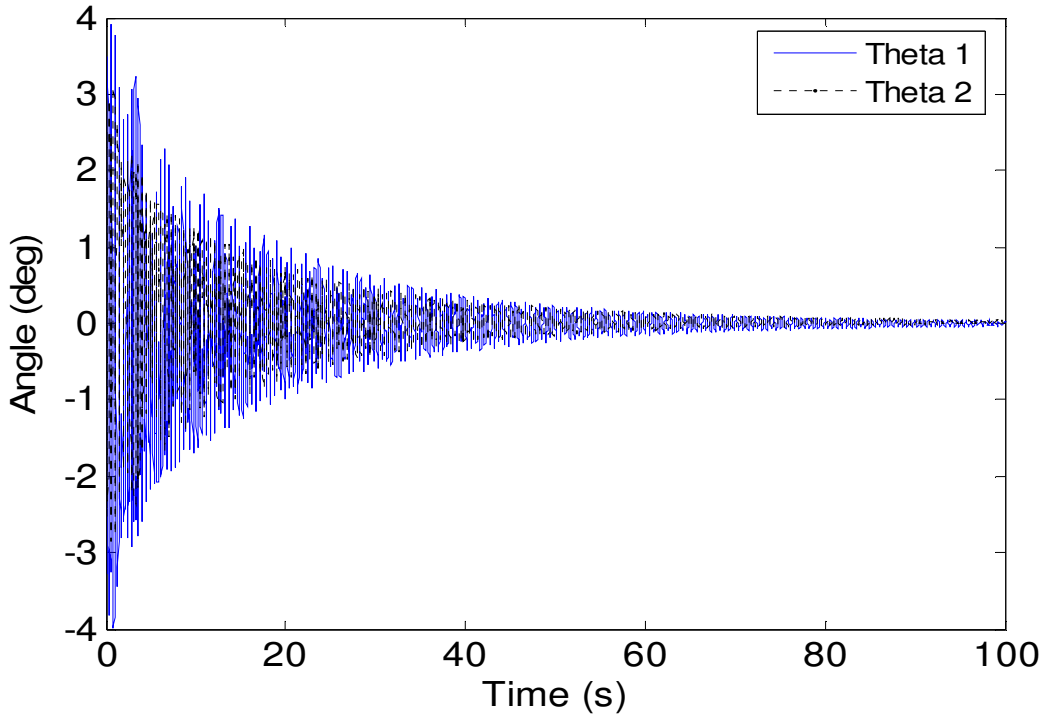

Figure 5.17: Time plot for the upper and lower segments of the wobble chair.

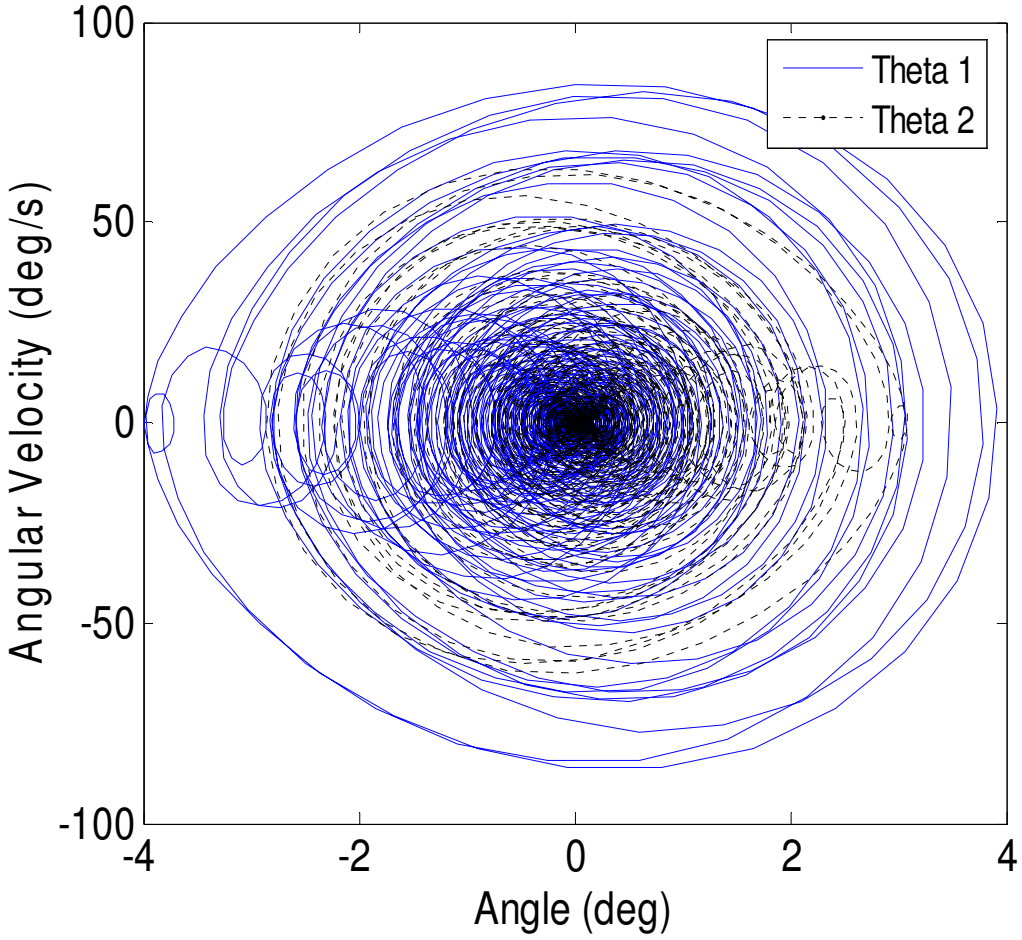

Figure 5.18: Phase plot for the upper and lower segments of the wobble chair.

With the controller gains now defined, trajectories were calculated for an 80x80 grid of initial values between the angles of ± 8 degrees (Figure 5.19). Trajectories that stayed remained bounded (± 300°) were determined to be stable according to Lyapunov in the finite time. As before, stable and unstable initial locations were marked with circles and crosses, respectively. Notice that the basin of stability is much smaller than the one found for the Acrobot. This may be the reason why a stable controller could not be found for the wobble chair until a solution was first found for the Acrobot.

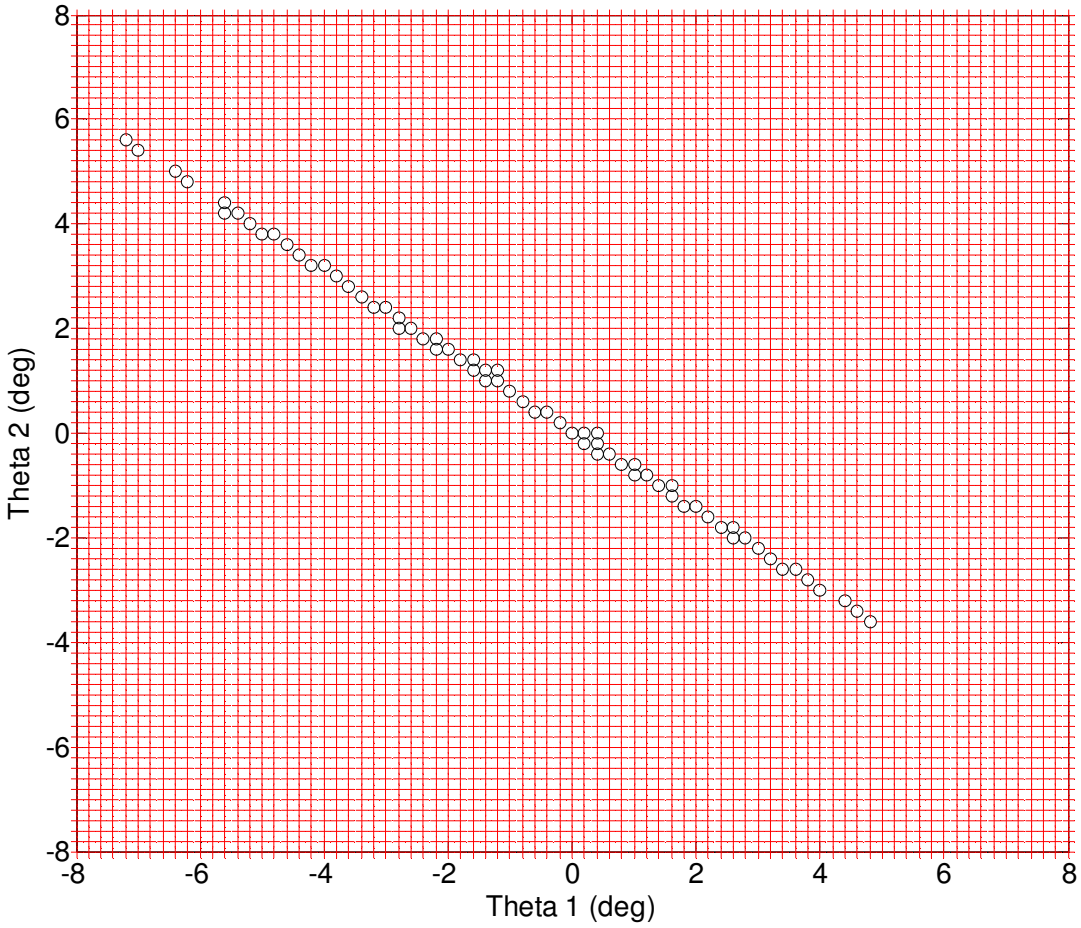

Figure 5.19: Global view of the basin of stability based on the outcomes of trajectories. Circles show initial locations where trajectories remained in the neighborhood of the origin. Crosses represent initial locations that resulted in unstable trajectories.

Next, the regular grid method was used to find the location of the basin of stability for the wobble chair. The technique was similar to that used in chapter 4 but expanded from two dimensions to four. Briefly, the finite time Lyapunov exponent was calculated by determining the local deformation of a regular grid in four orthogonal dimensions. Using this technique, the LCS for the wobble chair was found (Figure 5.20-22).

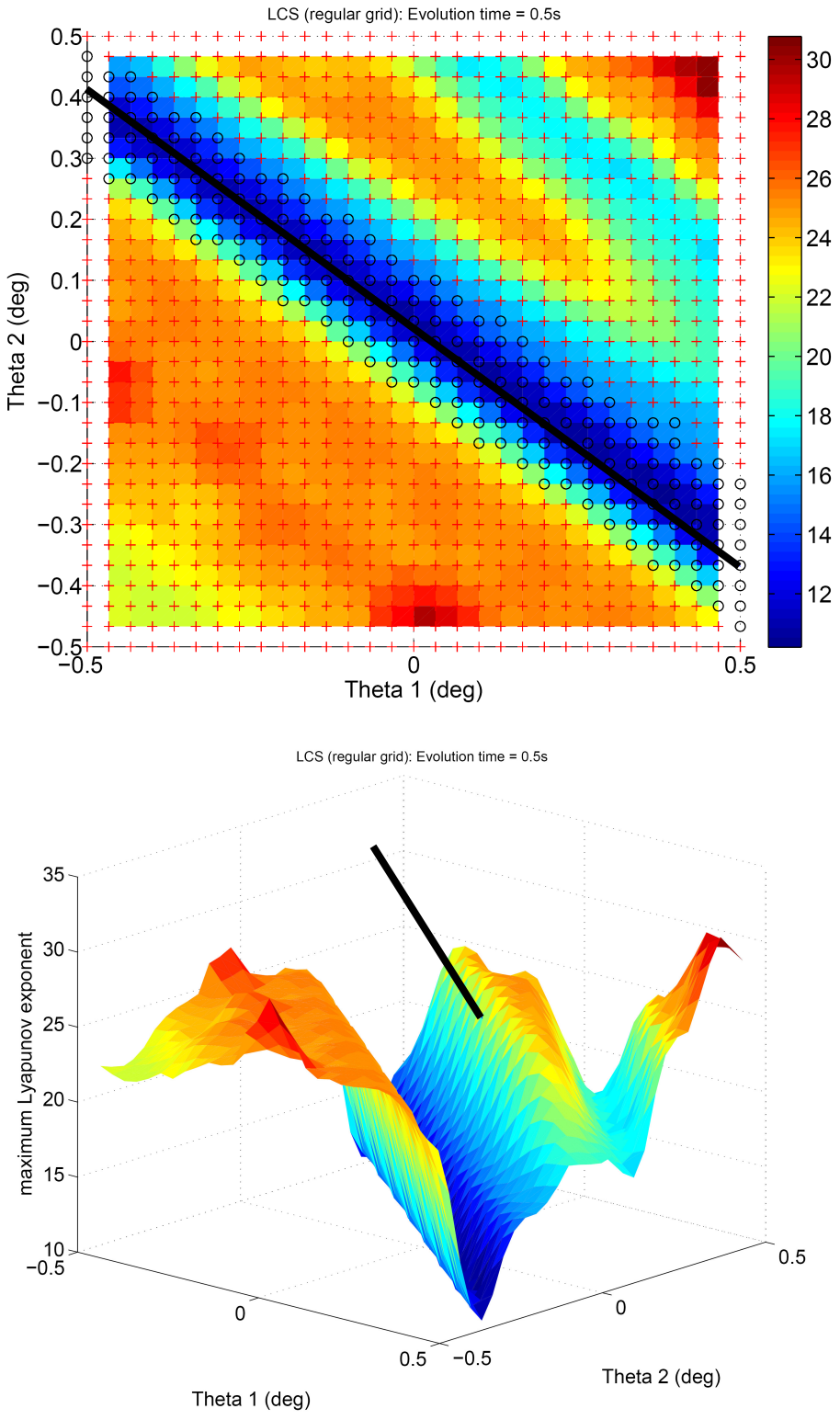

Figure 5.20: In the θ_1, θ_2 plane, LCS are visible in both the (a) top view and (b) 3D view of the FTLE field for the wobble chair. The equilibrium manifold (black line), LCS (ridges), and stable trajectory evolutions (circles) were all observed to correlate well.

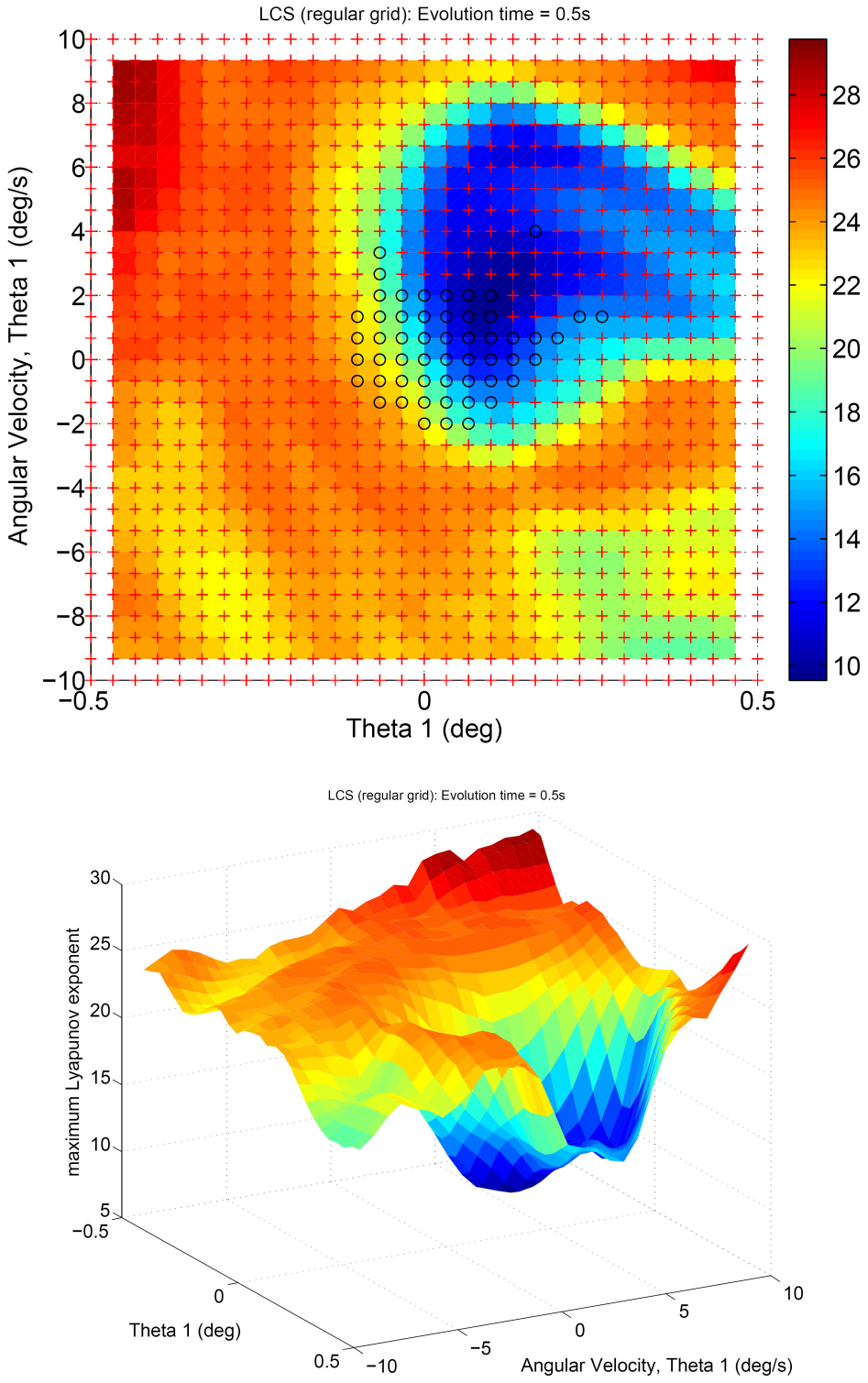

Figure 5.21: In the θ_1 phase plane, a depression in the FTLE field is observed to the upper right of the origin in the (a) top view. A (b) 3D view of the FTLE field for the wobble chair is also shown.

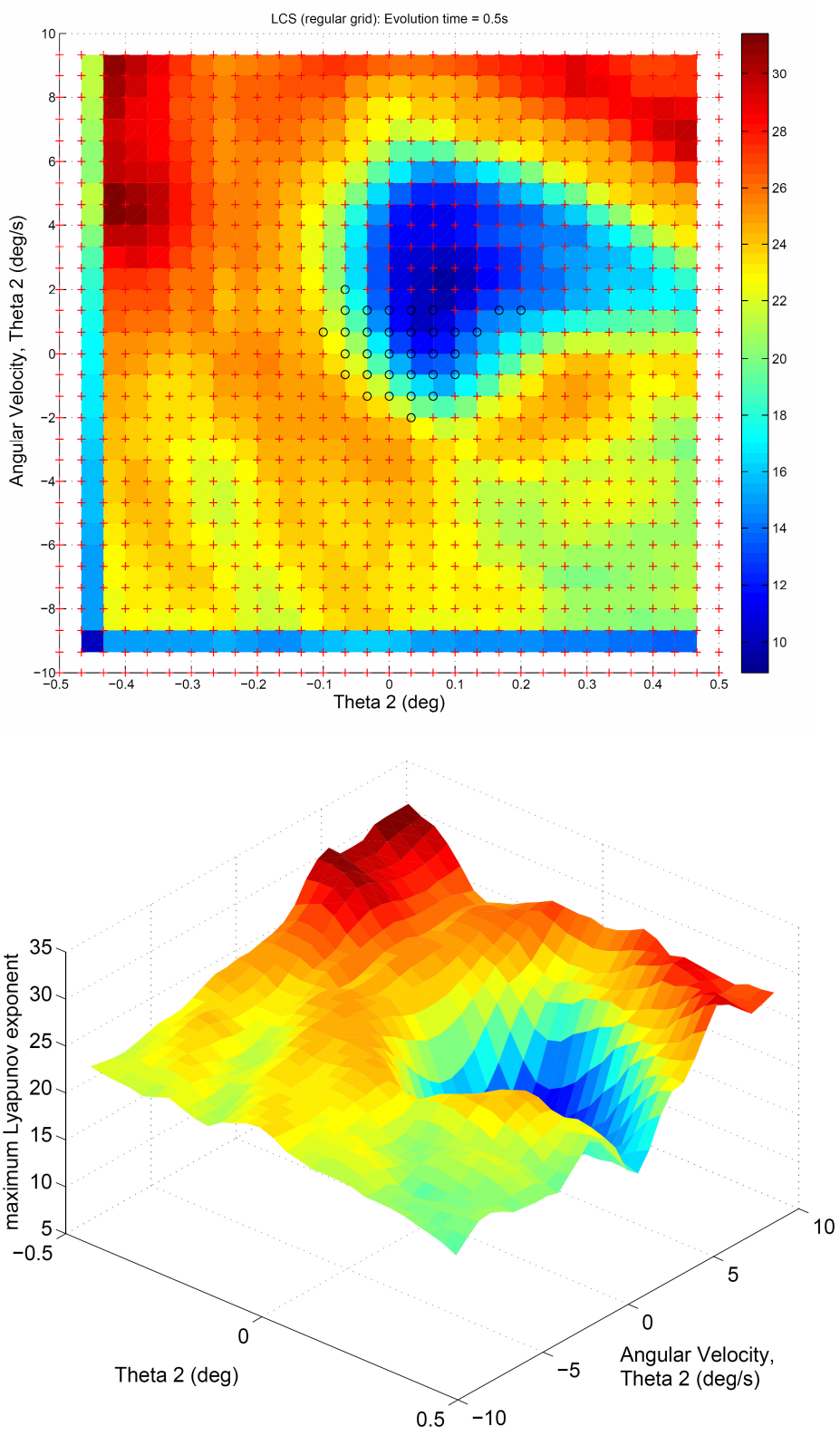

Figure 5.22: In the θ_2 phase plane, a depression in the FTLE field is observed a little closer to the origin in the (a) top view. A (b) 3D view of the FTLE field for the wobble chair is also shown.

The location of the equilibrium manifold (black line) shown in Figure 5.20 was found to align well with the trough of the FTLE field. In addition, the basin of stability found through the evolution of trajectories (circles) was also observed to correlate well with the LCS (ridges) in all figures. In the phase plots (Figure 5.21 & 5.22), the basins of stability found through the LCS method were larger than that found through evolution of trajectories. This may be due to the tendency of the system to be more stable to forward perturbations caused by system asymmetry. The same controller gain parameters found in this section were used to generate trajectories for the stochastic simulation in the following section.

5.4.3 Stochastic Analysis of the Planar Wobble Chair

The stochastic analysis of the planar wobble chair is similar to that performed for the inverted pendulum in section 4.4.3. Beginning from rest at $\theta_1 = \theta_2 = 0$, random force perturbations were used to destabilize the system while the controller and springs provided restorative moments. The first task was to use the mathematical model to generate time series data representative of that collected from experiments. This is an intermediate step towards being able to analyze actual experimental data which will be performed in chapter 6.

From the time series data, two methods were employed to calculate the finite time Lyapunov exponent (FTLE). Each method differs in the way that the FTLE was calculated. However, both methods were used to generate an FTLE field. In the Euclidean distance method (refer to section 4.4.3), the maximum FTLE is found by determining the rate of separation (Euclidean distance) of two nearest neighbors in n-dimensional state space (Rosenstein et al. 1993a). The Euclidean distance in state space is the square root of the sum of the squares of the distances in each dimension. This method has been used by several researchers to calculate

FTLE for biodynamic applications (Rosenstein et al. 1993a; Dingwell et al. 2000; Granata and England 2006; Kang and Dingwell 2006). In the second method, the state transition matrix method, the FTLE is calculated from the state transition matrix which is determined by evaluating the rate of expansion of a n-dimension hyper-ellipse (Shadden et al. 2005; Lekien et al. 2007).

5.4.3.1 Generation of trajectories

The mathematical model for the wobble chair was used to generate time series data. Beginning from the origin (0,0,0,0) in state space, random force perturbations were applied to the system causing movement. Twenty trials were conducted at noise level of 10% ∇G and a noise frequency of 20 Hz. The noise had a Gaussian distribution but was bounded such that it could not exceed 3σ. The same control parameters used for the deterministic analysis of the wobble chair were used in the stochastic simulation ($G_p = 3x10^5$, $G_d = 200$). Simulation time was set to 30 seconds, however if either angle exceeded a magnitude of 300 degrees, the trial was stopped. These large angles occur when the system becomes unstable. As before, the controller drove the system toward the equilibrium manifold (Figure 5.23). With this system, the segments oscillated near zero until the combination of perturbations caused them to go unstable (Figure 5.24). The phase plot shows both stable and unstable trajectories (Figure 5.25).

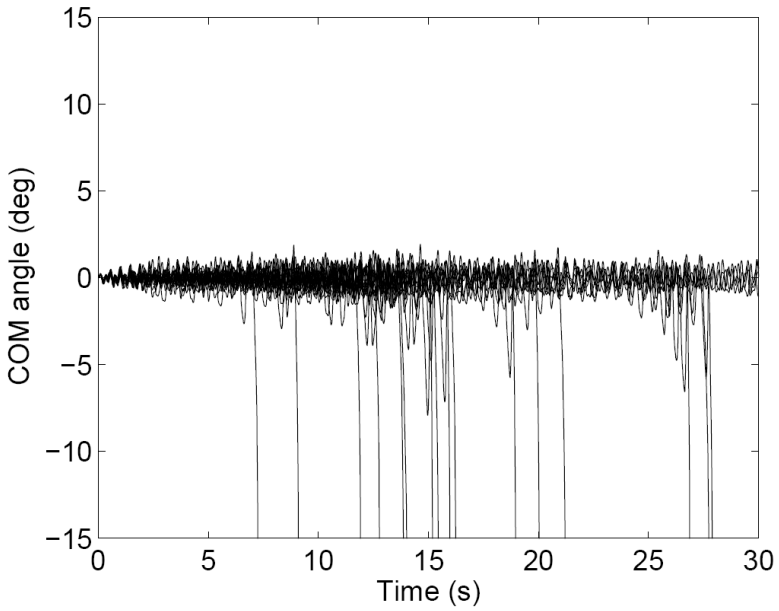

Figure 5.23: Simulation results showing the location of the center of mass over 50 trials. The PD controller drove the system towards the equilibrium manifold.

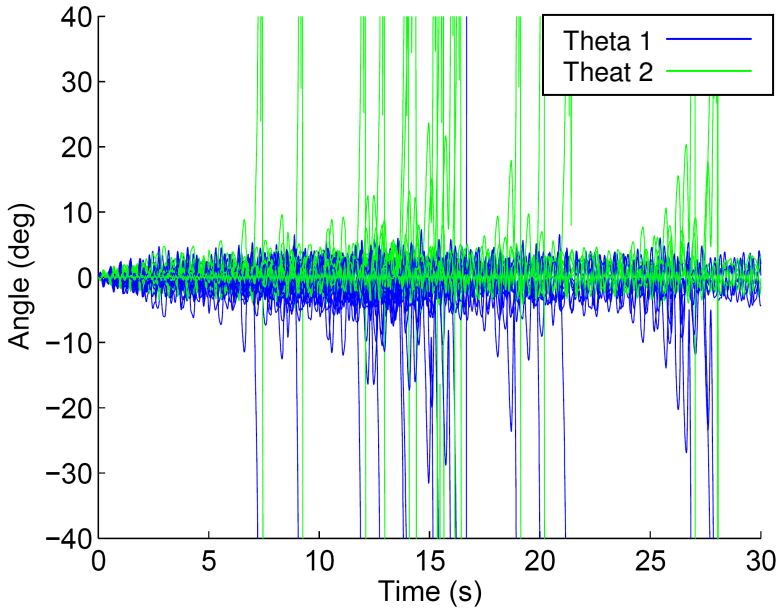

Figure 5.24: Time plot for the upper and lower segments of the wobble chair. Both stable and unstable dynamics are visible.

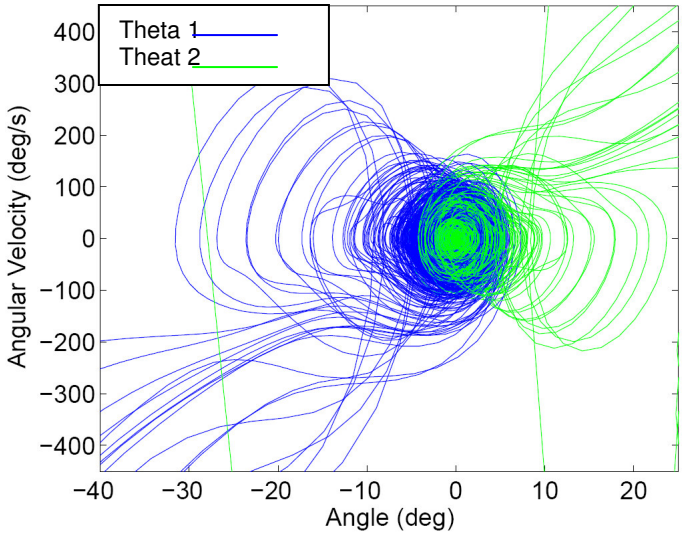

Figure 5.25: Phase plot for the upper and lower segments of the wobble chair. Both stable and unstable dynamics are visible. Stable behavior occurs within ~4 degrees of the origin (see 5.24).

5.4.3.2 Euclidean distance method

Recall equation (2.3), $d(t) = d(0)\, e^{\lambda t}$. The Euclidean distance was calculated in four dimensions for the planar wobble chair. Thus, the distance, d(t), is determined by,

$$d(t) = \sqrt{(\theta_{1,n} - \theta_{1,r})^2 + (\dot{\theta}_{1,n} - \dot{\theta}_{1,r})^2 + (\theta_{2,n} - \theta_{2,r})^2 + (\dot{\theta}_{2,n} - \dot{\theta}_{2,r})^2} \qquad (5.17)$$

where the subscripts n and r refer to the neighbor and the reference point, respectively. Using this method the Lyapunov exponent, λ, was found by fitting the divergence to an exponential function of evolution time, t, over the time interval [0.2, 0.7] seconds (refer to section 2.2.3).

5.4.3.3 State transition matrix method

The second method employed to generate the FTLE field was the state transition matrix method. The state transition matrix, Φ, is a function that describes how a perturbation from a reference trajectory evolves over time (Shadden et al. 2005; Lekien et al. 2007). This is the same matrix that was used to generate the FTLE field for the deterministic systems in the previous section.

Like the Euclidean distance method, the state transition matrix was calculated for each reference point. First, target points were defined a distance δq in the positive and negative direction of the first dimension (cyan points – Figure 5.26). The nearest neighbor to either of the target points (green point) was found. The vector from the reference point to this first neighbor defined the first principle direction (green arrow). Next, target points were defined at a distance δq in the positive and negative directions of the second dimension (yellow points). The nearest neighbor to either of the target points (magenta point) was found, and a vector from the reference point to this first neighbor defined the second principle direction (magenta arrow). This process was repeated for each dimension of state space. Upon completion, these vectors defined a basis that spans the dimensions of phase space. Since a preliminary investigation showed the principle directions to align very closely with the basis vectors of the reference frame, those basis vectors were used for the analysis.

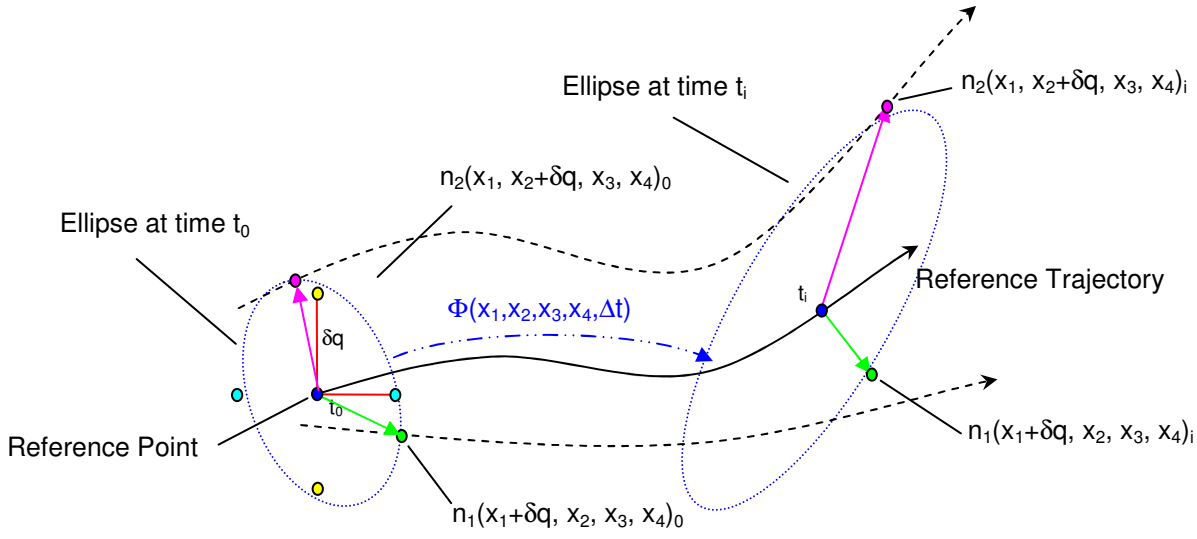

Figure 5.26: The state transition matrix was calculated by first forming a basis about the reference point using nearly orthogonal vectors, then tracking the trajectories forward in time (Δt) and determining the changes in the basis vectors.

As these points were tracked forward in time, the length and orientation of the basis vectors changed revealing how a ball of nearest neighbors deforms. For simplicity of illustration, consider the 2-dimensional case and let $\vec{x} = (x_1, x_2) = (x, y)$ and

$$\Phi(x, \Delta t) = \begin{bmatrix} \dfrac{x_{n1}(t+\Delta t) - x_r(t+\Delta t)}{x_{n1}(t) - x_r(t)} & \dfrac{x_{n2}(t+\Delta t) - x_r(t+\Delta t)}{y_{n2}(t) - y_r(t)} \\ \dfrac{y_{n1}(t+\Delta t) - y_r(t+\Delta t)}{x_{n1}(t) - x_r(t)} & \dfrac{y_{n2}(t+\Delta t) - y_r(t+\Delta t)}{y_{n2}(t) - y_r(t)} \end{bmatrix} \tag{5.18}$$

where the subscripts n and r indicate a neighbor or reference point, respectively. The diagonal terms represent expansion or contraction, and the off-diagonal terms indicate shearing (Figure 5.27).

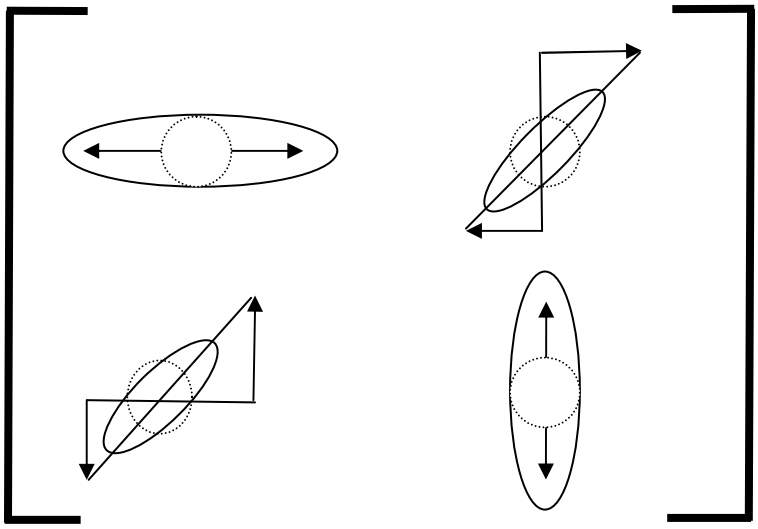

Figure 5.27: Graphical representation of the terms that make up the gradient of the state transition matrix.

5.4.3.5 Results - Euclidean distance method

The Euclidean distance method was applied to the time series generated above. The resulting FTLE field is shown below for the zero velocity plane (Figure 5.28). Since all trajectories began from the origin, little is known about the data outside of the thin band. The available data showed that the trajectories with near zero velocity for both segments to only existed near the equilibrium manifold. Little structure was noticeable in the FTLE field in either of the phase plots using the Euclidean distance method (Figures 5.29 & 30).

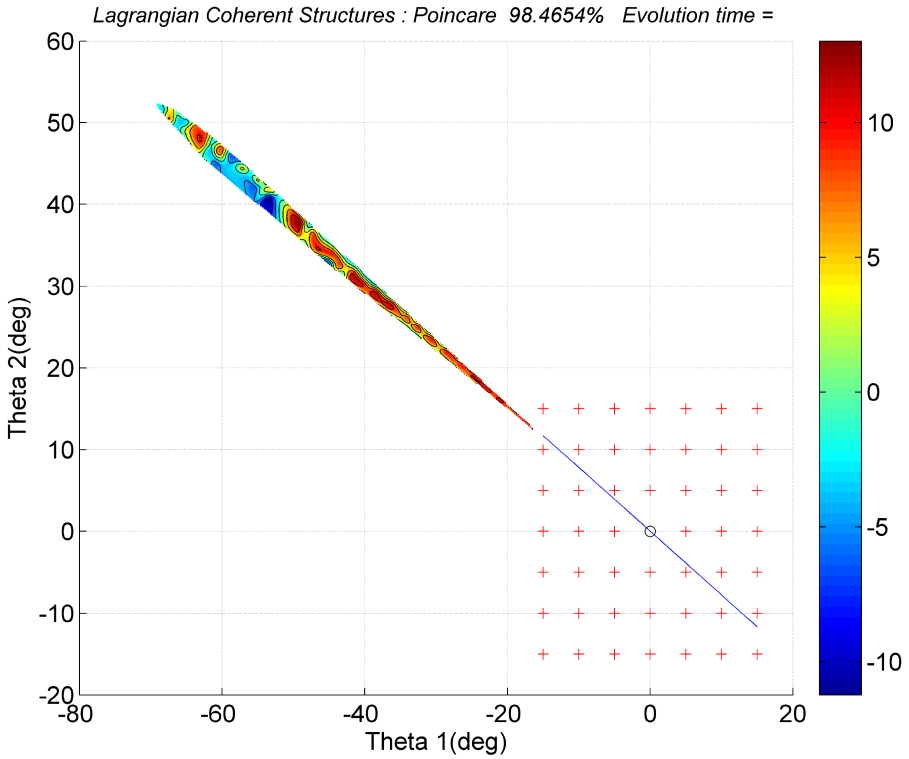

Figure 5.28: FTLE field for the wobble chair generated using the Euclidean distance method. This two dimensional plot shows the zero velocity section of the four dimensional system. Poincaré section width was 50% of the range of the data.

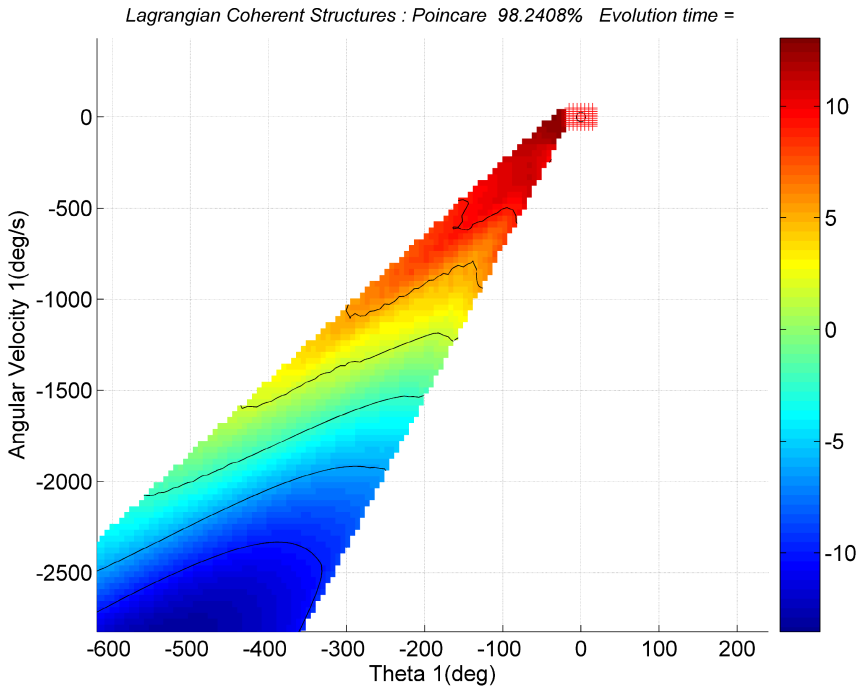

Figure 5.29: FTLE field for the wobble chair generated using the Euclidean distance method. This two dimensional plot shows the $(\theta_1, \dot{\theta}_1)$ slice of state space. The position and velocity of θ_2 is reduced to a 10% band around $(\theta_2 = 0, \dot{\theta}_2 = 0)$.

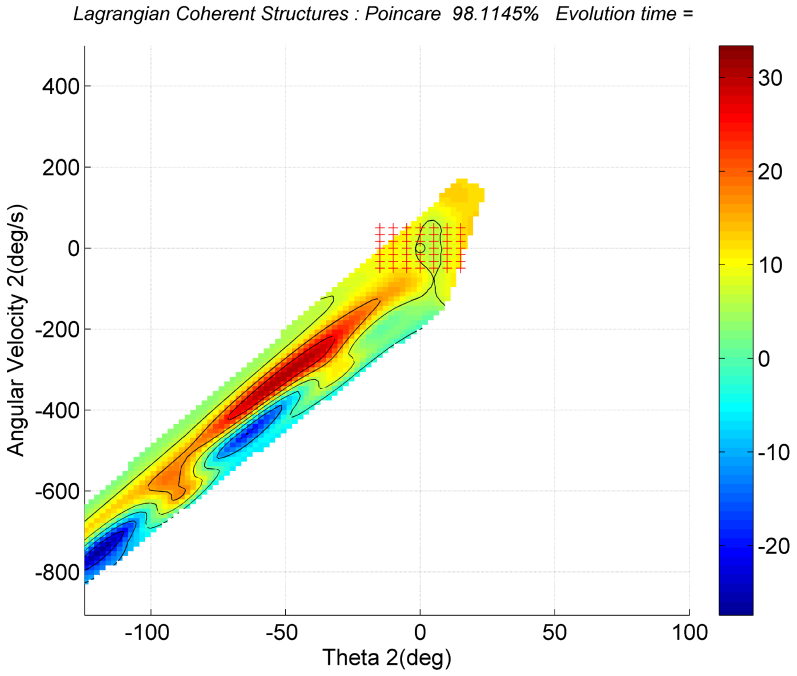

Figure 5.30: FTLE field for the wobble chair generated using the Euclidean distance method. This two dimensional plot shows the $(\theta_2, \dot{\theta}_2)$ slice of state space. The position and velocity of θ_1 is reduced to a 10% band around $(\theta_1 = 0, \dot{\theta}_1 = 0)$.

5.4.3.6 Results – State Transition Matrix method

The state transition matrix method was applied to the same time series data. The resulting FTLE field is shown below for the zero velocity plane (Figure 5.31). The results were similar to those found using the Euclidean distance method. Data was only present on the equilibrium manifold.

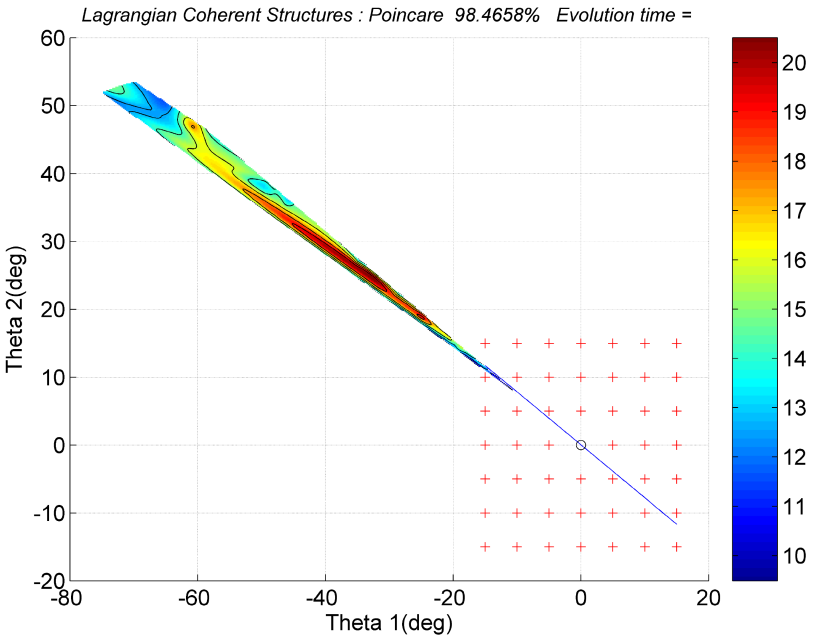

Figure 5.31: FTLE field for the wobble chair generated using the state transition matrix method. This two dimensional plot shows the zero velocity section of the four dimensional system. 100% of the available data is shown.

In the phase plots, structure was visible in the FTLE field. A depression was noticeable around the origin in 4D state space (Figure 5.32 & 5.33). For the θ_1 phase plot, the shape of the depression was smooth, but its magnitude was much larger than found through tracking trajectories. For the θ_2 phase plot, the ridges surrounding the depression were less smooth. Again, the magnitude of the basin of stability was larger than that calculated through trajectories.

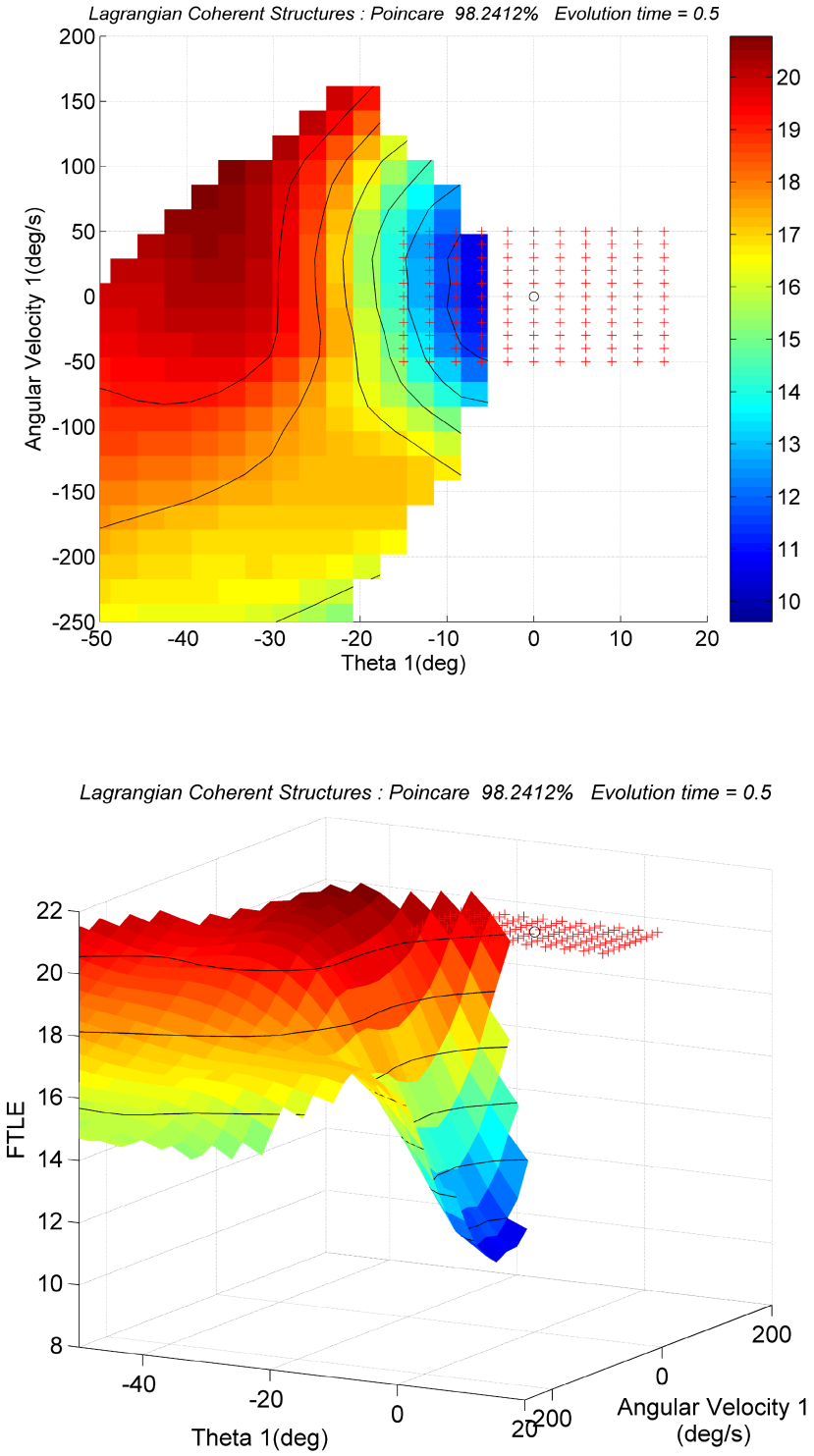

Figure 5.32: FTLE field for the wobble chair generated using the state transition matrix method. This two dimensional plot shows the $(\theta_1, \dot{\theta}_1)$ slice of state space. The position and velocity of θ_2 is reduced to a 10% band around $(\theta_2 = 0, \dot{\theta}_2 = 0)$.

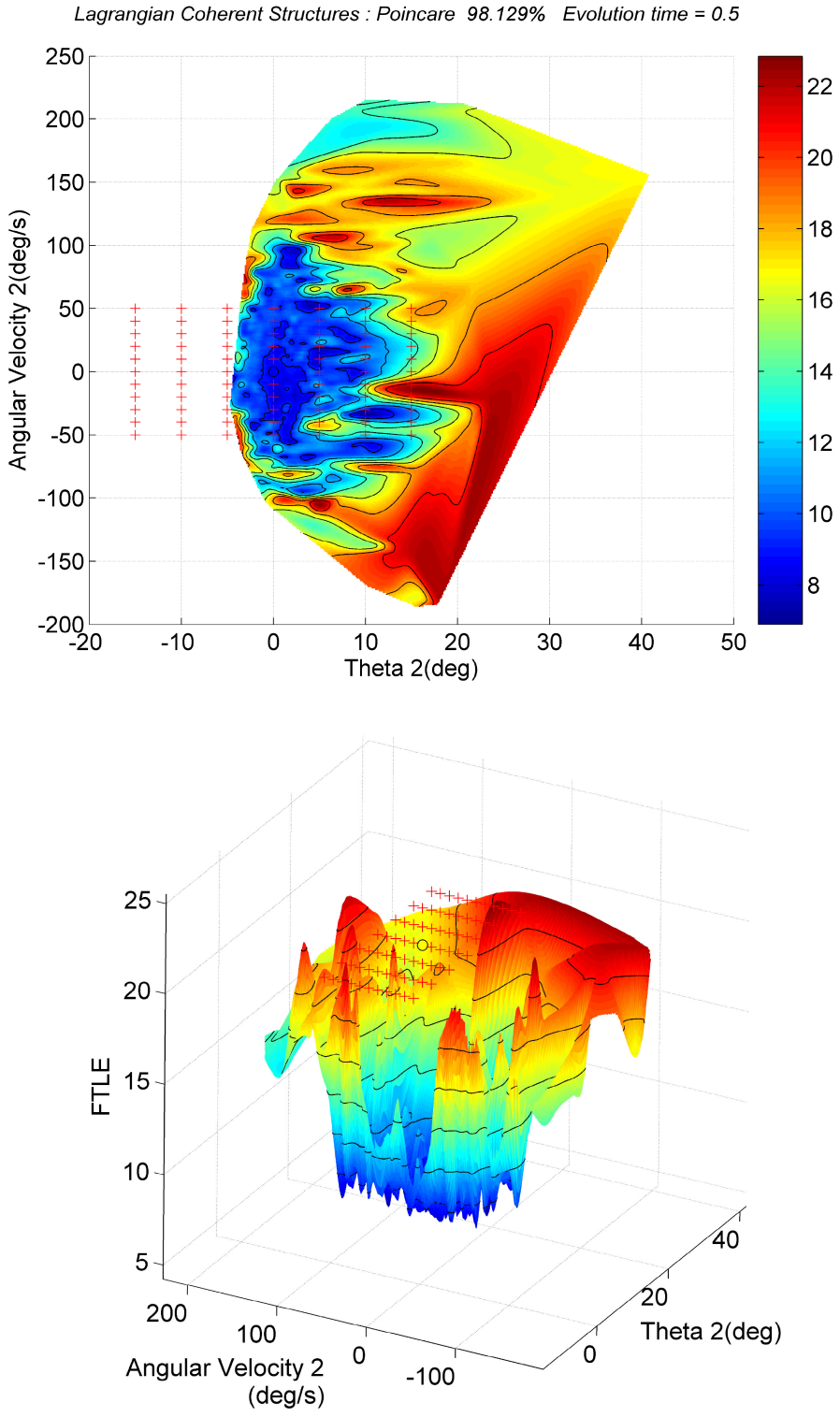

Figure 5.33: FTLE field for the wobble chair generated using the state transition matrix method. This two dimensional plot shows the $(\theta_2, \dot{\theta}_2)$ slice of state space. The position and velocity of θ_1 is reduced to a 10% band around $(\theta_1 = 0, \dot{\theta}_1 = 0)$.

Another way to view the four dimensional results is to create a two dimensional grid of two dimensional data (Figure 5.34). The value of the FTLE at any location is given by the height and color of the plot. Below is a 4D plot generated to show the effect of non-zero velocities on the size and location of the basin of stability. The location of the basin of stability was observed to shift with velocity (see also reference file "LCS non-zero velocities.ppt"). It is observed that when the lower body velocity, $\dot{\theta}_1$, is balanced by a upper body velocity, $\dot{\theta}_2$, in the opposite direction and a magnitude of ~1.5 times, the LCS is still present. This result is consistent with logical thought, but the magnitude difference was non-intuitive and would have gone unnoticed without the 4D plot.

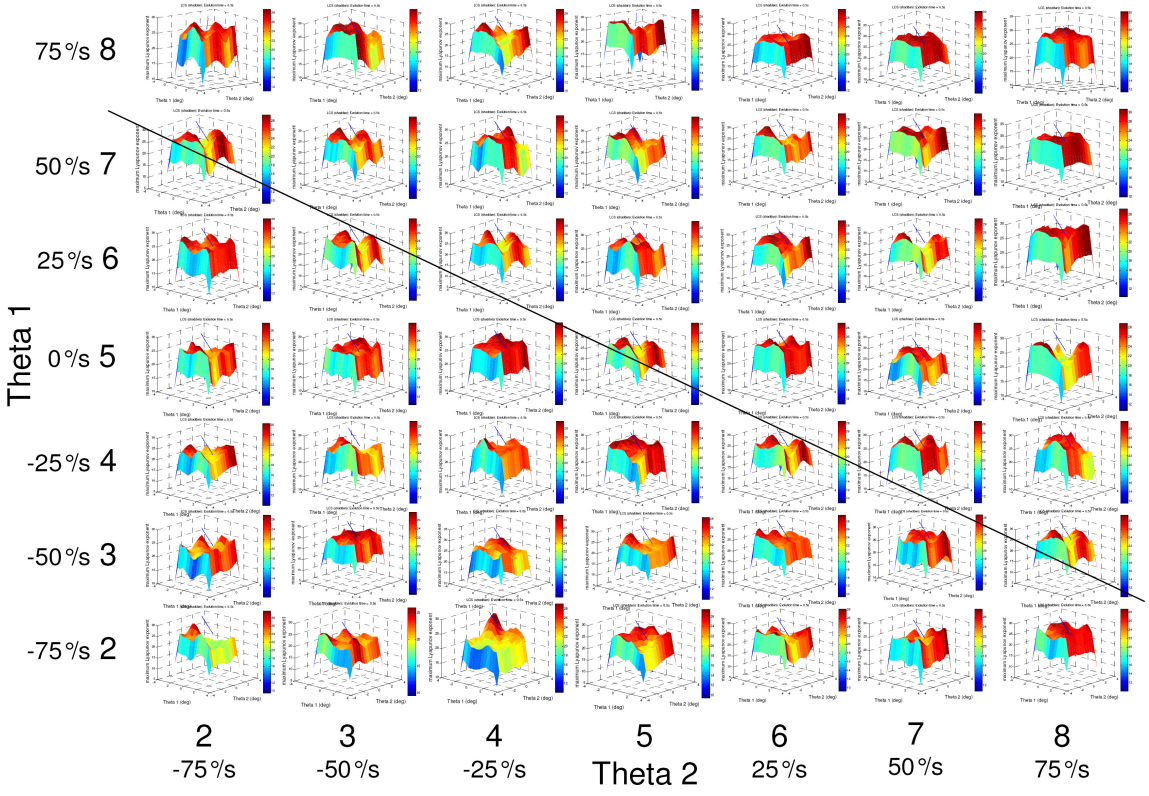

Figure 5.34: The 2-dimensional figures are arranged into a two dimensional grid. By comparing the figures at different grid locations, the full four dimensional basin of stability can be visualized (see associated document, "4D Basin of Stability")

5.5 Discussion

The mathematical model of the Acrobot matched well with the published results. Since the governing differential equations were the same for both the Acrobot and the wobble chair, this verifies the equations used for the simulations. The basins of stability obtained using the regular grid method for the deterministic system showed good resolution. As expected, ridges formed at the boundary between the stable and unstable regions. The sizes of the basin of stability matched well with the basin of stability determined by tracking trajectories. The basin of stability was found to be smaller for the wobble chair than the Acrobot. It is likely that this arises from the asymmetry of the system. The system is less tolerant to negative perturbations than positive ones. This effect was observed as a shift in the location of the basin of stability towards the upper right corner of the phase plot. This makes the edge of the basin of stability closer to the equilibrium manifold in the negative directions implying that it is easier to fall with the total center of mass moving backwards. In the simulations this usually occurred with the lower body, θ_1, falling backwards and the upper body falling forwards, θ_2 (Figure 5.24).

This effect was also observed in the stochastic analysis. Recall that all of the trajectories began at the origin in state space and were perturbed by random noise equally in both directions. For those trajectories that did not stay in the neighborhood of the origin, all of them became unstable with the center of mass moving in the negative direction. Limited results were obtained from the stochastic analysis of the time series data.

The Euclidean distance method did not yield structure for any of the Poincaré sections. On the other hand, the state transition matrix method yielded structure in the phase plots, but these did not match well with the size of the structures found in the deterministic simulation. The large size of the basin of stability found in the stochastic analysis may be a result of the short

evolution time. In the deterministic system, an evolution time of 0.5 seconds was adequate to determine the direction of motion. However, with the added noise of the stochastic system, longer evolution times may be necessary to find the basin of stability using this method. It may also be possible that the basin of stability was too small to find using the methods applied. A different controller may provide larger basin of stability that may be easier to detect using this method. The neuromuscular control applied by the human brain is expected to be more effective than the simple PD control modeled herein. Although neuromuscular control has time delay that retards performance, it is probably highly nonlinear and able to provide anticipatory control. Considering these factors, it is possible that the basin of stability will be larger for actual human balance control.

5.6 Summary and Conclusions

In this chapter, a mathematical model was developed for the planar wobble chair using anthropometric data to calibrate the model for a typical human subject. The governing differentials equation were developed for this model and solved numerically to find trajectories. These trajectories were evaluated to find finite time Lyapunov exponents (FTLE). The state space distribution of the FTLE was tracked, and a FTLE field was generated. This was used to find Lagrangian coherent structures and the locations of the basin of stability.

Analyses of the deterministic model were effective in finding the basin of stability for the wobble chair. However, results obtained for the stochastic system could not be correlated with those found by the deterministic methods of tracking the evolution of trajectories. Yet, structure was observed in the FTLE field using the state transition matrix method. Future evaluations using different evolution times and/or system parameters may yield a rewarding conclusion.

Chapter 6

Determining the Basin of Stability through Wobble Chair Experiments

6.1 Abstract

Torso stability associated with low back pain has been tested using a variety of different methods. However, the basin of stability for the human torso has not been identified. Knowing the limits of the stable region may provide additional information that could be useful in preventing injury. The aim of this study was to determine this basin of stability from seated stability test data generated in the laboratory. Tests conducted on participants with eyes open and closed showed a significant change in the dimensions of the basin of stability. At the threshold of stability, the basin of stability was found to be larger for eyes closed than eyes open presumably due to larger kinematic variability. In the future, this method may serve as another useful tool to evaluate other balance control problems for which time series data is available.

6.2 Introduction

Low back pain is a common medical ailment afflicting 80% of the population at some time in their life (Kelsey and White 1980; Reeves et al. 2005). A lack of torso stability has often

been considered a contributing factor to low back pain. Torso stability has been evaluated using a variety of different methods including kinematic variability and dynamic stability (Cholewicki et al. 2000; Tanaka and Granata 2007; Granata and Lee 2008). However, many complex systems are not globally stable and contain regions of state space in which stable behavior is exhibited, the basin of stability. Knowledge of the limits of the stable region may be useful in preventing injury. Currently, the basin of stability has not been found for the human torso. The aim of this study was to determine this basin of stability from seated stability test data generated in the laboratory. Unlike the previous tests that evaluated stability only within the stable region of state space, this test analyzes data in both the stable and unstable regions. Torso instability can occur when the level of kinematic variability is able to exceed the basin of stability. In order to provide a thorough understanding of the relationship between kinematic variability and the basin of stability, a discussion of effective potential function, threshold of stability and basin of stability follows.

6.2.1 Basin of Stability and Effective Potential Function Relationship

Spring distance has an effect on both the kinematic variability of the system and the size of the basin of stability. A schematic representation is shown in Figure 6.1. At 100% ∇G, the system is neutrally stable without the controller. When the controller is applied, the system becomes globally stable, meaning the entire state space becomes the basin of stability. In addition, for a given level of perturbations, the kinematic variability is small (~1.8 in Figure 6.1). When the spring distance is decreased to 50% ∇G, the uncontrolled system becomes unstable (dashed line) and the controlled system has locally stable behavior near the origin but is unstable beyond a critical point, q_{cr}. The region within $\pm q_{cr}$ is the basin of stability which is now smaller

than the entire state space. It is also observed that the kinematic variability is larger (~3.8) at 50% ∇G than 100% ∇G for the same level of perturbations.

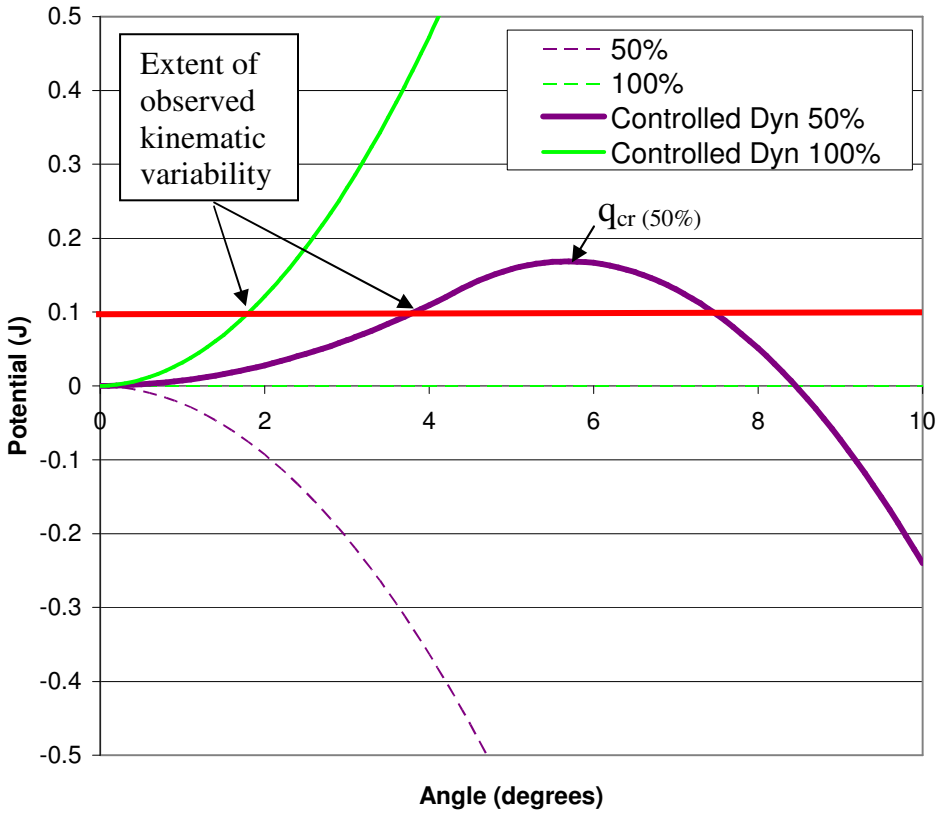

Figure 6.1: Schematic diagram showing the effect of spring setting on the basin of stability and the kinematic variability.

As spring distance decreases, kinematic variability increases and the basin of stability decreases. As long as the basin of stability is larger than the kinematic variability, the controller is able to stabilize the system. However, when the kinematic variability exceeds the basin of stability, conditions may exist that cause the system to become unstable (Figure 6.2). In this case, the basin of stability is still finite, but kinematic variability becomes infinite. With this configuration, the system will exhibit both stable and unstable behavior based on the pattern of

the perturbations applied. The threshold of stability defined in chapter 3 is the spring setting in which stability is maintained throughout test, i.e kinematic variability falls just within the basin of stability.

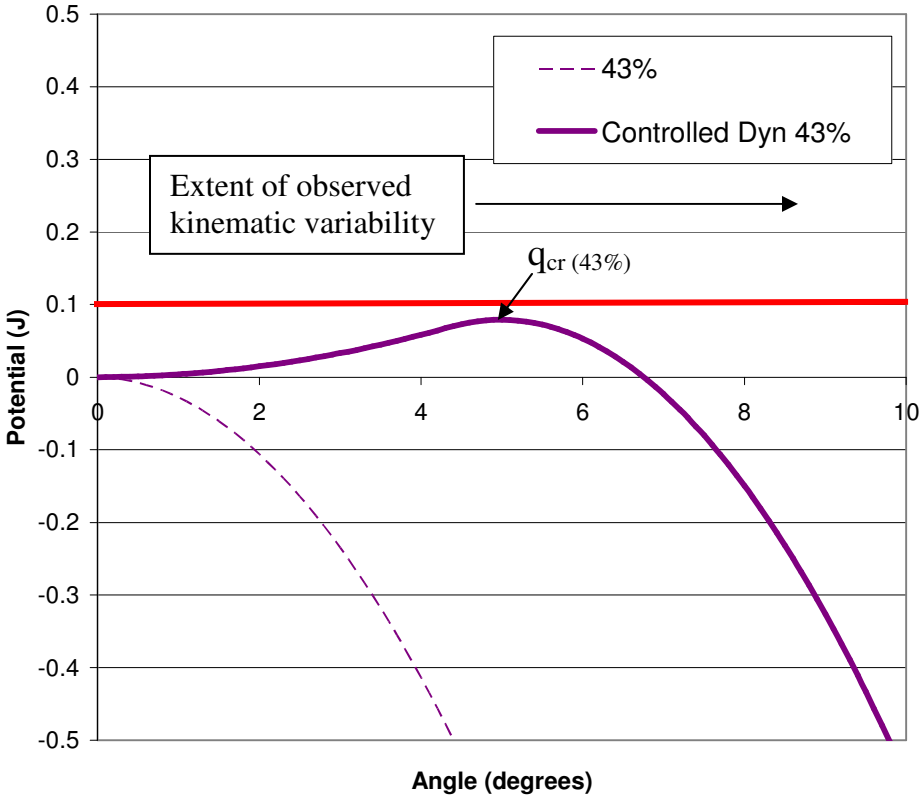

Figure 6.2: When spring distance is reduced to a point where kinetic energy due to random perturbations exceeds effective potential energy, the system can exhibit unstable behavior.

6.2.2 Energy approach to the basin of stability

An energy approach may also be used to develop an understanding of the relationship between kinematic variability and the basin of stability. Systems with random perturbations that are capable of generating kinetic energy that exceeds the maximum effective potential energy,

V_{eff}, of the system may exhibit unstable behavior. V_{eff} is the sum of the potential functions of the system.

The amount of time spent in the stable region verses the unstable region can be theoretically calculated by comparing the probability distribution function (PDF) of the kinetic energy with V_{eff}. Under random perturbations, the PDF for kinetic energy will be centered at zero and have higher energies at lower probabilities. If the tail of the PDF exceeds the energy of the V_{eff}, unstable behavior can occur. Frequency of unstable behavior occurring can be approximated by calculating the area under the upper and lower tails. Note that kinetic energy may exceed potential energy without causing the system to become unstable. This is because major trajectory separations only occur near the ejection point in state space. As a result, if the boundary defining the basin of stability is crossed due to random perturbations it is possible for random perturbations to cause the trajectory to cross back into the stable region since trajectories do not diverge away from the ejection point.

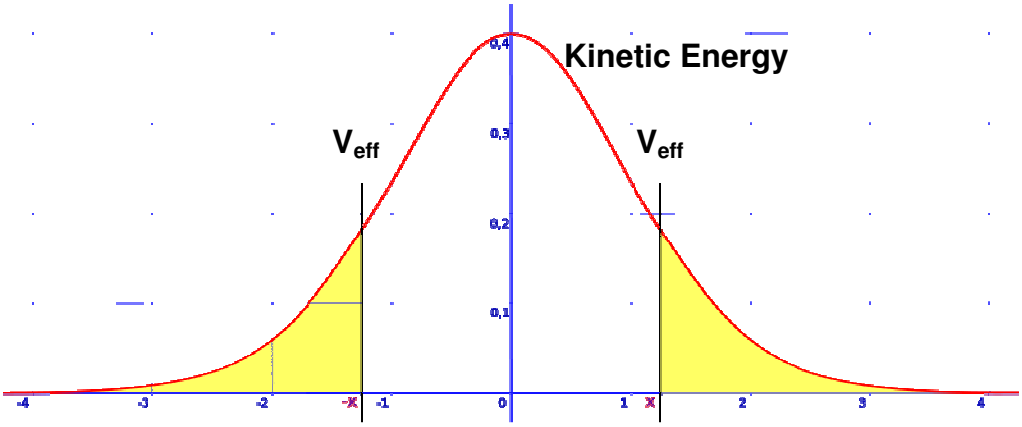

Figure 6.3: When kinetic energy (red) exceeds effective potential energy (black) unstable behavior occurs (http://en.wikipedia.org/wiki/Image:DisNormal06.svg)

6.2.2 Generating both stable and unstable system behavior

It is desirable for analysis to have a substantial amount of data within both stable and unstable regions of state space. If the basin of stability is too small or nonexistent, little or no data will be collected in the stable region. However, if the basin of stability is too large, little or no data will be collected in the unstable region. Ideally, the kinetic energy level generated by random perturbations should slightly exceed the effective potential of the system. Thus, the system will exhibit stable behavior, but given the right combination of perturbations, unstable behavior can be generated.

For a system, there are two ways to achieve this condition; adjust the perturbation level or decrease the effective potential energy of the system. Increasing perturbation amplitudes increases kinetic energy and kinematic variability of the system. However, in human subjects testing, it is often not possible to adjust the perturbation amplitude because it is generated by naturally occurring variability in the neuromuscular system. However, in the testing conducted herein, the effective potential energy of the system is under the control of the experimenter. Since the spring distance contributes to the effective potential by providing restorative torque, altering the spring distance changes the value of the effective potential function.

6.3 Methods

Time series data for this analysis were collected during the study described in chapter 3. Recall that motion sensors were attached to the seat of the wobble chair (Figure 2.1 & 3.1) and back of the participant to record three dimensional angle data. 60 seconds of data were recorded at 100 Hz for each trial. Between trials the anterior and posterior spring distances were changed

to alter task difficulty. The lateral springs were kept at 100% ∇G. This large value of ∇G for the lateral springs made maintaining medial lateral stability easy focusing the motion in the sagittal plane (Figure 6.4).

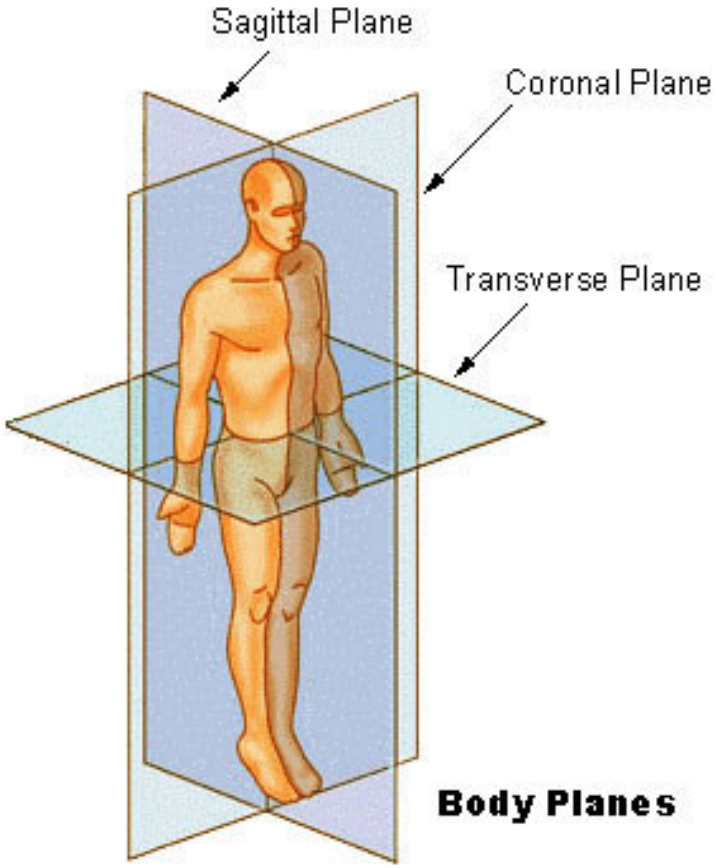

Figure 6.4: Human body planes. During the experimental trials, motion was focused in the sagittal plane (http://en.wikipedia.org/wiki/Core_%28anatomy%29).

The analysis methods used to determine the basin of stability from simulated experimental data in chapter 5 were applied to the time series data collected during the study (chapter 3). Trials of interest were those one increment (5%∇G) smaller than the threshold of

stability. These trials had data in both the stable and unstable regions of state space. The size of the basin was measured in four dimensions from the Poincaré sections and the volume of a 4D bounding box (the representing the basin of stability) was calculated.

6.4 Results

Of the eight participants tested, subject three showed the most consistency for any particular test condition. For the eight tests with eyes open, this participant consistently alternated levels passing each time at 35%∇G and failing each time at 30%∇G. Because of this consistency, these four replicated trials at 30%∇G were selected for the initial analysis. Two dimensional slices of the basin of stability were calculated using Poincaré sections which are described earlier in this dissertation (section 5.4). Initially no structure was visible, but structure became noticeable when very thin slices were used. Figure 6.5 shows the zero velocity plot which was constructed by selecting values of $\dot{\theta}_1$ and $\dot{\theta}_2$ that lie within 0.01% of the data range. This Poincaré section included 2.7% of the data points. A basin of stability was noticeable near the origin in state space (0, 0, 0, 0) and showed some alignment with the equilibrium manifold predicted by the mathematical model in chapter 5 (section 5.4.2). The size of the basin was approximately 4 degrees in θ_1 and 3 degrees in θ_2.

The (θ_1, $\dot{\theta}_1$) slice of state space was constructed by selecting values of θ_2 and $\dot{\theta}_2$ that lie within 0.01% of the data range (Figure 6.6). In the plot, a basin of stability was noticeable near the origin in state space (0, 0, 0, 0). Furthermore, the size and shape of the basin matched well with the size and shape generated from trajectory data (see chapter 5 for details). The size of the basin was spanned a range of approximately 4 degrees in θ_1 and 8 degrees/s in $\dot{\theta}_1$.

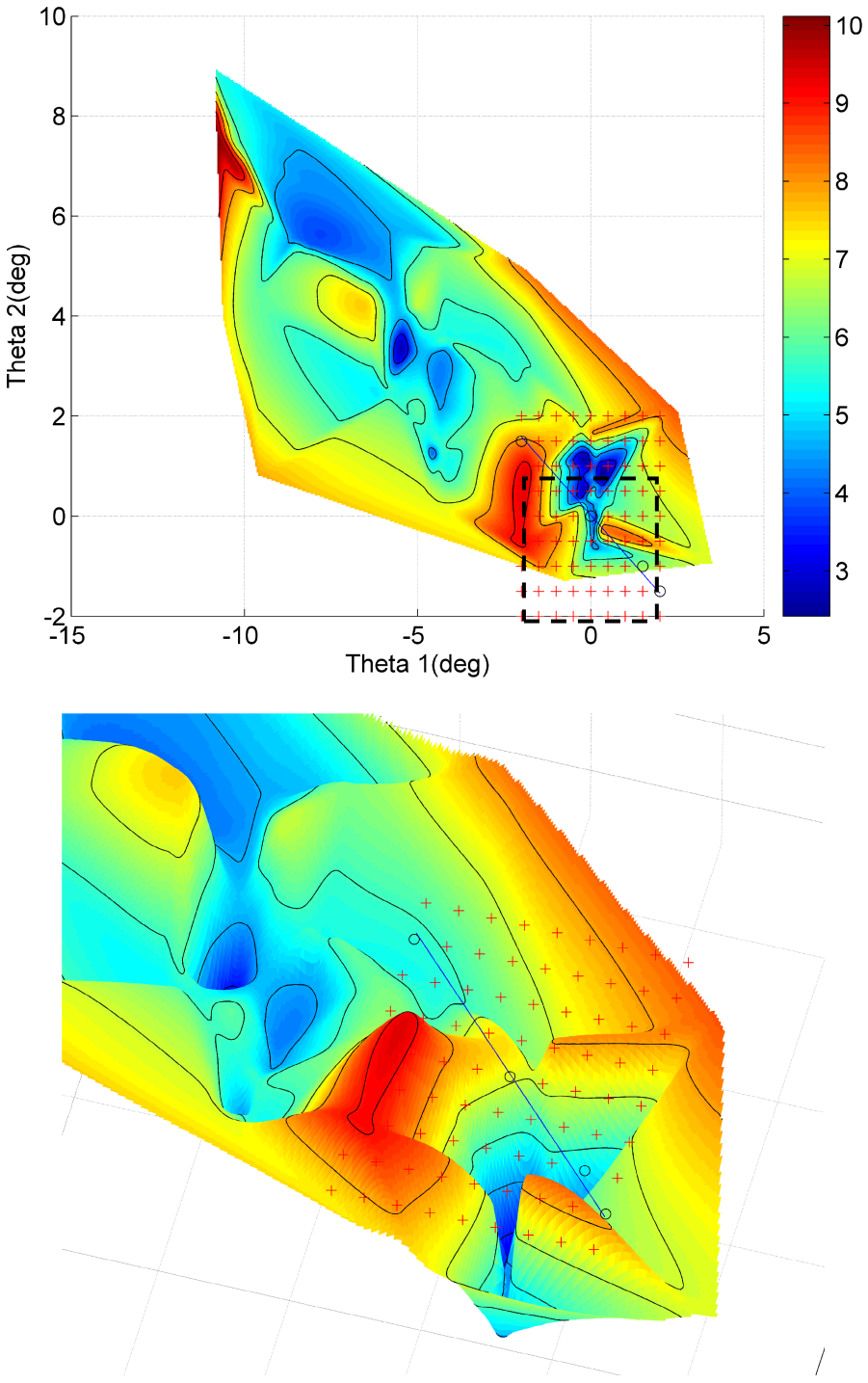

Figure 6.5: FTLE field for participant #3 with eyes open generated using state transition matrix method. This two dimensional plot shows the zero velocity section of the four dimensional system. A bounding box was drawn (black dashed lines) to approximate the dimensions of the basin of stability.

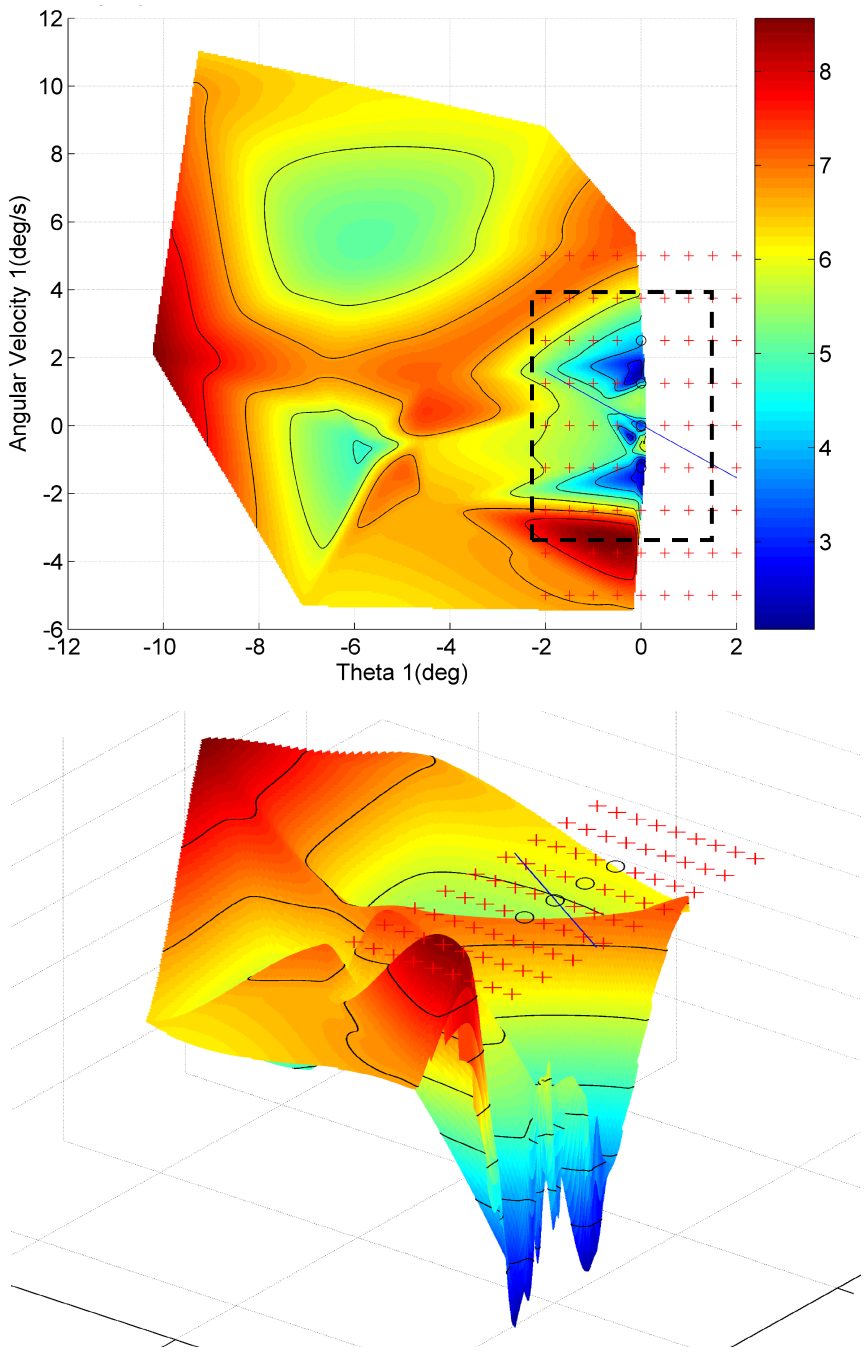

Figure 6.6: FTLE field for participant #3 with eyes open generated using the state transition matrix method. This two dimensional plot shows phase space of θ_1. A bounding box was drawn (black dashed lines) to approximate the dimensions of the basin of stability.

The $(\theta_2, \dot{\theta}_2)$ slice of state space was constructed by selecting values of θ_1 and $\dot{\theta}_1$ that lie within 0.01% of the data range (Figure 6.7). In the plot, a basin of stability was noticeable near

the origin in state space (0, 0, 0, 0). Furthermore, the size of the basin was similar to the size generated from trajectory data, but the shape was different. The size of the basin was approximately 4 degrees in θ_2 and 10 degrees/s in $\dot{\theta}_2$.

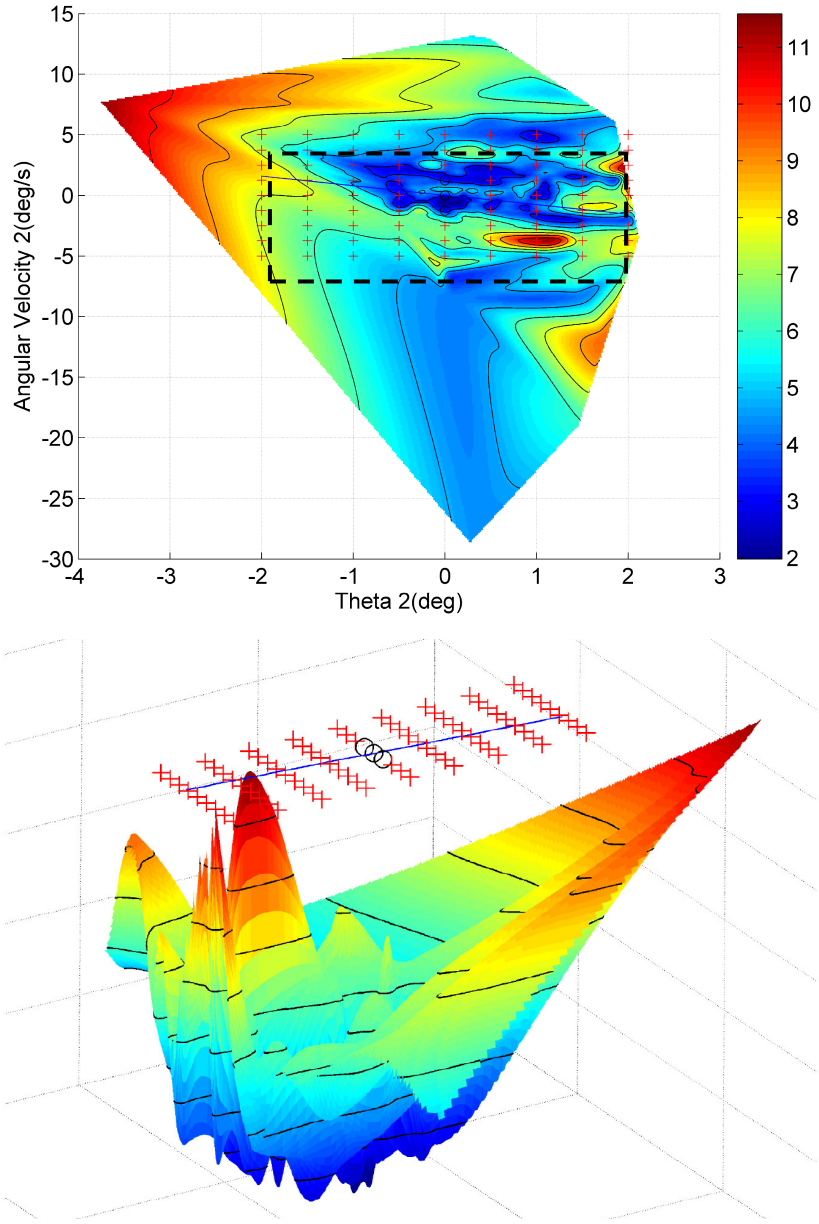

Figure 6.7: FTLE field for participant #3 with eyes open generated using the state transition matrix method. This two dimensional plot shows the phase space of θ_2. A bounding box was drawn (black dashed lines) to approximate the dimensions of the basin of stability.

The volume of the basin of stability, V_{BOS}, was approximated by a 4-dimensional rectangular solid,

$$V_{BOS} = \theta_1\Big|_{\min}^{\max} \times \theta_2\Big|_{\min}^{\max} \times \dot{\theta}_1\Big|_{\min}^{\max} \times \dot{\theta}_2\Big|_{\min}^{\max} \qquad (6.1)$$

where each of the four θ parameters is the length of the basin of stability in that state space direction. In this case, V_{BOS} was 1280 degrees^4/s^2 (4°x 4°x 10°/s x 8°/s). Since θ_1 and θ_2 were shown in more than one plot, the best view of the LCS was used to determine the dimension of the basin of stability in this direction.

For the eyes shut condition, only two trials were available for subject three. A data range of 0.01% was used for the (θ_1, θ_2) (Figure 6.8) and (θ_1, $\dot{\theta}_1$) slices of state space (Figure 6.10). The (θ_2, $\dot{\theta}_2$) slices of state space (Figure 6.9) yielded almost no data at a data range of 0.01%, so the range was increased until a surface was visible (0.03%). The ranges for θ_1, θ_2, $\dot{\theta}_1$, $\dot{\theta}_2$ were estimated to be 5 degrees, 6 degrees, 10 degrees/s, 10 degrees/s, respectively. Applying equation [6.1], the V_{BOS} was calculated to be 3000 degrees^4/s^2.

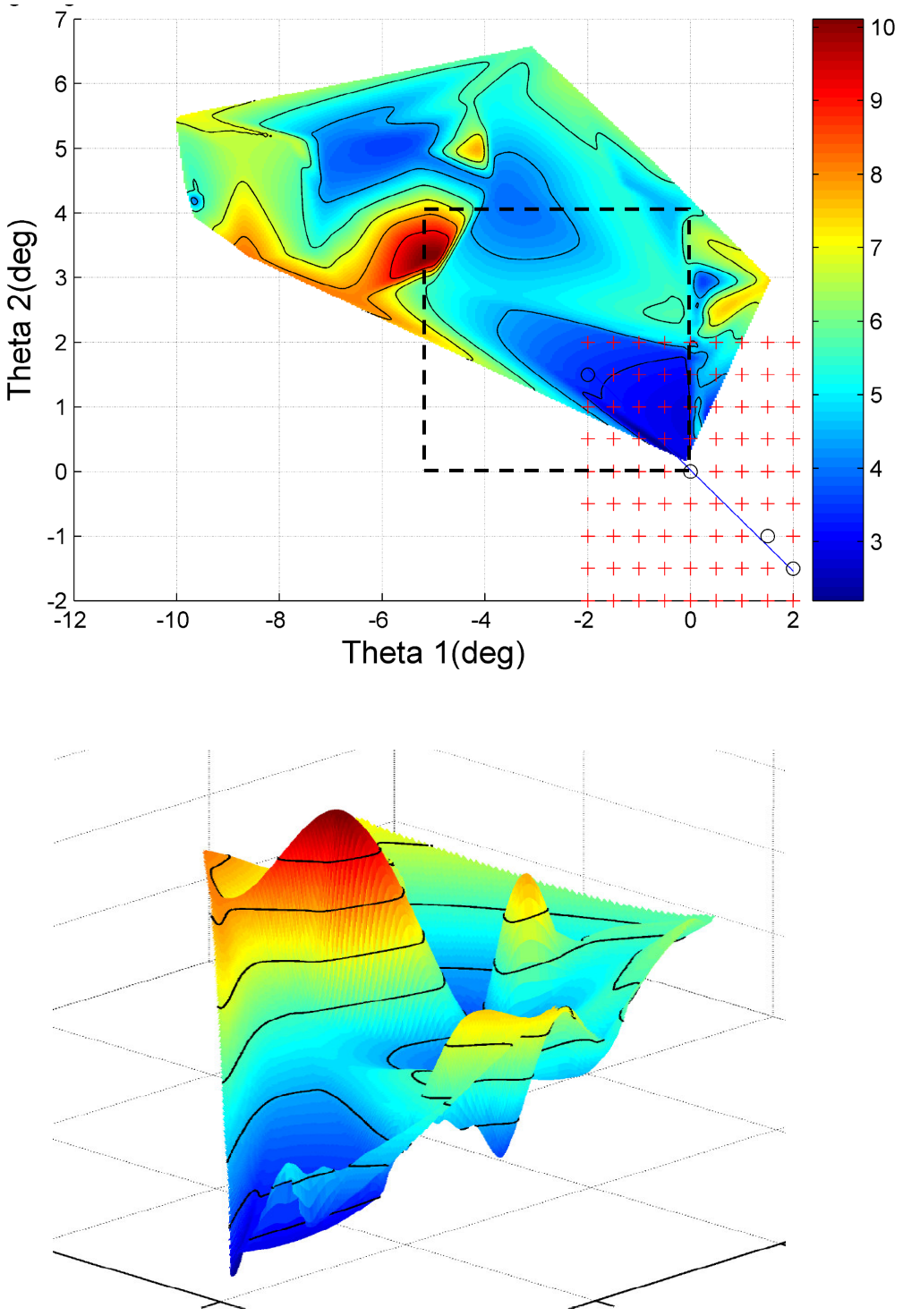

Figure 6.8: FTLE field for participant #3 with eyes shut generated using the state transition matrix method. This two dimensional plot shows the zero velocity section of the four dimensional system. The bounding box drawn (black dashed lines) to approximates ¼ of the basin of stability. The full basin is assumed to by symmetric with respect of the origin in $\theta_1$and θ_2.

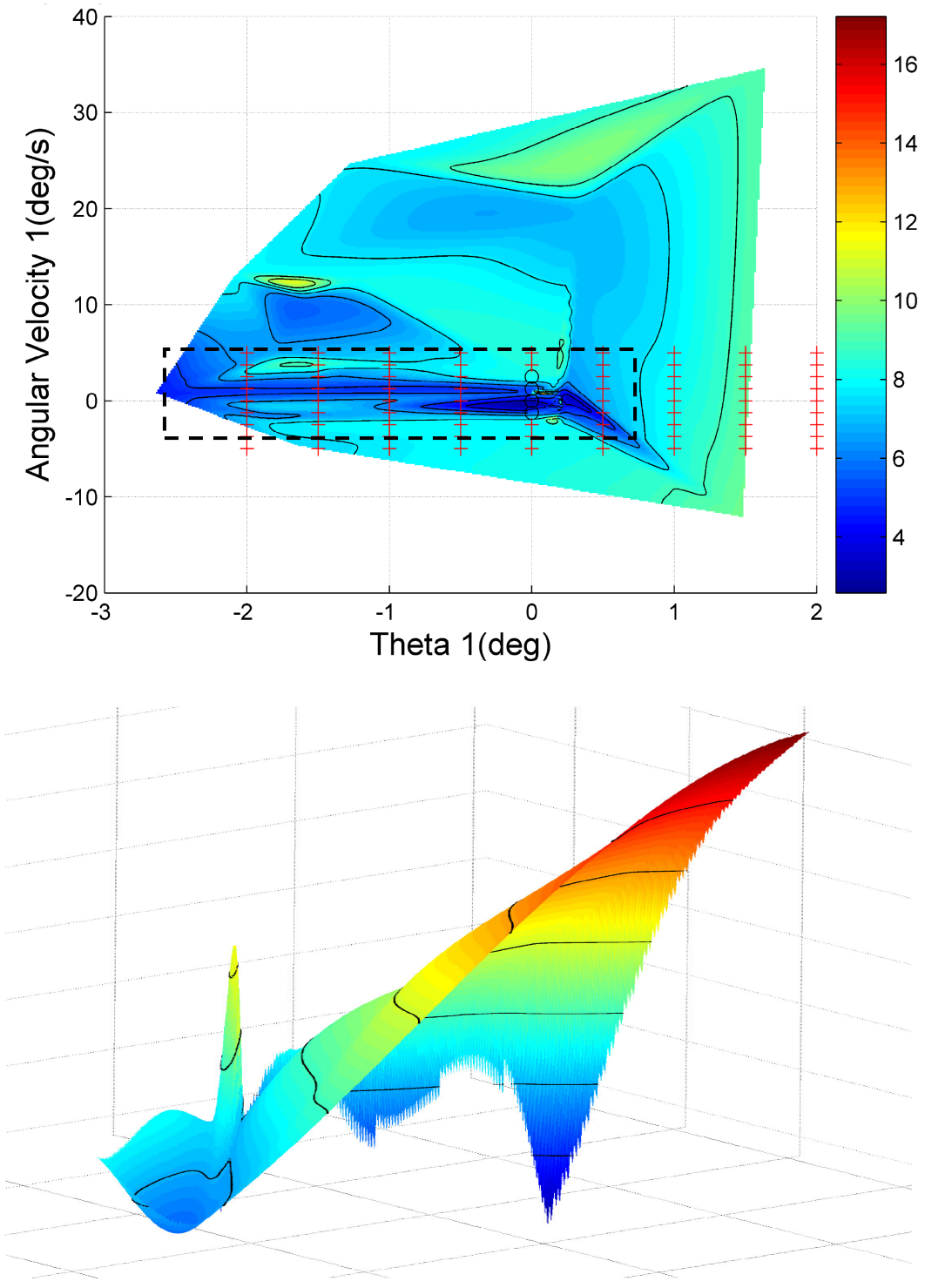

Figure 6.9: FTLE field for participant #3 with eyes shut generated using the state transition matrix method. This two dimensional plot shows the phase space of θ_1.

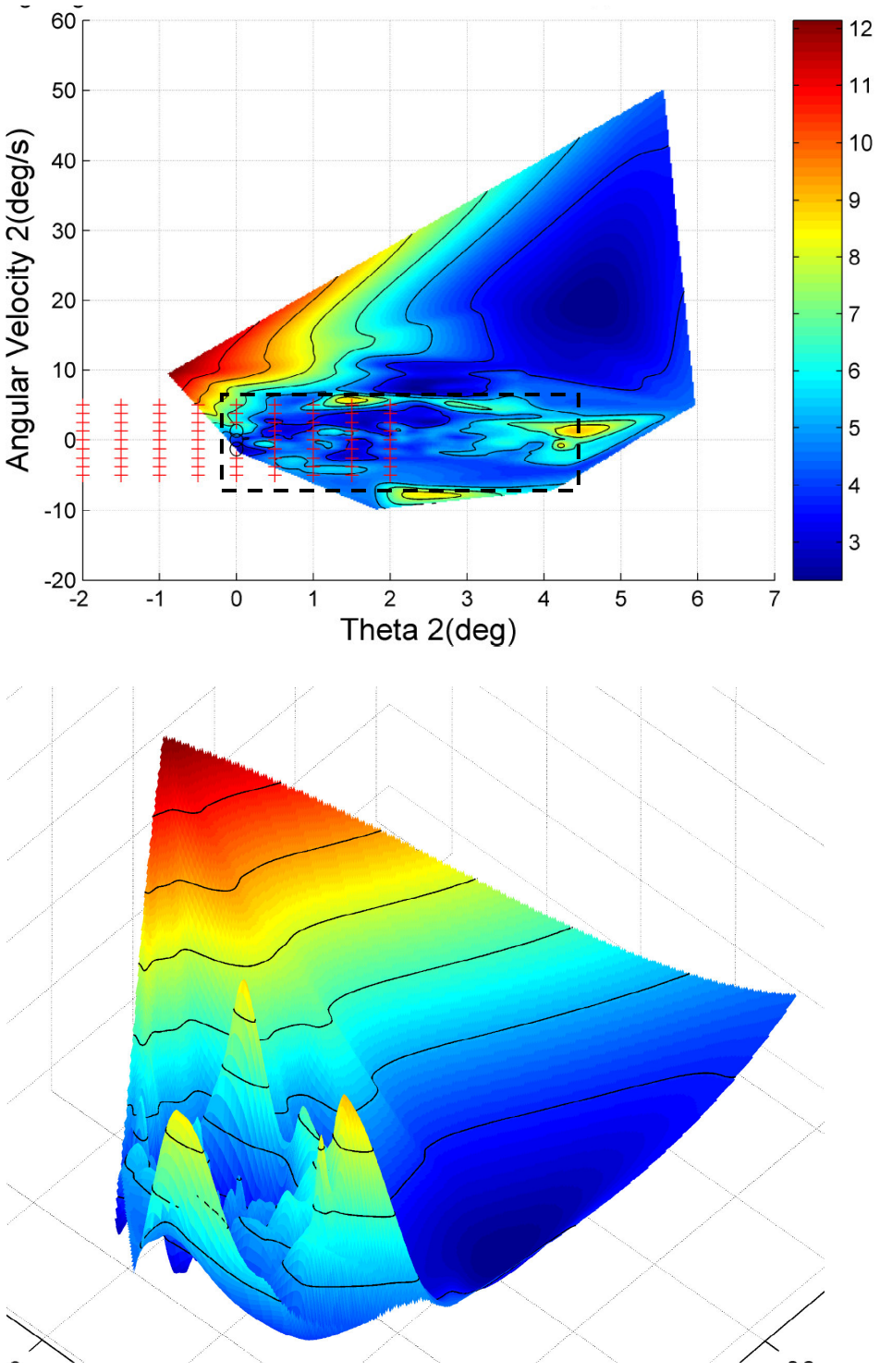

Figure 6.10: FTLE field for participant #3 with eyes shut generated using the state transition matrix method. This two dimensional plot shows the phase space of θ_2.

The basin of stability was determined for each condition and subject using the process above. Results are shown in the table below (Table 6.1).

Table 6.1: Basin of stability volume

Participant	Eyes Open					Eyes Closed				
	θ_1 range (deg)	$\dot{\theta}_1^*$ range (deg/s)	θ_2 range (deg)	$\dot{\theta}_2$ range (deg/s)	4D volume* (deg^4/s^2)	θ_1 range (deg)	$\dot{\theta}_1^*$ range (deg/s)	θ_2 range (deg)	$\dot{\theta}_2$ range (deg/s)	4D volume* (deg^4/s^2)
1	6	4	4	4	384	6	6	8	10	2880
2	6	6	8	8	2304	6	6	9	15	4860
3	4	4	10	8	1280	5	6	10	10	3000
4	5	6	8	12	2880	8	7	7	15	5880
5	8	4	15	12	5760	6	12	8	20	11520
6	6	3	10	10	1800	9	5	15	10	6750
7	2	3	3	14	252	6	7	5	15	3150
8	4	6	3	40	2880	8	7	2	10	1120

* indicates significant

A paired t-test was conducted to determine if differences in parameters were detected between test performed with and without visual feedback. A value of $\alpha = 0.05$ was used as the criterion for significance. The seat angular velocity, $\dot{\theta}_1$, (mean difference = 2.5; p = 0.026) and the 4D volume (mean difference = 2700; p = 0.012) were found to be statistically different using a paired t-test. Seat angle, θ_1, (mean difference = 1.63; p = 0.075) also tended to increase with the eyes closed, however no significant difference was found. Torso angle, θ_2, (mean difference = .38; p = 0.78) and torso angular velocity, $\dot{\theta}_2$, (mean difference = -.38; p = 0.93) were generally invariant to changes in test condition.

6.5 Discussion

The 4-dimensional volume of the basin of stability was significantly larger with eyes closed than eyes open when tested just beyond the threshold of stability for each condition. Changes in angle and angular velocity of the lower body caused this difference. This is consistent with experimental observations which showed seat angle to be the dominant segment used by the participant to control balance. A larger basin of stability for eyes closed may be explained by considering the effect of visual feedback on balance control. In general, feedback to a controller will improve performance by allowing more precise application of the control torques. In contrast, a lack of feedback can result in poor timing of control torque, incorrect application of torque direction, and system drift. All of these factors lead to an increase in kinematic variability of the system. Recall that when kinematic variability exceeds the basin of stability, the system becomes unstable. At the threshold of stability, the increased kinematic variability caused by lack of visual feedback must be matched with a larger basin of stability. The lack of feedback control can also explain the changes in seat angle and angular velocity. Inferior performance of the balance control system (predominantly driven by the lower body) leads to non-optimal trajectories. Control error can cause the system to deviate from equilibrium by larger angles which then require higher velocities to recover stability. These factors can contribute to larger angles and angular velocities and ultimately a larger basin of stability at the threshold of stability.

One limitation of this method is the often ambiguous shape of the basin of stability and the subjective determination of its size. Thus, accuracy and repeatability of the method may not be good for some experiments. However, large differences were measured in the θ_1 directions of state space while virtually no difference was measured in the θ_2 state space directions. Since the

researcher was “blind” to the implications of directions differences, some of the subjective nature of these measurements was removed. Thus, it is encouraging that such significant differences between the state space directions were observed and explainable.

6.6 Summary and Conclusions

This method effectively showed that a basin of stability can be generated from time series data collected from biomechanics experiments. Finite time Lyapunov exponent (FTLE) fields were generated using the state transition matrix method. Within these FTLE fields, LCSs were found identifying the boundary of the basin of stability. At the threshold of stability, the basin of stability was found to be larger for eyes closed than eyes open presumably due to larger kinematic variability. In the future, this method may serve as another useful tool to evaluate other balance control problems for which time series data is available.

Chapter 7

Summary and Conclusions

7.1 Research Summary and Contributions

A series of related studies were performed in order to improve the understanding of torso instability, a factor often associated with low back pain. The first study examined torso stability using time series averaged finite time Lyapunov exponents (FTLE). This was an application of an existing method to a new problem. It was found that differences in spring distance (i.e. task difficulty) were detectable using this method. In addition, the FTLE was found to be repeatable when subjects were retested one week later.

The next study was an experiment designed to assess the sensitivity of a new metric, the threshold of stability. This new metric is interesting because it evaluates the limits of stability rather then the variability or trends of a stable system. It requires no electronics and is easy to administer the test. A significant difference was found between participants with and without visual feedback showing the method to be sensitive to differences in balance control with only eight participants. Due to the simplicity and sensitivity of this method, it may be suitable for assessment of low back pain in a clinical setting.

In order to better understand the experimental work, mathematical models were developed for the human torso. Initially a reduced model was created so that methods could be developed to evaluate the state space distribution of the FTLE. Although the state space distribution of the FTLE had been evaluated for other engineering systems, it had not been applied to biomechanics or time series data in general. Lagrangian coherent structures were found in the FTLE field showing the location of separatrices in the trajectory paths. Furthermore, the basin of stability was found for the deterministic system. As a step toward being able to apply this method to time series data similar to that collected in chapter 3, methods were developed to find LCS from time series data. To the authors knowledge this is the first application of LCS to time series data in the absence of a vector field.

Next the reduced model was extended to develop a model of the wobble chair. Anthropometric data was used to calibrate the model, but initially, a stable controller could not be found. This problem was overcome by investigating the Acrobot, a system with similar but inherently more stable dynamics. After first finding controller parameters for the Acrobot, a morphing technique was used to find controller parameters that stabilized the wobble chair. An addition benefit of the assessment of the Acrobot was that it provided clues which aided in the discovery of an unknown parameter for the wobble chair, the equilibrium manifold. Extending the methods developed for the reduced model, the FTLE field was created and LCS were found. Basins of stability for the deterministic simulation of the wobble chair model matched well with those created by evolving trajectories form various initial states. However, the stochastic simulation failed to match well with trajectory data. Perhaps this was because the basin of stability was small using the stable linear control which was found. As a result there may have been an inadequate signal to noise ratio to effectively define the edge of the basin.

Finally, the methods developed using simulated experimental data were applied to real experimental data obtained from wobble chair experiments. Using the state transition matrix method for finding the FTLE field, structure was noticeable near the origin in 4D state space. For the first time, the dimensions of the basin of stability were determined in each state space direction along with the total volume. Results showed the basin of stability to be larger (at the threshold of stability) for eyes closed than open. This result may be explained by a larger amount of kinematic variability for the eyes closed condition leading to a larger basin of stability at the threshold of stability (see section 6.5 for a full discussion). The location of the LCS was often difficult to identify which made finding the basin of stability somewhat subjective. However, statistically significant and logically explainable results were obtained even with these challenges.

Evaluating the state space distribution of the FTLE led to insight that was not intuitively available using existing method that produces a scalar value. One unexpected finding was the existence of a one-dimensional equilibrium manifold to which stable trajectories were clustered around rather than a single equilibrium point.

7.2 Future Work

A trend was observed in the experiments toward failing in the backward direction, although an insufficient amount of data was collected to quantify these results. This is interesting because it was also predicted by the wobble chair model. This prediction was probably due to asymmetry about the central ball joint. In a future study, the number of forward and backward falls could be counted to see if a significant difference exists. It may also be

possible to correlate the results with clinical data for LBP patients to determine if the same ratio exists for tissue injury presumably caused the forward, backward, or lateral instability. This information may be useful to determining how people carry loads on the back.

Different controllers could be evaluated to determine if the actual human response could be predicted. These controllers could include non-linear feedback gain, time delay, and gain limitations. If an accurate model for the torso could be developed, simulations could be performed to evaluate expensive or possibly dangerous scenarios such as the effects of large inertial loads on the human torso during space flight, optimization of ejection seat performance, or determination of critical torso loading.

Finally, the methods presented herein could be extended to other areas of biomechanics such as standing postural sway, fall prevention, gait analysis, or evaluation of sports movements. Furthermore, there may be applications outside of biomechanics such as analysis of robot movements, vehicle controls, or other time series phenomenon.

LITERATURE CITED

Adams M (2007) Re: Spine stability: the six blind men and the elephant. Clin Biomech (Bristol, Avon) 22: 486; author reply 487-488

Adams MA, Dolan P (1995) Recent advances in lumbar spinal mechanics and their clinical significance. Clin Biomech (Bristol, Avon) 10: 3-19

Akay M (2006) Wiley encyclopedia of biomedical engineering. Wiley-Interscience, Hoboken, N.J.

Aldridge B, Haller G, Sorger P, Lauffenburger D (2006) Direct Lyaponov exponent analysis enables parametric study of transient signalling governing cell behaviour. IEE Proc. Syst. Biol.: 425--432

Ashby WR (1962) Principles of the Self-organizing system Pergamon Press, New York

Benettin G, Galgani L, Giorgilli A, Strelcyn J (1980a) Lyapunov Characteristic Exponents for smooth dynamical systems and for hamiltonian systems; a method for computing all of them. Part 1: Theory. Meccanica 15: 9–20

Benettin G, Galgani L, Giorgilli A, Strelcyn J (1980b) Lyapunov exponents for smooth dynamical systems and Hamiltonian systems; a method for computing all of them, Part II: Numerical application. Meccanica: 21–30

Bergmark A (1989) Stability of the lumbar spine. A study in mechanical engineering. Acta Orthop Scand Suppl 230: 1-54

Boone G (1997) Minimum-time Control of the Acrobot International Conference on Robotics and Automation, Albuquerque, New Mexico, pp 3281-3287

Bortoff S (1992) Pseudolinearization Using Spline Functions With Application to the Acrobot. Department of Electrical and Computer Engineering, Urbana-Champaign

Brown R, Bryant P, Abarbanel HDI (1991) Computing the Lyapunov spectrum of a dynamical system from an observed time series. Physical Review A 43: 2787

Brown SH, McGill SM (2005) Muscle force-stiffness characteristics influence joint stability: a spine example. Clin Biomech (Bristol, Avon) 20: 917-922

Cailliet R (2003) Low Back Disorders a Medical Enigma

Casdagli M, Eubank S, Farmer JD, Gibson J (1991) State-Space Reconstruction in the Presence of Noise. Physica D 51: 52-98

Cholewicki J, McGill SM (1996) Mechanical stability of the in vivo lumbar spine: implications for injury and chronic low back pain. Clin Biomech (Bristol, Avon) 11: 1-15

Cholewicki J, Polzhofer GK, Radebold A (2000) Postural control of trunk during unstable sitting. J Biomech 33: 1733-1737

Collins JJ, De Luca CJ (1993) Open-loop and closed-loop control of posture: a random-walk analysis of center-of-pressure trajectories. Exp Brain Res 95: 308-318

de Leva P (1996) Adjustments to Zatsiorsky-Seluyanov's segment inertia parameters. Journal of Biomechanics 29: 1223-1230

Delignieres D, Deschamps T, Legros A, Caillou N (2003) A methodological note on nonlinear time series analysis: is the open- and closed-loop model of Collins and De Luca (1993) a statistical artifact? J Mot Behav 35: 86-97

Dingwell JB, Cusumano JP (2000) Nonlinear time series analysis of normal and pathological human walking. Chaos 10: 848-863

Dingwell JB, Cusumano JP, Sternad D, Cavanagh PR (2000) Slower speeds in patients with diabetic neuropathy lead to improved local dynamic stability of continuous overground walking. J Biomech 33: 1269-1277

Eckmann JP, Kamphorst SO, Ruelle D, Ciliberto S (1986) Liapunov Exponents from Time-Series. Physical Review A 34: 4971-4979

Edwards WT (2001) Comments on "Predicted region of stability for balance recovery: motion at the knee joint can improve termination of forward movement". J Biomech 34: 831-833

Einstein A (1905) Investigations on the theory of, the Brownian movement (translated to English)

El Rifai K, Haller G, Bajaj AK (2007) Global dynamics of an autoparametric spring-mass-pendulum system. Nonlinear Dynamics 49: 105-116

Ellner S, Turchin P (1995) Chaos in a Noisy World - New Methods and Evidence from Time-Series Analysis. American Naturalist 145: 343-375

England SA, Granata KP (2006) The influence of gait speed on local dynamic stability of walking. Gait Posture

England SA, Granata KP (2007) The influence of gait speed on local dynamic stability of walking. Gait Posture 25: 172-178

Evans DJ, Cohen EGD, Morriss GP (1990) Viscosity of a simple fluid from its maximal Lyapunov exponents. Physical Review A 42: 5990

Falconer I, Gottwald GA, Melbourne I, Wormnes K (2007) Application of the 0-1 test for chaos to experimental data. Siam Journal on Applied Dynamical Systems 6: 395-402

Franca LFP, Savi MA (2001) Distinguishing periodic and chaotic time series obtained from an experimental nonlinear pendulum. Nonlinear Dynamics 26: 253-271

Fung Y (1993) Biomechanics: Mechanical Properties of Living Tissues. Springer-Verlag, New York

Galukande M, Muwazi S, Mugisa BD (2006) Disability associated with low back pain in Mulago Hospital, Kampala Uganda. Afr Health Sci 6: 173-176

Garcia M, Chatterjee A, Ruina A, Coleman M (1998) The simplest walking model: Stability, complexity, and scaling. Journal of Biomechanical Engineering-Transactions of the Asme 120: 281-288

Gates DH, Dingwell JB (2007) Peripheral neuropathy does not alter the fractal dynamics of stride intervals of gait. J Appl Physiol 102: 965-971

Goswami A (1996) Limit cycles and their stability in a passive biped gait International conference on Robotics and Automation, Minneapolis, MN, pp 246-251

Granata K, Lee H (2008) Process Stationarity and Reliability of Trunk Postural Stability. Clinical Biomechanics - *Submitted 8 January 2007

Granata KP, England SA (2006) Stability of dynamic trunk movement. Spine 31: E271-276

Granata KP, Orishimo KF (2001) Response of trunk muscle coactivation to changes in spinal stability. J Biomech 34: 1117-1123

Granata KP, Tanaka M, Slota G, Lee HW (2006) Effects of level of static stability on metabolic consumption of oxygen

Haller G (2000) Finding finite-time invariant manifolds in two-dimensional velocity fields. Chaos 10: 99-108

Haller G (2001a) Distinguished material surfaces and coherent structures in three-dimensional fluid flows. Physica D 149: 248-277

Haller G (2001b) Lagrangian structures and the rate of strain in a partition of two-dimensional turbulence. Physics of Fluids 13: 3365-3385

Haller G (2002) Lagrangian coherent structures from approximate velocity data. Physics of Fluids 14: 1851-1861

Haller G, Yuan G (2000) Lagrangian coherent structures and mixing in two-dimensional turbulence. Physica D-Nonlinear Phenomena 147: 352-370

Hauser J, Murray R (1990) Nonlinear controllers for non-integrable systems: the Acrobot example American Control Conference, San Diego, California, pp 669-671

Haynes P (2005) Stratospheric dynamics. Annual Review of Fluid Mechanics 37: 263-293

Hou Y, Luecke G (2003) Control of the Tight Rope Balancing Robot International Symposium on Intelligent Control, Houston, Texas, pp 896-901

Iqbal K, Pai Y (2000) Predicted region of stability for balance recovery: motion at the knee joint can improve termination of forward movement. J Biomech 33: 1619-1627

Jury EI (1996) Remembering four stability theory pioneers of the nineteenth century. Ieee Transactions on Automatic Control 41: 1242-1244

Kang HG, Dingwell JB (2006) A direct comparison of local dynamic stability during unperturbed standing and walking. Exp Brain Res 172: 35-48

Kantz H, Schreiber T (2004) Nonlinear Time Series Analysis. Cambridge University Press

Kelsey JL, White AA, 3rd (1980) Epidemiology and impact of low-back pain. Spine 5: 133-142

Kent PM, Keating JL (2005) The epidemiology of low back pain in primary care. Chiropr Osteopat 13: 13

Kuo AD, Zajac FE (1993) A biomechanical analysis of muscle strength as a limiting factor in standing posture. J Biomech 26 Suppl 1: 137-150

Lapeyre G (2002) Characterization of finite-time Lyapunov exponents and vectors in two-dimensional turbulence. Chaos 12: 688-698

Lekien F, Shadden SC, Marsden JE (2007) Lagrangian coherent structures in n-dimensional systems. Journal of Mathematical Physics 48: -

Loney PL, Stratford PW (1999) The prevalence of low back pain in adults: a methodological review of the literature. Phys Ther 79: 384-396

Lucas D, Bresler B (1961) Stability of the Ligamentous Spine

Mandelbrot BB, Van Ness JW (1968) Fractional Brownian Motions, Fractional Noises and Applications. SIAM Review Vol. 10: pp. 422-437

Mccue L, Troesch A (2006) A combined numerical-empirical method to calculate finite-time Lyapunov exponents from experimental time series with application to vessel capsizing. Ocean Engineering 33: 1796-1813

Mcgeer T (1990) Passive Dynamic Walking. International Journal of Robotics Research 9: 62-82

McGill SM (2001) Low back stability: from formal description to issues for performance and rehabilitation. Exerc Sport Sci Rev 29: 26-31

MedlinePlus (2007) Back pain - low : Medical Encyclopedia. MedlinePlus

Morasso PG, Sanguineti V (2002) Ankle muscle stiffness alone cannot stabilize balance during quiet standing. J Neurophysiol 88: 2157-2162

Murray R, Hauser J (1991) A Case Study on Approximate Linearization: The Acrobot Example. Electronics Research Loaboatory, College of Engineering, University of California, Berkeley, Berkeley, California

NINDS (2007) Low Back Pain Fact Sheet National Institute of Neurological Disorders and Stroke

Okushima T (2003) New Method for Computing Finite-Time Lyapunov Exponents. Physical Review Letters 91: 254101

Pai YC, Patton J (1997) Center of mass velocity-position predictions for balance control. J Biomech 30: 347-354

Peterka RJ (2000) Postural control model interpretation of stabilogram diffusion analysis. Biol Cybern 82: 335-343

Pierrehumbert RT (1991a) Chaotic mixing of tracer and vorticity by modulated travelling Rossby waves. Geophys. Astrophys. Fluid Dynamics 58: 285--319

Pierrehumbert RT (1991b) Large-Scale Horizontal Mixing in Planetary-Atmospheres. Physics of Fluids a-Fluid Dynamics 3: 1250-1260

Preuss R, Fung J (2005) Can acute low back pain result from segmental spinal buckling during sub-maximal activities? A review of the current literature. Man Ther 10: 14-20

Radebold A, Cholewicki J, Polzhofer GK, Greene HS (2001) Impaired postural control of the lumbar spine is associated with delayed muscle response times in patients with chronic idiopathic low back pain. Spine 26: 724-730

Reeves NP, Cholewicki J, Milner TE (2005) Muscle reflex classification of low-back pain. J Electromyogr Kinesiol 15: 53-60

Reeves NP, Cholewicki J, Narendra KS (2007a) Reply. Clin Biomech (Bristol, Avon) 22: 487-488

Reeves NP, Everding VQ, Cholewicki J, Morrisette DC (2006) The effects of trunk stiffness on postural control during unstable seated balance. Exp Brain Res 174: 694-700

Reeves NP, Narendra KS, Cholewicki J (2007b) Spine stability: the six blind men and the elephant. Clin Biomech (Bristol, Avon) 22: 266-274

Rosenstein MT, Collins JJ, De Luca CJ (1993a) A practical method for calculating largest Lyapunov exponents from small data sets65: 117-134

Rosenstein MT, Collins JJ, Deluca CJ (1993b) A Practical Method for Calculating Largest Lyapunov Exponents from Small Data Sets. Physica D 65: 117-134

Sall J, Lehman A (1996) JPM Start Statistics. Wadsworth Publishing Co., Belmont, Ca

Sano M, Sawada Y (1985) Measurement of the Lyapunov Spectrum from a Chaotic Time Series. Physical Review Letters 55: 1082

Schmitt j (2006) A Simple Stabilizing Control for Sagittal Plane Locomotion. Journal of Computational and Nonlinear Dynamics vol. 1: pp. 348-357

Shadden SC, Lekien F, Marsden JE (2005) Definition and properties of Lagrangian coherent structures from finite-time Lyapunov exponents in two-dimensional aperiodic flows. Physica D-Nonlinear Phenomena 212: 271-304

Smirnov VI (1992) Biography of Lyapunov,A.M. International Journal of Control 55: 775-784

Spong MW (1995) The Swing up Control Problem for the Acrobot. Ieee Control Systems Magazine 15: 49-55

Stokes IA, Gardner-Morse M (2001) Lumbar spinal muscle activation synergies predicted by multi-criteria cost function. J Biomech 34: 733-740

Strang G (1998) Linear Algebra and its Applications. Harcourt Brace Jovanovich, San Diego

Tanaka ML, Granata KP (2007) Methods & Nonlinear Analysis for Measuring Torso Stability ASCE 18th Engineering Mechanics Division Conference, Blacksburg, VA

Truesdell C, Noll W (2004) The Non-Linear Field Theories of Mechanics. Springer-Verlag, Berlin-Heidelberg-New York

Van Dieen JH, Cholewicki J, Radebold A (2003) Trunk muscle recruitment patterns in patients with low back pain enhance the stability of the lumbar spine. Spine 28: 834-841

Vastano JA, Moser RD (1991) Short-Time Lyapunov Exponent Analysis and the Transition to Chaos in Taylor-Couette Flow. Journal of Fluid Mechanics 233: 83-118

Wang Y, Haller G, Banaszuk A, Tadmor G (2003) Closed-loop Lagrangian separation control in a bluff body shear flow model. Physics of Fluids 15: 2251-2266

Wessel N, Meyerfeldt U, Schirdewan A, Kurths J, Voss A (1998) Short-term forecasting of life-threatening arrhythmias with finite time Lyapunov exponents, pp 326-329 vol.321

Winter D (1990) Biomechanics and motor control of human movement Biomechanics and motor control of human movement, pp 141-154

Winter DA, Patla AE, Rietdyk S, Ishac MG (2001) Ankle muscle stiffness in the control of balance during quiet standing. J Neurophysiol 85: 2630-2633

Wolf A, Swift JB, Swinney HL, Vastano JA (1985) Determining Lyapunov exponents from a time series. Physica D: Nonlinear Phenomena 16: 285-317

Yang CX, Wu Q (2006) On stabilization of bipedal robots during disturbed standing using the concept of Lyapunov exponents. Robotica 24: 621-624

Yoden S, Nomura M (1993) Finite-Time Lyapunov Stability Analysis and Its Application to Atmospheric Predictability. Journal of the Atmospheric Sciences 50: 1531-1543